Title

Multi-Faceted Roles of Lithium Metal in Batteries and Beyond

Author

Yuan, Xintong

Publication Date

2025

Peer reviewed|Thesis/dissertation

UNIVERSITY OF CALIFORNIA

Los Angeles

Multi-Faceted Roles of Lithium Metal in Batteries and Beyond

A dissertation submitted in partial satisfaction of the requirements for the degree Doctor of Philosophy in Chemical Engineering

by

Xintong Yuan

2025

ABSTRACT OF THE DISSERTATION

Multi-Faceted Roles of Lithium Metal

in Batteries and Beyond

by

Xintong Yuan

Doctor of Philosophy in Chemical Engineering

University of California, Los Angeles

Professor Yuzhang Li, Chair

Electrochemical energy conversion and storage is critical for advancing vehicle electrification and sustainability of essential commodity chemicals. In pursuit of these goals, I delved progressively deeper into the foundational research of batteries and beyond: (1) pioneering novel methodologies to fundamentally understand lithium (Li) metal deposition, (2) regulating electrolyte decomposition to enhance Li metal batteries (LMBs) performance, and (3) expanding the technology's applicability to make impact beyond batteries.

I have revealed the intrinsic morphology of electrodeposited Li metal to be a non-dendritic rhombic dodecahedron, which defies conventional expectations yet aligns with the theoretical prediction. Li deposition is a process in which Li-ions are reduced to metallic form at the electrode,

which plays a crucial role for LMBs, because the reversibility of deposition morphology directly determines the cycling performance and safety of the battery. However, the simultaneous formation of a surface corrosion film termed the solid electrolyte interphase (SEI) complicates the deposition process, which underpins our poor understanding of Li metal electrodeposition. I creatively integrated the classical electrochemical method, ultramicroelectrode geometry, and an emerging electron microscopy technique, cryogenic electron microscopy (cryo-EM), to decouple Li deposition from the SEI growth and capture the corresponding nanostructure of Li. This discovery has significant implications for LMBs, as it suggests SEI influence can be effectively mitigated to achieve desired deposition morphologies. Besides enhancing our understanding of Li deposition, this work opens new opportunities to explore how reactive metal deposition fundamentally proceeds without the influence of corrosion film, thereby regulating reversibility of metal deposition to optimize the performance of metal batteries.

In addition to deposition morphology, the properties of the SEI also influence the performance of LMBs, as the SEI governs the transportation of Li-ion during cycling. Since the SEI formation results from electrolyte decomposition influenced by electric fields, I systematically examined effects of both electrolyte decomposition and electric fields on SEI formation, progressing from the bulk electrolyte to the electrode surface. I worked with colleagues to quantify reactions driving SEI formation and to determine the decomposition rates of individual electrolyte components, which guided our efforts to design and regulate their decomposition. Furthermore, I emphasized the importance of electric field to further fine-tune the formation of favorable SEI to improve battery performance.

Looking beyond applications of Li metal in batteries, I worked with collaborators to leverage the wealth of battery knowledge and established strategies to investigate fundamental aspects of Li metal as electrocatalyst in electrifying ammonia synthesis to help decarbonize the traditional chemical industry. We revealed key driver behind surface phenomena is the rupture of the SEI, enabling nitrogen and electrolyte to penetrate and react with Li metal to make ammonia. The insights from this work expanded our perspective of how Li metal electrodeposition can decarbonize chemical synthesis and inform our future efforts in designing better LMBs as well.

The dissertation of Xintong Yuan is approved.

Richard B. Kaner

Carlos Gilber Morales-Guio

Philippe Sautet

Yuzhang Li, Committee Chair

University of California, Los Angeles

2025

To my dear family and friends.

Table of Contents

List of Figures

List of Tables

Acknowledgments

First and foremost, I would like to express my deepest gratitude to my advisor, Prof. Yuzhang Li, for his unwavering support, guidance, and mentorship throughout my Ph.D. journey. His insight, patience, and encouragement have shaped not only the direction of my research, but also the way I think as a scientist. I would also like to thank the members of my dissertation committee, Prof. Richard Kaner, Prof. Carlos Morales-Guio, and Prof. Philippe Sautet for their valuable time and support during this process.

My sincere appreciation goes to all the colleagues, collaborators, and labmates I have had the pleasure of working with. In particular, I am deeply grateful to my collaborators, including Prof. Karthish Manthiram, Prof. Philippe Sautet, Dr. Matthew Mecklenburg, Katherine Steinberg, and Dongfang Cheng, for their insights, critical support, and the opportunity to work together on inspiring projects. Additionally, I want to thank Bo Liu for being a wonderful friend, colleague, mentor and mentee throughout this journey. I would also like to thank my colleagues and labmates, including Keyue Liang, Kaiyan Liang, Grace Vasiknanonte, Po-Hung Chen, Haoyang Wu, Jiayi Yu, Elizabeth Zhang, Dingyi Zhao, Dr. Jin Koo Kim, Dr. Hayoung Park, Justin Kim, Huida Lyu, Kaixi Chen, Dr. Tianyu Wang, Dr. Min-Ho Kim, Xinyue Zhang, and Brandan Taing, for their constructive ideas, technical discussions, and for creating such a supportive and motivating environment filled with laughter, kindness, and friendship.

Additionally, I would like to thank all the scientists and staff at the Electron Imaging Center for Nanosystems (EICN) at the California NanoSystems Institute (CNSI), including Dr. Matthew Mecklenburg, Ivo Atanasov, Wong Hoi Hui, Yueyun Chen, Judy Su, Tristan O'Neill and Dr. David

Strugatsky for their training and continued support in electron microscopy-based imaging, which has been invaluable to my research.

I have received tremendous support and encouragement from my friends, including Yanran Wu, Yifeng Shi, Qiuchi Pan, Jinxiu Tian, Wenjin Zhu and many others, and I am truly thankful for their support along the way.

Finally, I would like to thank my family for their unconditional love, understanding, and encouragement over the years. To my parents, thank you for always believing in me and supporting my decisions and dreams.

This work would not have been possible without all of you.

Chapter 2 is reprinted (adapted) from Yuan, X.; Liu, B.; Mecklenburg, M.; Li, Y. Ultrafast deposition of faceted lithium polyhedra by outpacing SEI formation. *Nature* **620**, 86-91 (2023). https://doi.org/10.1038/s41586-023-06235-w. Copyright (2023) Springer Nature. X.Y. and Y.L. conceived the project and designed the experiments. X.Y. built the UME set-up and performed electrochemical experiments and SEM characterization. B.L. helped with COMSOL simulations and data analysis. X.Y. and Y.L. carried out cryo-EM experiments. M.M. advised on microscope and imaging analyses. X.Y. and Y.L. co-wrote the manuscript. All authors discussed the results and commented on the manuscript.

Chapter 3 is reprinted (adapted) from Yuan, X.; Cheng, D.; Liu, B.; Liang, Kaiyan.; Liang, Keyue.; Yu, J.; Mecklenburg, M.; Sautet, P.; Li, Y. Engineering battery corrosion films by tuning electrical

double layer composition. *Joule* **8**, 3038-3053 (2024). https://doi.org/10.1016/j.joule.2024.07.011. Copyright (2024) Elsevier. X.Y. and Y.L. conceived the project and designed the experiments. X.Y. performed electrochemical experiments, XPS, cryo-EM, and in situ Raman characterizations. D.C. and P.S. helped with GCDFT simulations and data analysis. B.L. helped with electrochemical experiments and data analysis. Kaiyan Liang, Keyue Liang, and J.Y. were involved in general discussions. Keyue Liang helped with partial cryo-EM samples preparation. M.M. advised on microscope and imaging analysis. X.Y. and Y.L. co-wrote the manuscript. All authors discussed the results and commented on the manuscript.

Chapter 4 is adapted from Steinberg, K.; Yuan, X.; Klein, C. K.; Lazouski, N.; Mecklenburg, M.; Manthiram K.; Li, Y. Imaging of nitrogen fixation at lithium solid electrolyte interphases via cryo-electron microscopy. *Nature Energy* **8**, 138-148 (2023). https://doi.org/10.1038/s41560-022-01177-5. Copyright (2023) Springer Nature. K.S. and X.Y. contributed equally to this work. K.S., K.M. and Y.L. conceptualized the paper. K.S. developed the experimental methodology for product quantification, sample preparation for imaging and characterization and collection of XPS spectra. X.Y. and Y.L. developed the experimental methodology for SEM and cryo-EM. K.S. performed product quantification, SEM imaging and XPS experiments, and K.S. and C.K. prepared samples for cryo-EM. X.Y. carried out cryo-EM and SEM imaging. Y.L. performed EELS characterization. M.M. advised on microscopy and imaging analysis. C.K. and K.S. performed the validation. K.S. prepared the figures and wrote the original draft of the manuscript and Supplementary Information, and N.L, Y.L., K.M., C.K., X.Y. and K.S. reviewed and edited its contents. K.M. and Y.L. supervised the work.

Vita

2020-2025 Graduate Student Researcher, Chemical Engineering

University of California, Los Angeles

Dissertation Year Fellowship in 2024

MRS Graduate Student Award (Gold) in 2024

Department Award in the 4th Year Symposium in 2024

MIT Chemical Engineering Rising Star in 2024

CMU MIT Stanford UIUC MSE Rising Star in 2024

AIChE Women in Chemical Engineering Travel Award

Nano Letters Seed Grant for the Americas region in 2024

Schmidt Science Fellowship in 2025

2017-2020 Masters of Engineering, Chemical Technology

Tianjin University

National Scholarship in 2019

Graduate with Honor in 2020

Outstanding Thesis Award in 2020

2013-2017 Bachelor of Engineering, Chemical Engineering and Technology

Sichuan University

Graduate with Honor in 2017

Selected Publications

[#]Denotes equal contribution, *Denotes corresponding author.

1. **X. Yuan**, B. Liu, M. Mecklenburg, and Y. Li*, Ultrafast deposition of faceted lithium polyhedra by outpacing SEI formation. *Nature* 2023, **620**, 86-91. (Cover Image)
2. K. Steinberg[#], **X. Yuan**[#], C. K. Klein, N. Lazouski, M. Mecklenburg, K. Manthiram*, and Y. Li*, Imaging of nitrogen fixation at lithium solid electrolyte interphases via cryo-electron microscopy. *Nature Energy* 2023, **8**, 138-148.
3. **X. Yuan**, D. Cheng, B. Liu, K. Liang, K. Liang, J. Yu, M. Mecklenburg, P. Sautet, and Y. Li*, Engineering battery corrosion films by tuning electrical double layer composition. *Joule* 2024, **8**, 3038-3053.
4. **X. Yuan**, S. Chen, D. Cheng, L. Li, W. Zhu, D. Zhong, Z.J. Zhao, J. Li, T. Wang, and J. Gong*, Controllable Cu^0-Cu^+ Sites for Electrocatalytic Reduction of Carbon Dioxide. *Angewandte Chemie International Edition* 2021, **60**, 15344-15347. (Highly Cited Paper)
5. **X. Yuan**[#], L. Zhang[#], L. Li, H. Dong, S. Chen, W. Zhu, C. Hu, W. Deng, Z.J. Zhao, and J. Gong*, Ultrathin Pd-Au shells with Controllable Alloying Degree on Pd Nanocubes toward Carbon Dioxide Reduction. *Journal of the American Chemical Society* 2019, **141**, 4791-4794. (Cover Image)
6. K. Liang[#], **X. Yuan**[#], X. Chen, B. Liu, J.T. Kim, J. Yu, D. Zhao, Y. Li*, A Beginner's Guide to Cryo-EM for Battery Research *Nano Letters* 2025, in press. DOI: 10.1021/acs.nanolett.5c00740

Chapter 1: Introduction and motivation

1.1 The rising need for next-generation batteries

The rapid expansion of electric vehicles (EVs) is reshaping the global energy and transportation landscape. In 2024 alone, global EV sales reached 17 million units, accounting for over 20% of total car sales.[1] This surge reflects not only growing consumer demand but also global policy momentum toward decarbonization and energy transition. As nations strive to meet net-zero emission targets, electrifying transportation has emerged as a central strategy, placing rechargeable batteries, especially high-energy-density systems, at the heart of this transformation.

At present, lithium (Li)-ion batteries (LIBs) serve as the technological backbone of the EV revolution. Their balanced performance in terms of energy density, cycle life, and manufacturability has enabled the proliferation of EVs, portable electronics, and stationary storage systems. Over the past three decades, extensive research has led to the optimization of cathode and anode materials, liquid electrolytes, and cell design, pushing LIB performance to impressive levels.[2-3] However, the fundamental limitations of LIBs are becoming increasingly evident as performance requirements intensify. These include the relatively low theoretical capacity of graphite anodes (~372 mAh g^{-1}),[4-5] and safety concerns related to flammable electrolytes. Consequently, there is a growing need for next-generation battery chemistries that can deliver higher energy densities without compromising safety or cycle life.

Li metal batteries (LMBs) have emerged as one of the most promising candidates to address the energy density limitations. By replacing the graphite anode with metallic Li, LMBs offer a

theoretical specific capacity of 3,860 mAh g^{-1} and the lowest electrochemical potential of any anode material, enabling a step change in cell-level energy density.[5-6] This has far-reaching implications for applications such as long-range EVs, electric aviation, and grid-scale storage. However, despite their theoretical advantages, LMBs face significant challenges that hinder commercial viability. Li metal deposition as one of the most important processes during LMBs cycling is highly uncontrollable and easily leads to poor cycling efficiency, short lifetime, and significant safety risks.[7-9] Various deposition morphologies[10-17] were observed with different electrolytes, yet it remains unclear how distinct electrolyte chemistries lead to certain Li deposition morphologies for decades. The solid electrolyte interphase (SEI) layer, formed simultaneously, regulates Li ions transport from bulk liquid electrolyte to the Li metal surface during deposition and underpins our incomplete understanding of how to precisely control deposited Li metal morphology.

1.2 Toward mechanistic understanding of Li metal in batteries and beyond

To address these challenges, my research seeks to decouple the concurrent processes of Li metal deposition and the SEI formation, thereby exploring them separately. **Chapter 2** decoupled Li metal deposition by outpacing SEI formation at ultrafast deposition rates while also avoiding mass transport limitations using an ultramicroelectrode, a classic method in electrochemistry that allows three-dimensional diffusion pathways at ultrafast current density without sudden ion depletion.[8] By using cryo-EM, the intrinsic Li deposition morphology is quantitatively identified to be a rhombic dodecahedron, which is surprisingly independent of electrolyte chemistry or substrate composition. Furthermore, a pulse-current protocol is proposed to exploit these rhombic

dodecahedra as nucleation seeds, enabling the formation of dense Li deposits and providing new strategies for Li metal anode engineering.

Since Li deposition and SEI formation are decoupled, the SEI formation process can be studied independently. **Chapter 3** explores how SEI formation differs under electrochemical versus purely chemical conditions, focusing on the role of the applied electric field. The definitions of chemical SEI and electrochemical SEI are proposed for the first time due to changes of composition in electrical double-layer (EDL).[18] In conventional electrolytes, the solvent-derived SEI typically exhibits limited anion involvement. However, upon removal of the electric field, enhanced anion participation is observed, which can be attributed to the reduced Coulombic interaction between negatively charged electric field and free anions. By modulating the electric field, an anion-enriched SEI is successfully induced in conventional electrolytes, leading to improved cycling stability and corrosion resistance.

Moreover, the relevance of Li metal deposition and SEI formation is now expanding beyond batteries, gaining attention in applications such as electrified ammonia synthesis. This highlights the broader potential of Li chemistry in addressing pressing energy and environmental challenges. **Chapter 4** introduces a multi-institutional collaboration between MIT, UCLA, and Caltech, which offers a novel perspective on Li metal applications beyond conventional batteries.[19] The experimental design, product quantification, and electrochemical protocols were carried out by collaborators. I led the characterization effort, employing cryo-EM to examine Li metal and SEI interfaces during electrocatalytic nitrogen reduction. This work not only expands the application

scope of Li metal beyond traditional batteries, but also illustrates the broader utility of cryo-EM in understanding dynamic interfacial processes in emerging electrochemical systems.

1.3 References

1. International Energy Agency (IEA). *Global EV Outlook 2024*. https://www.iea.org/reports/global-ev-outlook-2024
2. Xu, K. Electrolytes and interphases in Li-ion batteries and beyond. *Chem. Rev.* **114**, 11503-11618 (2014).
3. Dunn, B., Kamath, H., Tarascon, J.-M. Electrical Energy Storage for the Grid: A Battery of Choices, *Science* **334**, 928-935 (2011).
4. Goodenough, J. B., Park, K. S. The Li-ion rechargeable battery: a perspective, *J. Am. Chem. Soc.* **135**, 1167-1176 (2013).
5. Lin, D., Liu, Y., Cui, Y. Reviving the lithium metal anode for high-energy batteries, *Nature Nanotech.* **12**, 194-206 (2017).
6. Cheng, X. et al. Toward Safe Lithium Metal Anode in Rechargeable Batteries: A Review, *Chem. Rev.* **117**, 10403-10473 (2017).
7. Xu, W. et al. Lithium metal anodes for rechargeable batteries. *Energy Environ. Sci.* **7**, 513–537 (2014).
8. Yuan, X. et al. Ultrafast deposition of faceted lithium polyhedra by outpacing SEI formation. *Nature* **620**, 86–91 (2023)
9. Liu, B. et al. Coupling a sponge metal fibers skeleton with in situ surface engineering to achieve advanced electrodes for flexible lithium-sulfur batteries. *Adv. Mater.* **32**, e2003657 (2020).

10. Bai, P., Li, J., Brushett, F. R. & Bazant, M. Z. Transition of lithium growth mechanisms in liquid electrolytes. *Energy Environ. Sci.* **9**, 3221–3229 (2016).
11. Ren, X. et al. Guided Lithium Metal Deposition and Improved Lithium Coulombic Efficiency through Synergistic Effects of LiAsF6 and Cyclic Carbonate Additives. *ACS Energy Lett.* **3**, 14-19 (2017).
12. Zhang, Y. et al. Dendrite-free lithium deposition with self-aligned nanorod structure. *Nano Lett.* **14**, 6889-6896 (2014).
13. Qian, J. et al. Dendrite-free Li deposition using trace-amounts of water as an electrolyte additive. *Nano Energy* **15**, 135-144 (2015).
14. Weber, R. et al. Long cycle life and dendrite-free lithium morphology in anode-free lithium pouch cells enabled by a dual-salt liquid electrolyte. *Nat. Energy* **4**, 683-689 (2019).
15. Zhang, W. et al. Colossal Granular Lithium Deposits Enabled by the Grain-Coarsening Effect for High-Efficiency Lithium Metal Full Batteries. *Adv. Mater.* **32**, e2001740 (2020).
16. Qian, J. et al. High rate and stable cycling of lithium metal anode. *Nat. Commun.* **6**, 6362 (2015).
17. Zhou, S. et al. Incorporation of LiF into functionalized polymer fiber networks enabling high capacity and high rate cycling of lithium metal composite anodes. *Chem. Eng. J.* **404**, 126508 (2021).
18. Yuan, X. et al. Engineering battery corrosion films by tuning electrical double layer composition. *Joule* **8**, 3038-3053 (2024).
19. Steinberg, K. et al. Imaging of nitrogen fixation at lithium solid electrolyte interphases via cryo-electron microscopy. *Nat. Energy* **8**, 138–148 (2023).

Chapter 2: Ultrafast deposition of faceted lithium polyhedra by outpacing SEI formation

Reprinted (adapted) with permission from Yuan, X.; Liu, B.; Mecklenburg, M.; Li, Y. Ultrafast deposition of faceted lithium polyhedra by outpacing SEI formation. *Nature* **620**, 86-91 (2023). https://doi.org/10.1038/s41586-023-06235-w. Copyright (2023) Springer Nature.

2.1 Abstract

Electrodeposition of lithium (Li) metal is critical for high-energy batteries.[1] However, the simultaneous formation of a surface corrosion film termed the solid electrolyte interphase (SEI)[2] complicates the deposition process, which underpins our poor understanding of Li metal electrodeposition. Here we decouple these two intertwined processes by outpacing SEI formation at ultrafast deposition current densities[3] while also avoiding mass transport limitations. By using cryogenic electron microscopy,[4,5,6,7] we discover the intrinsic deposition morphology of metallic Li to be that of a rhombic dodecahedron, which is surprisingly independent of electrolyte chemistry or current collector substrate. In a coin cell architecture, these rhombic dodecahedra exhibit near point-contact connectivity with the current collector, which can accelerate inactive Li formation.[8] We propose a pulse-current protocol that overcomes this failure mode by leveraging Li rhombic dodecahedra as nucleation seeds, enabling the subsequent growth of dense Li that improves battery performance compared with a baseline. While Li deposition and SEI formation have always been tightly linked in past studies, our experimental approach enables new opportunities to fundamentally understand these processes decoupled from each other and bring about new insights to engineer better batteries.

2.2 Introduction

Uncontrolled lithium (Li) dendritic deposition morphologies pose poor cycling efficiency, short lifetime and significant safety concerns.[9,10,11] The simultaneously formed solid electrolyte interphase (SEI) layer controls lithium ion (Li^+) transport to the depositing surface,[12] which in turn, influences the deposition morphology, generating a complex feedback loop of SEI formation and Li deposition that is difficult to decouple. This concurrent Li deposition and SEI growth underpin our incomplete understanding of how to precisely control Li morphology. For example, four common morphologies of Li metal (for example, filaments,[5,13] nanorods,[14,15,16] columns[17,18] or chunks[19,20]) formed in the model electrolytes shown in Fig. 2.1a all exhibit distinct Coulombic efficiencies (CEs), yet it remains unclear how various electrolyte chemistries lead to certain Li deposition morphologies. While a number of past studies[21] have attempted to rationalize Li deposition morphologies in different electrolytes, a general framework for understanding and predicting Li deposition morphology remains elusive due to the coupled growth of SEI and Li. A paradigm shift in understanding Li electrodeposition requires these two processes to be decoupled. However, SEI formation occurs simultaneously with Li electrodeposition because metallic Li is extremely reactive,[22] immediately reacting with the liquid electrolyte to form the SEI.[23] In principle, Li electrodeposition and SEI formation can be decoupled if Li^+ can be reduced at faster timescales than electrolyte decomposition. Since electrolyte decomposition occurs on the order of seconds, high current densities are needed to outpace SEI influence during Li metal electrodeposition.

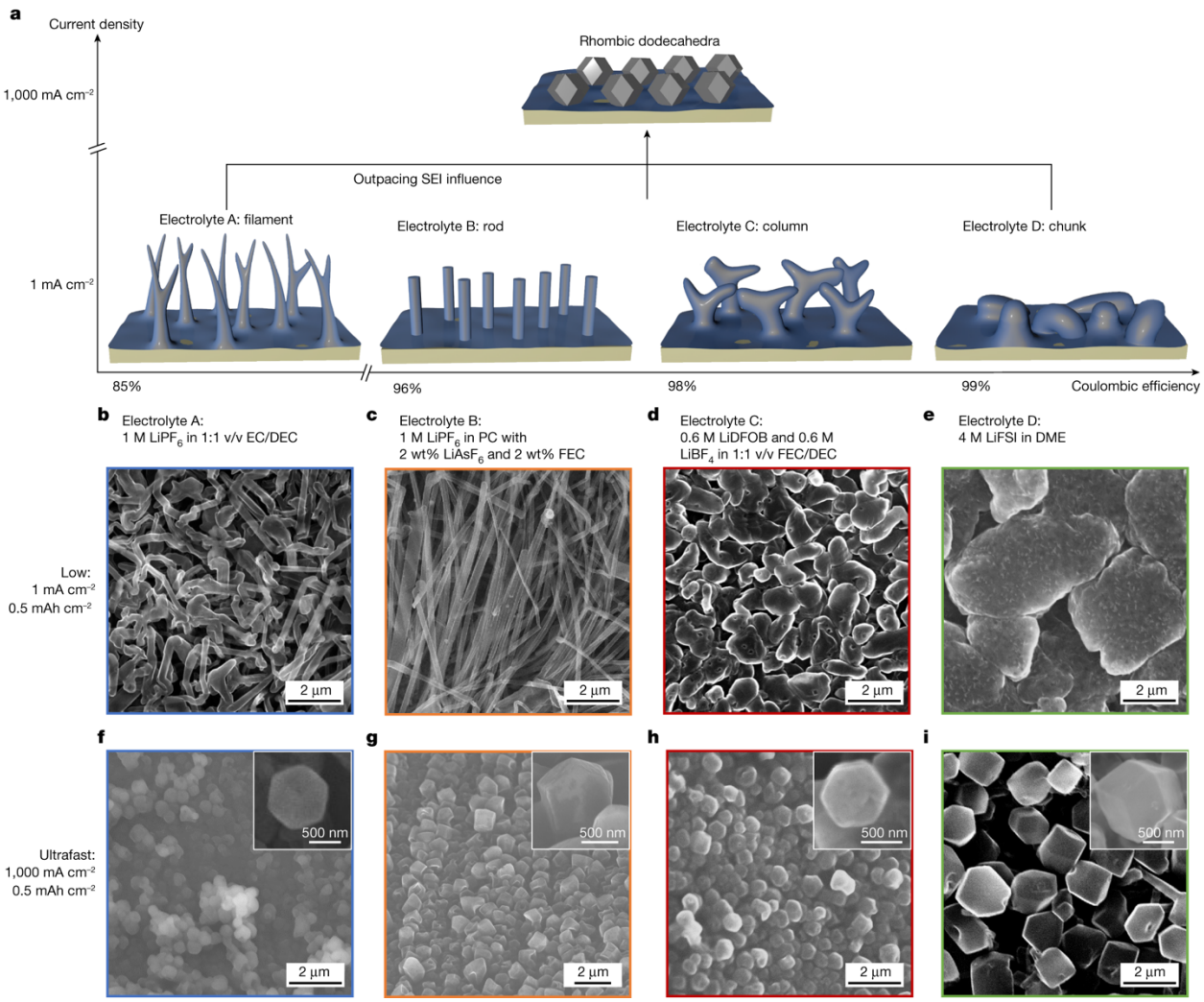

Fig. 2.1 Transition of different dendritic Li to identical faceted Li polyhedra. a, Schematic of the distinct Li electrodeposition morphology as a function of electrolyte chemistry and current density. **b–e**, Li deposition in the Li||Cu coin cell at 1 mA cm^{-2} as filaments in electrolyte A (**b**), rods in electrolyte B (**c**), columns in electrolyte C (**d**) and chunks in electrolyte D (**e**). **f–i**, Faceted Li polyhedra deposited on UME at 1,000 mA cm^{-2} in electrolyte A (**f**), electrolyte B (**g**), electrolyte C (**h**) and electrolyte D (**i**). The insets are magnified images of individual faceted particles.

Here, we decouple Li deposition from SEI growth using an ultramicroelectrode (UME) geometry[3,24,25,26] (Fig. 2.2) and surprisingly, observe that the diverse Li morphologies in the model

electrolytes all transition to a well-defined faceted polyhedron at ultrafast current densities (Fig. 2.1a). This result seems counterintuitive, as previous studies showed that Li dendrites grow increasingly ramified at higher current density,[13,27] yet it aligns with expectations if Li deposition truly proceeds independently from SEI formation. Cryogenic electron microscopy (cryo-EM) quantitatively identifies this morphology to be that of a rhombic dodecahedron, which matches the theoretical Wulff structure prediction of a body-centred cubic (bcc) crystal in the absence of a surface film. Furthermore, we discover that this well-defined faceted morphology persists independent of electrolyte chemistry or current collector substrate, which indicates that outpacing SEI influence can eliminate the effect of these parameters on Li deposition morphology. While these Li rhombic dodecahedra are poorly connected to the current collector and may accelerate inactive Li formation, we overcome this failure mode by proposing a pulse-current strategy that leverages these Li polyhedra as nucleation seeds for enabling improved reversibility of Li plating and stripping.

2.3 Discussion

At high current densities, it is well known[13] that Li metal transitions from base-growing filaments to tip-growing dendritic Li upon diffusion-limited ion depletion at the electrolyte-Li interface. To avoid encountering mass transport limitations at high deposition rates, we used a UME as the depositing substrate. With a limiting current density that scales inversely with the radius, the 25-μm-diameter UME allows three-dimensional diffusion pathways toward the working electrode to sustain ultrafast current densities without sudden ion depletion. COMSOL Multiphysics simulations confirm that at 1,000 mA cm^{-2}, no significant depletion of Li^+ occurred on the working electrode surface (Fig. 2.3).[28,29] To deposit metallic Li at both normal and ultrafast rates, we chose

four model electrolytes for their diversity in chemistry (for example, carbonate versus ether solvent, low versus high salt concentration, single versus dual salts and with versus without additives), which results in widely varying SEI layers, Li deposition morphologies and CE:[4,17,19,30] electrolyte A, 1 M lithium hexafluorophosphate ($LiPF_6$) in 1:1 v/v ethylene carbonate (EC)/diethyl carbonate (DEC); electrolyte B, 1 M $LiPF_6$ in propylene carbonate (PC) with 2 wt% lithium hexafluoroarsenate ($LiAsF_6$) and 2 wt% fluoroethylene carbonate (FEC); electrolyte C, 0.6 M lithium difluoro(oxalato)borate (LiDFOB) and 0.6 M lithium tetrafluoroborate ($LiBF_4$) in 1:1 v/v FEC/DEC; electrolyte D, 4 M lithium bis(fluorosulfonyl)imide (LiFSI) in dimethoxyethane (DME). While these electrolytes form distinct SEI layers that govern battery performance[31,32] under normal operating conditions (1–10 mA cm^{-2}), we expect the SEI and electrolyte chemistry to have diminished influence at ultrafast deposition regimes (50–1,000 mA cm^{-2}) that are predicted to outpace SEI growth.

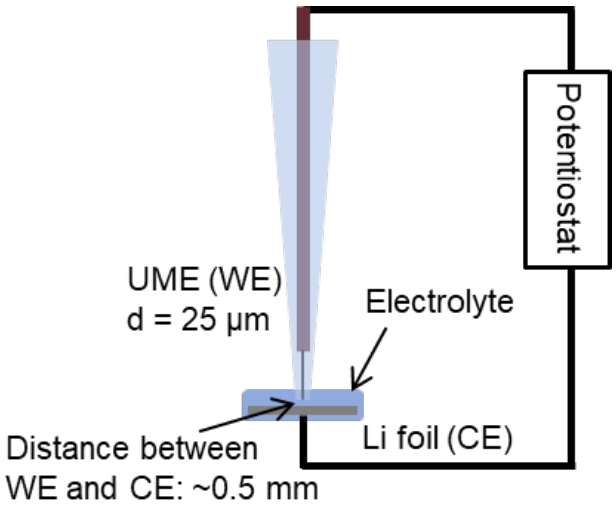

Fig. 2.2 Schematic of UME platform. UME is the working electrode (WE) and Li foil is the counter electrode (CE, only for this Figure). The distance between WE and CE is minimized to ~0.5 mm in our UME experiments.

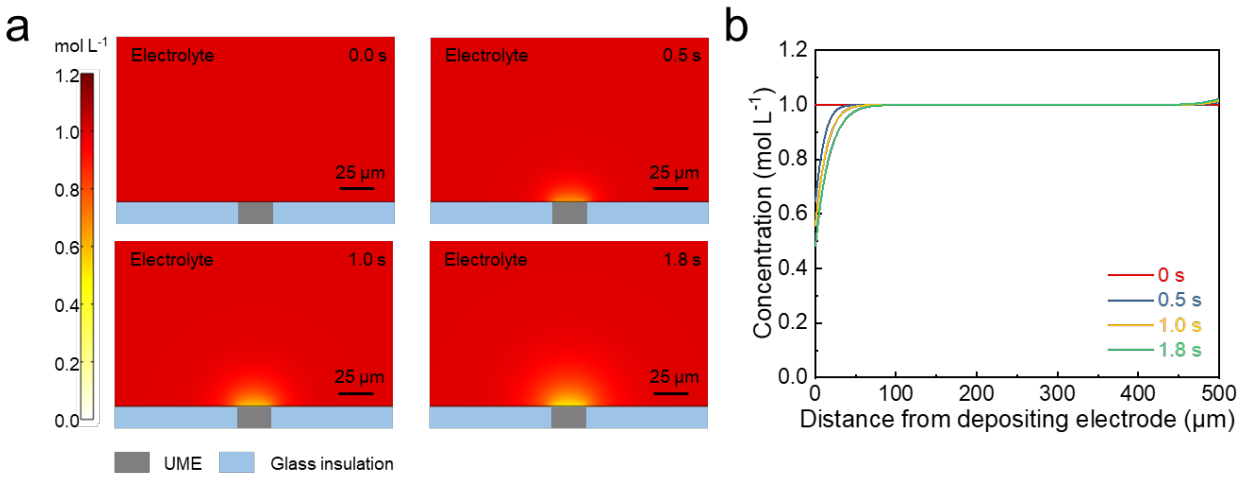

Fig. 2.3 COMSOL Multiphysics simulation of Li^+ concentration on UME geometry at 1,000 mA cm^{-2}. a, A two-dimension cross-sectional Li^+ concentration gradient visualized under current density of 1,000 mA cm^{-2} at different deposition times in UME geometry, the thickness of electrodes is neglected. b, Li^+ concentration gradient plots as a function of distance from the working electrode at different times.

Upon Li deposition at typical current densities, we found distinct Li morphologies in each of the model electrolytes (for example, 'filaments' in electrolyte A, 'rods' in electrolyte B, 'columns' in electrolyte C and 'chunks' in electrolyte D), as shown in Fig. 2.1b–e. While these qualitative descriptions highlight our incomplete understanding of Li deposition morphology, they are commonly used to explain key differences in macroscale battery performance between these electrolytes. For example, electrolytes C and D exhibit much higher CE (approximately 97–99%) than electrolyte A (approximately 85%) due to the lower surface area to volume ratio of the Li deposits. Interestingly, at an ultrafast current density of 1,000 mA cm^{-2}, we discover a stark morphological transition to well-defined faceted Li polyhedra in all electrolytes (Fig. 2.1f–i and

Fig. 2.4). The trend in polyhedra size in the four electrolytes (spanning from 0.4 to 1.2 µm) corresponds well with the differing electrodeposition overpotential (Fig. 2.5), which is consistent with classical nucleation theory.[33] Additionally, we note that there exists a minimum current density sufficient to outpace SEI influence that will change depending on cell geometry, temperature, pressure, electrolyte chemistry and other factors. It is not the scope of this initial work to quantify or understand how the minimum current density changes with such parameters (Fig. 2.6) but rather, to demonstrate the implications for surpassing this threshold.

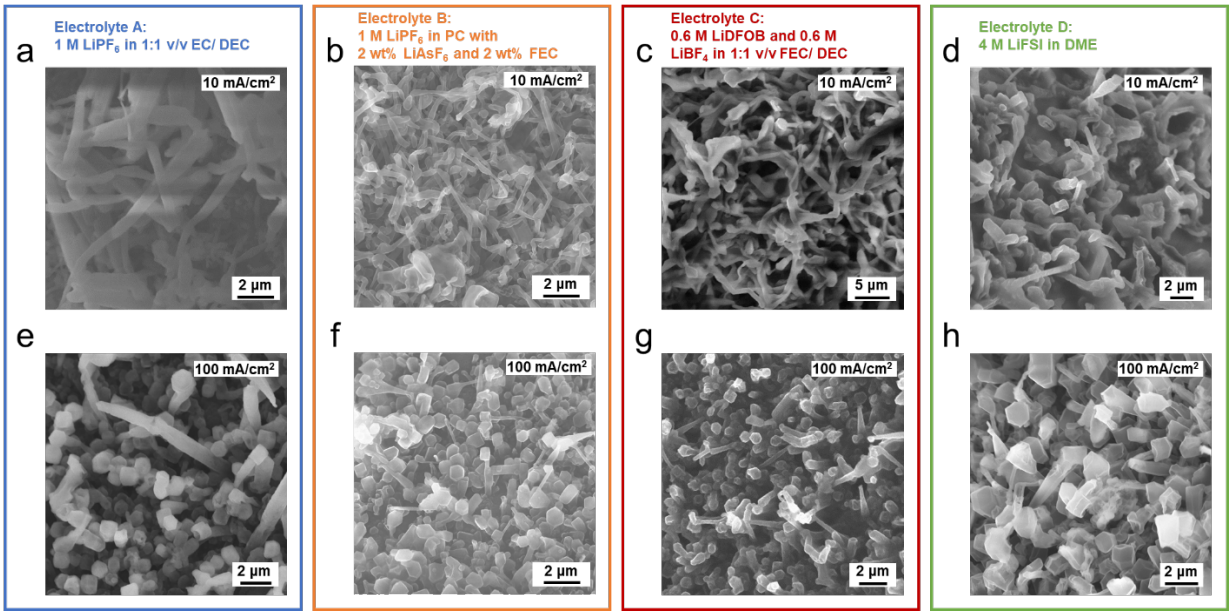

Fig. 2.4 Transition of different dendritic Li to identical faceted Li particles on UME from 10 to 100 mA cm^{-2} with a capacity of 0.5 mAh cm^{-2}. a, b, c, d, Dendritic Li deposited on UME at 10 mA cm^{-2}. **e, f, g, h,** Mixed dendritic and faceted Li particles deposited on UME at 100 mA cm^{-2}. The electrolyte from left to right are electrolyte A, electrolyte B, electrolyte C and electrolyte D.

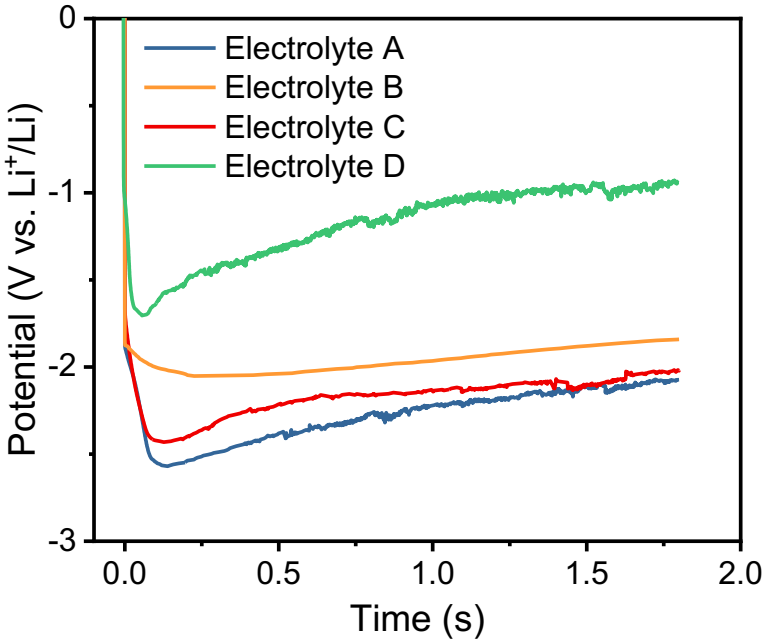

Fig. 2.5 Potential profiles of Li deposition on UME at a current density of 1,000 mA cm^{-2} for a total capacity of 0.5 mAh cm^{-2} in four electrolytes.

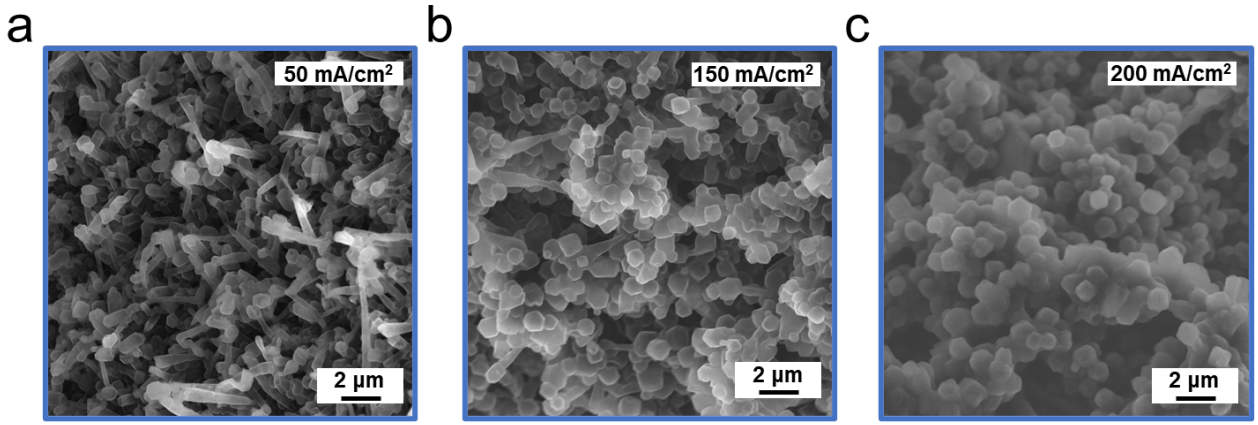

Fig. 2.6 SEM images show the morphology of electrodeposited Li metal on the UME in electrolyte A at different current densities with a capacity of 0.5 mAh cm^{-2}. Mixed dendritic and faceted Li particles deposited at (**a**) 50 mA cm^{-2} and (**b**) 150 mA cm^{-2}. **c**, Faceted Li polyhedra observed at 200 mA cm^{-2}. As the current density increases from 50 to 150 mA cm^{-2}, the ratio of

dendritic Li particles to faceted Li particles decreases. At a current density of 200 mA cm^{-2}, we observe no more dendritic Li particle morphologies. Further increasing the current density to 1000 mA cm^{-2} will not change the polyhedron morphology since the critical current density is surpassed (Fig. 2.1f).

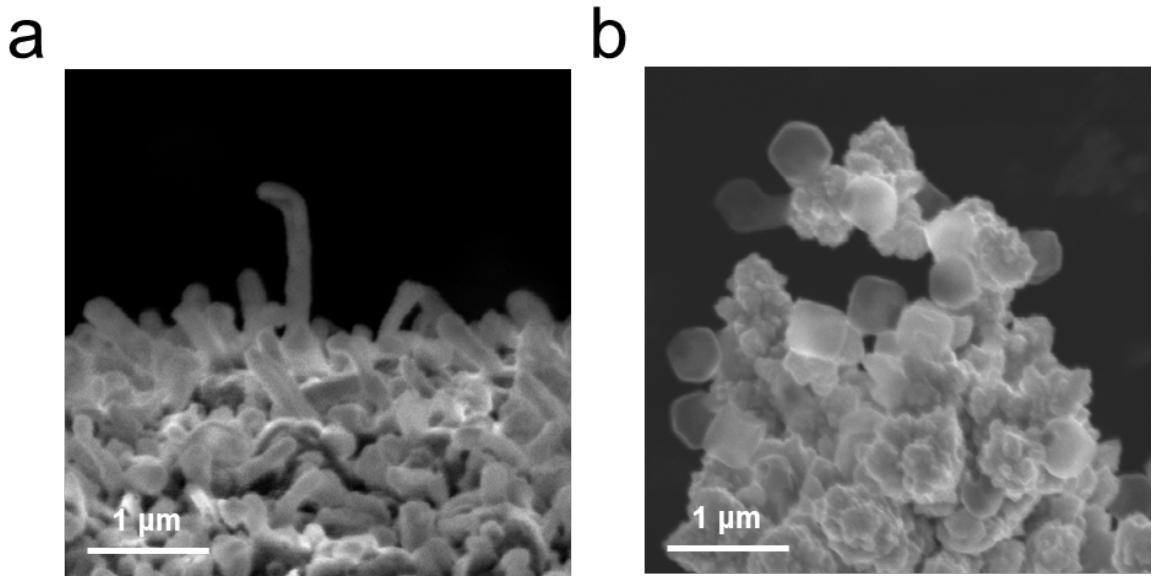

Fig. 2.7 SEM of dendritic and faceted Li particles deposited on TEM grids in electrolyte C. **a**, Dendritic Li deposition on bare Cu TEM grid at 10 mA cm^{-2}. **b**, Faceted Li polyhedra deposition on Cu chunks-coated TEM grid at 200 mA cm^{-2}. To facilitate the imaging of individual particles on the nanometer scale, the coverage of Li on the TEM grid is low with a capacity of 0.1 mAh cm^{-2}.

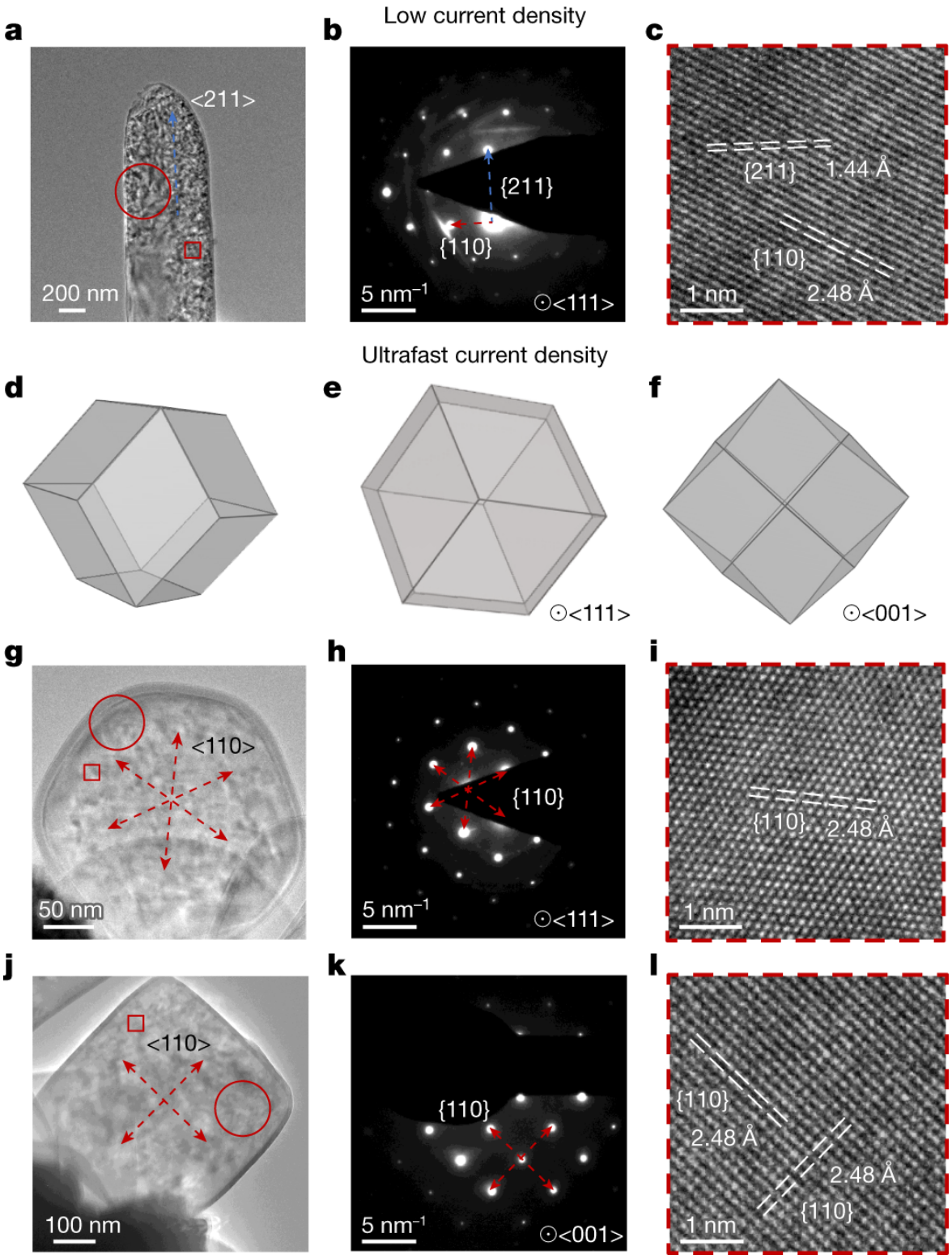

Fig. 2.8 Atomic-resolution cryo-EM of Li rhombic dodecahedra with faceting behaviours. a, Cryo-EM image of Li column morphology grown on the Cu TEM grid at low current density. **b**,

SAED pattern of the Li column region shown in the red circle of **a**. **c**, High-resolution image of the red boxed region from **a**. **d**, Schematic of bcc Wulff construction. **e**,**f**, bcc Wulff construction shapes aligned along the <111> (**e**) and <001> (**f**) zone axes. **g**, Cryo-EM image of the faceted rhombic dodecahedron Li particle aligned along the <111> zone axis (two-dimensional projection of **e**). **h**, Li metal SAED pattern of the red circled region of **g**. **i**, High-resolution cryo-EM image of the red boxed region from **g**. **j**, Cryo-EM image of the faceted rhombic dodecahedron Li particle aligned along the <001> zone axis (two-dimensional projection of **f**). **k**, Li metal SAED pattern of the red circled region of **j**. **l**, High-resolution cryo-EM image of the red boxed region from **j**. All images correspond to electrolyte C: 0.6 M LiDFOB and 0.6 M $LiBF_4$ in 1:1 v/v FEC/DEC.

Indeed, these faceted Li polyhedra appear identical across distinct electrolyte chemistries (Fig. 2.1f–i), which suggests three important findings. (1) The morphology dependence on electrolyte chemistry disappears at ultrafast current densities, (2) Li deposition and SEI formation can be decoupled at ultrafast current densities and (3) the faceted polyhedra are the intrinsic deposition morphology of Li metal in the absence of SEI influence.[34] The well-defined faceted particle shape implies that they are rhombic dodecahedra, which match the thermodynamic Wulff construction of a bcc crystal with only {110} planes exposed as surfaces. For a bcc crystal, the {110} faces are the most densely packed planes, and thus, exposing their lowest-energy surface would minimize the energy of the system. We must note, however, that these scanning electron microscopy (SEM) observations are merely qualitative based on the morphology and crystallographic understanding of Li metal itself. For more quantitative crystallographic evidence of the intrinsic Li deposition morphology being rhombic dodecahedra, we leverage the powerful cryo-EM to preserve the pristine surfaces of the faceted Li polyhedra.

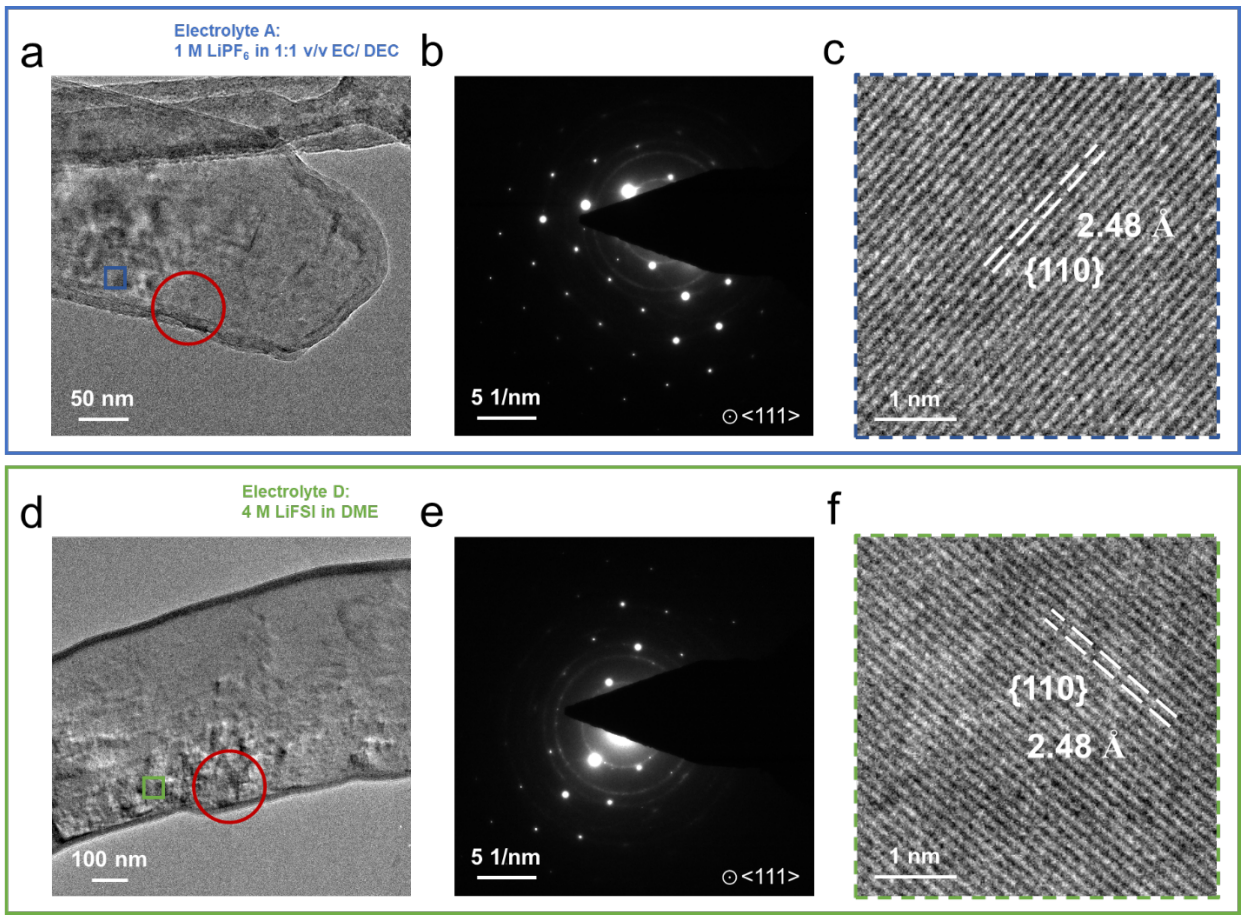

Fig. 2.9 Cryo-EM showing dendritic Li grown in different electrolyte chemistry at 10 mA cm^{-2} with a capacity of 0.1 mAh cm^{-2}. a, d, Cryo-EM image of a dendritic Li grown on a Cu TEM grid at normal current density. **b, e,** SAED patterns of dendritic Li shown in (**a, d**). **c, f,** Magnified images of boxed regions from (**a, d**). The electrolytes are electrolyte A in the first row and electrolyte D in the second row.

Within the electron microscope, selected area electron diffraction (SAED) can identify the crystalline planes exposed on the Li facets, and high-resolution imaging can reveal the atomic structure of the individual faceted Li particle. First, we deposit Li metal directly onto copper (Cu)

transmission electron microscopy (TEM) grids at low current density as a control sample (Fig. 2.7a). Combining cryo-EM imaging and the corresponding SAED pattern (Fig. 2.8a–c), Li in electrolyte C grows as a single crystalline nanowire along the <211> direction (blue arrow), which is one of the common growth directions of Li dendrites.[4] The lattice spacing of 1.44 Å was obtained in the high-resolution image (Fig. 2.8c) and matched with the Li {211} plane.[4] Similar results in electrolytes A and D can be found in Fig. 2.9. To grow faceted Li polyhedra at ultrafast current densities on TEM grids (Fig. 2.7b), we modify stainless steel TEM grids with electrodeposited Cu nanowires to serve as local UMEs, producing high electric fields[35] that locally concentrate electrolyte cations during ultrafast deposition. The bcc Li metal crystal has a space group of $Im3m$ and a corresponding rhombic dodecahedral geometry as predicted by the Wulff construction (Fig. 2.8d).[34] When viewing the two-dimensional projection of a rhombic dodecahedron using cryo-EM, we expect a hexagonal shape (Fig. 2.8e) when Li is aligned along the <111> zone axis and a square shape (Fig. 2.8f) when aligned along the <001> zone axis. Indeed, we do observe such shapes: a hexagon in Fig. 2.8g, where its corresponding SAED pattern (Fig. 2.8h) confirms its alignment along the <111> zone axis, and a square in Fig. 2.8j, where its corresponding SAED pattern (Fig. 2.8k) confirms its alignment along the <001> zone axis. The red arrows in the hexagonal SAED pattern (Fig. 2.8h) represent the {110} direction pointing toward the reciprocal space reflections (Fig. 2.8g, circled in red), which correspond to the {110} family of planes. These same arrows overlaid on the hexagonal Li metal polyhedra point toward the edge facets, which directly confirms that these surfaces are {110} planes (Fig. 2.8g). This same analysis allows us to assign the crystal facets for the surfaces exposed in the square Li projection along the <001> zone axis, all of which are also the {110} planes (Fig. 2.8j). These cryo-EM data showing the only exposed surfaces being

the {110} planes confirm the native Li deposition morphology without SEI influence to be that of a rhombic dodecahedron.

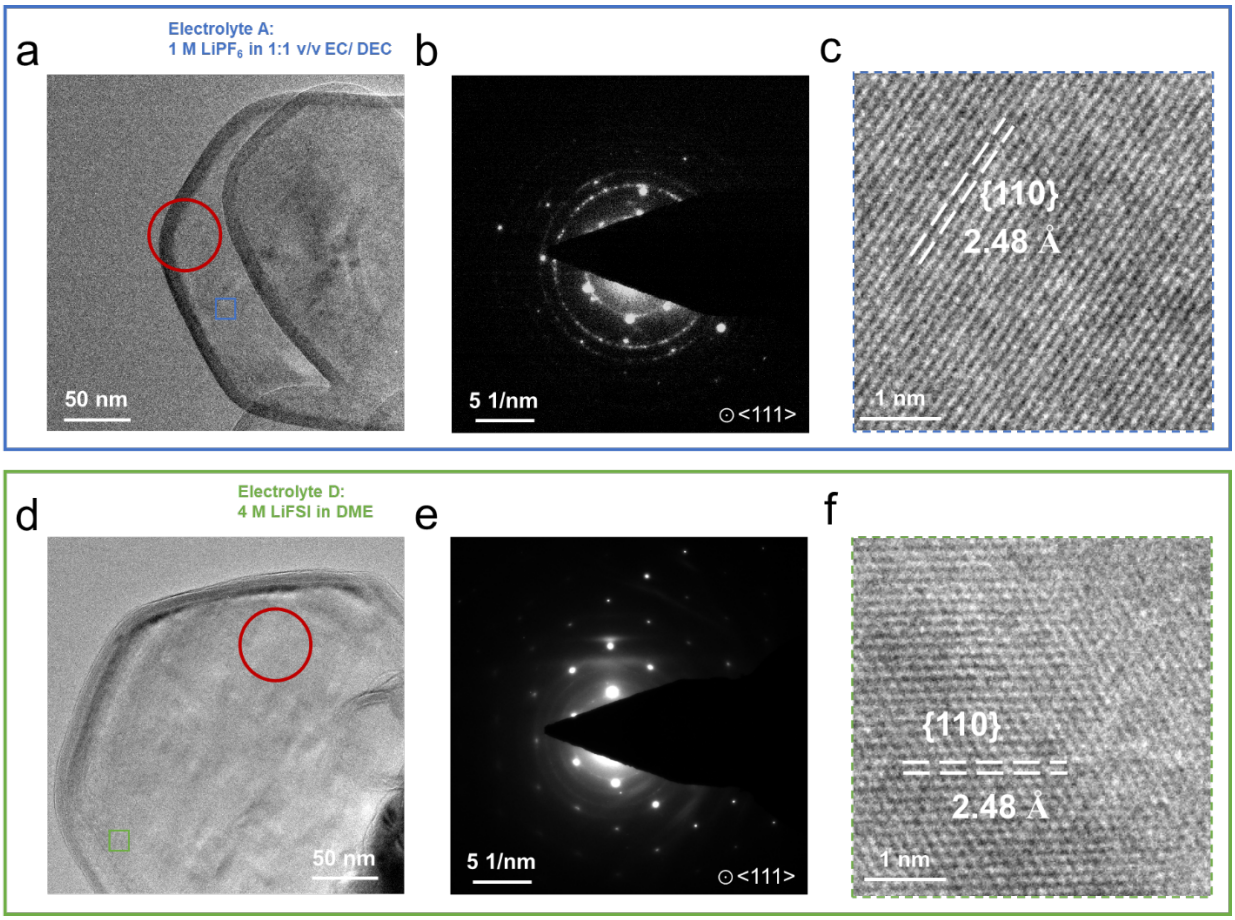

Fig. 2.10 Cryo-EM showing faceted Li polyhedra grown in different electrolyte chemistry at 200 mA cm^{-2} with a capacity of 0.1 mAh cm^{-2}. a, d, Cryo-EM image of a faceted Li polyhedral grown on the Cu chunks-coated TEM grid at ultrahigh current density. **b, e,** SAED patterns of the faceted particles shown in (**a, d**). **c, f,** Magnified images of boxed regions from (**a, d**). The electrolytes are electrolyte A in the first row and electrolyte D in the second row.

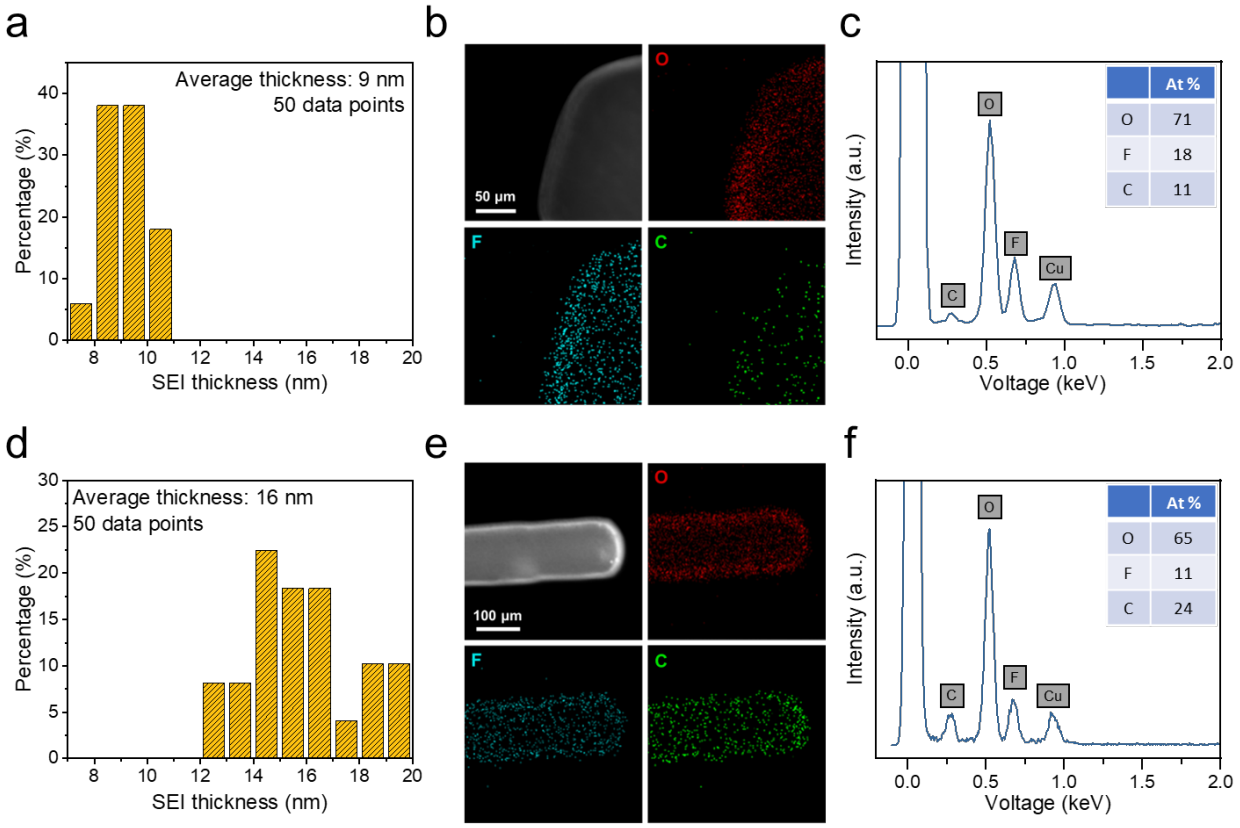

Fig. 2.11 Comparison in structure and chemistry of the SEI formed on faceted Li polyhedra and Li dendrites. a, Thickness statistics of the SEI formed on faceted Li polyhedral. Scanning transmission electron microscopy energy dispersive spectroscopy (**b**) mapping and (**c**) spectrum of faceted Li polyhedra and its SEI, insert is the atomic ratio of each element. **d, e, f,** Analogous images to (**a, b, c**) but collected on the SEI formed on dendritic Li. SEI thickness statistics demonstrates that SEI grown on faceted polyhedral has a significantly decreased thickness compared to the SEI on dendrites (9 nm vs. 16 nm). Relative ratio of elements shows that SEI grown on faceted polyhedral has much more inorganic components (fluorine and oxygen) than the SEI formed on Li dendrites. This difference further illustrates that the SEI formed on the faceted polyhedral is different from the SEI formed on Li dendrites.

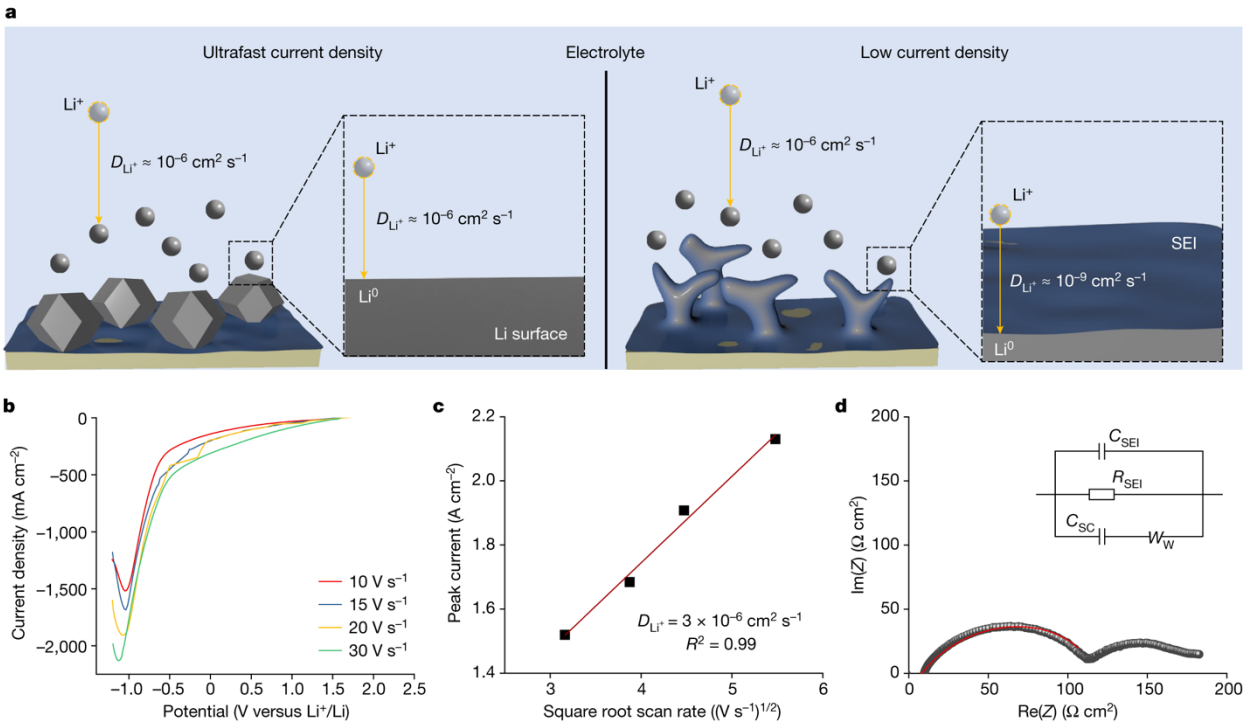

Fig. 2.12 Electrochemical analysis of Li plating pathways at ultrafast and low current density regimes. a, Schematic of Li^+ transport from electrolyte to electrode surface without the SEI at ultrafast current density (left) and with the SEI at normal current density (right). **b**, LSV profiles of Li electrodeposition with an ultrafast scan rate from 10 to 30 V s^{-1}. c, The dependence of the peak current on the square root of the scan rate. **d**, Nyquist plot of the EIS and the fitting result for the symmetric Li||Li coin cell; the inset is the SEI equivalent circuit model.

High-resolution cryo-EM images of the faceted Li polyhedra (Fig. 2.8i,l) resolve individual Li atoms, showing that these deposits are single crystalline and expose the {110} facets. At the atomic scale, the lattice spacings are measured to be 2.48 Å (Fig. 2.8i,l), which matches well with the known spacing of the Li {110} plane.[4] We note that the surface of Li polyhedra appears to be covered by an apparent SEI layer, which we propose is the result of inevitable contact between the freshly deposited Li and liquid electrolyte[23,36] after ultrafast deposition during cryo-EM sample

preparation that takes on the order of minutes (more than enough time for fresh metallic Li to react chemically with the electrolyte). This is supported by cryo-EM experiments that confirm that Li metal is also deposited as rhombic dodecahedra in electrolytes A and D, demonstrating that the SEI and electrolyte chemistry do not influence the deposition morphology at ultrafast current densities (Fig. 2.10). It is then likely that Li electrodeposition and SEI formation proceed in a stepwise manner when they are decoupled, with Li deposition occurring first electrochemically and SEI formation proceeding chemically after Li deposition. This is supported by cryo-EM and energy-dispersive spectroscopy that confirm structural and chemical differences between SEI formed on faceted Li polyhedra and SEI formed on Li dendrites (Fig. 2.11).

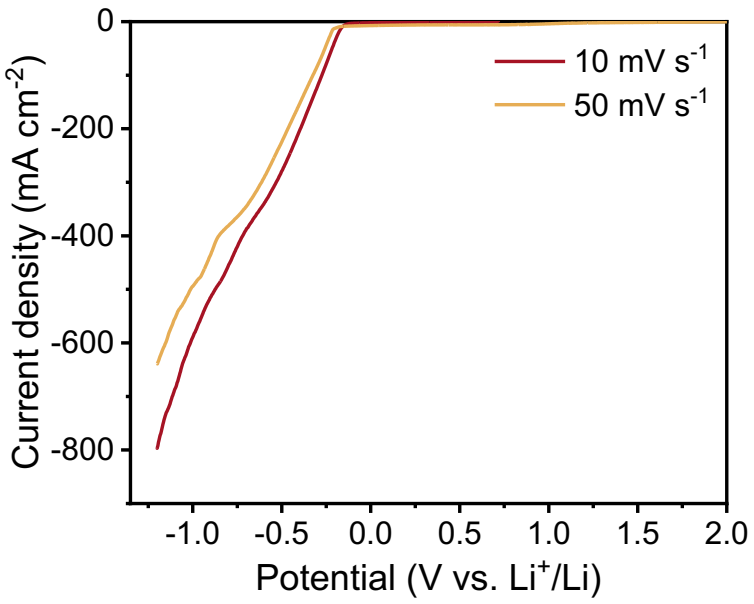

Fig. 2.13 Comparison LSV profiles with normal scan rates.

To verify that Li electrodeposition at ultrafast current densities proceeds without SEI influence, we measure Li^+ transport from the bulk to the depositing metallic Li surface in both normal and

ultrafast current density regimes. Li^+ diffusion coefficients (D_{Li^+}) in the solid (SEI) and liquid (electrolyte) phase are significantly different and often vary by orders of magnitude (Fig. 2.12a). To measure Li^+ transport at ultrafast current density regimes, linear sweep voltammetry (LSV) experiments with ultrafast scan rates from 10 to 30 V s^{-1} are carried out (Fig. 2.12b; LSV data with low scan rates are in Fig. 2.13). Fig. 2.12c shows that the peak current density scales linearly with the square root of scan rate, which can be used to calculate a D_{Li^+} value of 3×10^{-6} cm^{-2} s^{-1} (calculation details are in the Methods).[3] The magnitude of 10^{-6} cm^{-2} s^{-1} is the same as previous measurements[3,37] of D_{Li^+} in liquid electrolytes (Fig. 2.12a), which indicates that Li^+ transport to the Li-electrolyte interface occurs at the same speed as if in the bulk liquid without SEI interference. To measure Li^+ transport to the Li surface at normal current density regimes, we construct an Li||Li symmetric coin cell to characterize the ionic resistance. This enables calculation of D_{Li^+} from the bulk to the Li surface under normal current density regimes to be 4.4×10^{-9} cm^{-2} s^{-1}. Since Li^+ transport through the SEI accounts for the majority (more than 98%) of the interfacial impedance in an Li||Li cell (Fig. 2.12d and Fig. 2.14), the dramatic decrease in D_{Li^+} shows that the SEI impedes Li^+ transport under normal current densities.[3] These quantitative measurements show the clear difference in how Li^+ travels from the bulk liquid to the Li surface in the two current density regimes. At ultrafast current densities, Li^+ transport to the surface is on the same order of magnitude as bulk liquid diffusion; at normal current densities, Li^+ transport is slowed by three orders of magnitude and must travel through an SEI layer that is dependent on electrolyte chemistry and controls the Li^+ transport.

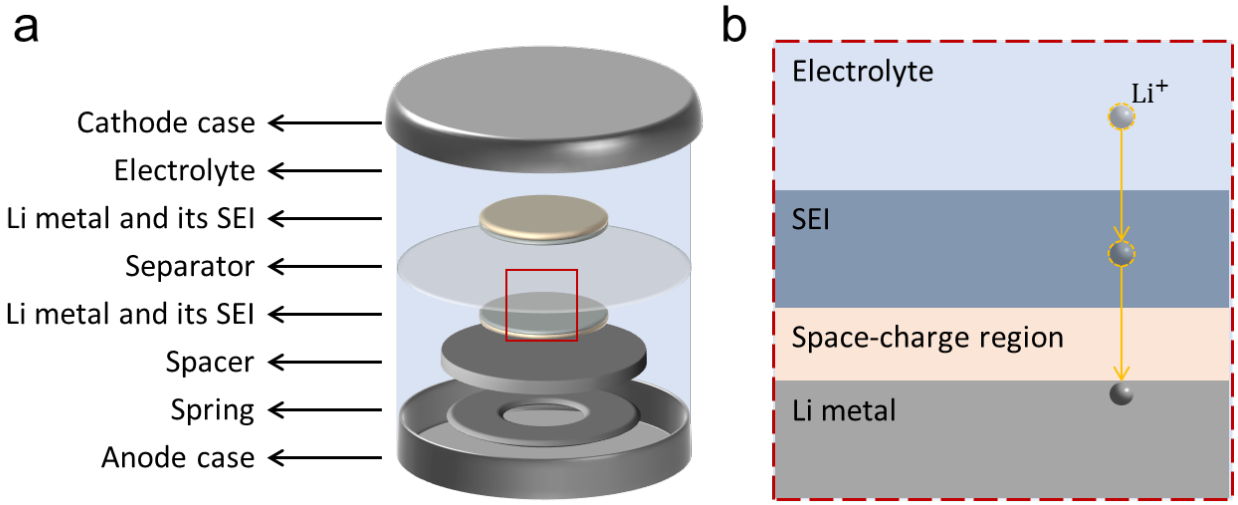

Fig. 2.14 Schematics of a Li||Li symmetric coin cell and corresponding internal model. a, Schematics of a Li||Li symmetric cell. **b**, Magnified region from red box in (**a**), corresponding to equivalent circuit model used in Fig. 2.12d.

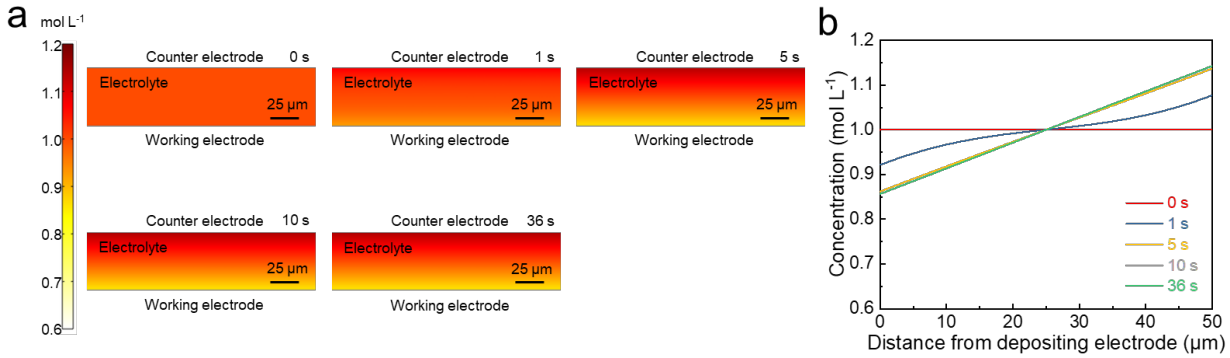

Fig. 2.15 COMSOL Multiphysics simulation of Li^+ concentration on coin cell geometry at 50 mA cm^{-2}. a, A two-dimension cross-sectional Li^+ concentration gradient visualized under current density of 50 mA cm^{-2} at different deposition times, the thickness of electrodes is neglected. **b**, Li^+ concentration gradient plots as a function of distance from the working electrode at different times.

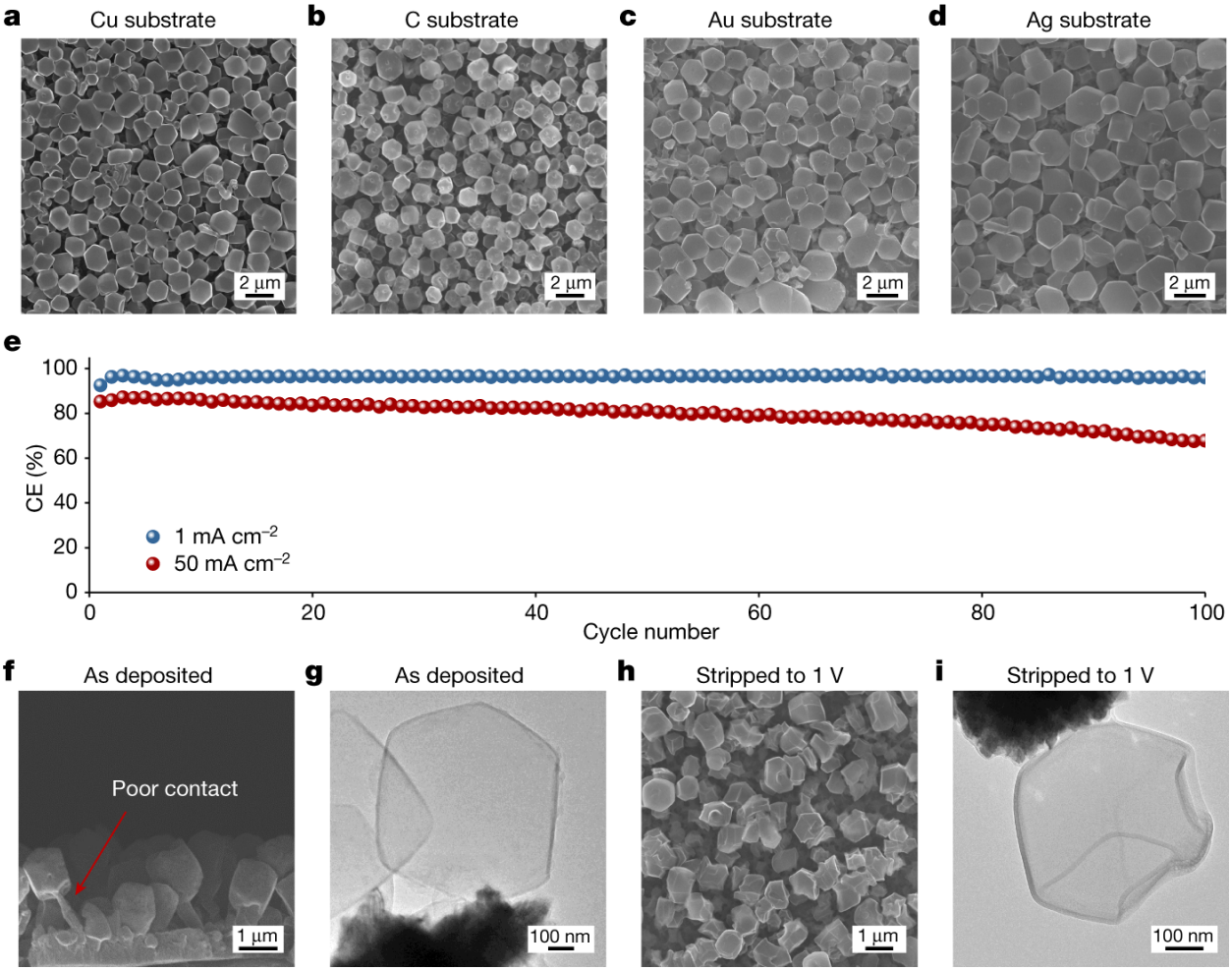

Fig. 2.16 Li plating as rhombic dodecahedra in coin cell geometry and its failure mechanism analysis. a–d, SEM images of Li polyhedra grown on Cu (**a**), C (**b**), Au (**c**) and Ag (**d**) substrates at 50 mA cm^{-2}. **e**, CE of Li||Cu cells at current densities of 1 mA cm^{-2} and 50 mA cm^{-2}. **f**,**g**, Cross-sectional SEM view (**f**) and cryo-EM image (**g**) showing poor contact between deposited faceted Li particles and Cu substrate. **h**, Cu foil with abundant inactive Li after stripping with 1 V cutoff voltage. **i**, Cryo-EM image of the partially stripped Li particle after stripping with 1 V cutoff voltage. The electrolyte is C: 0.6 M LiDFOB and 0.6 M $LiBF_4$ in 1:1 v/v FEC/DEC.

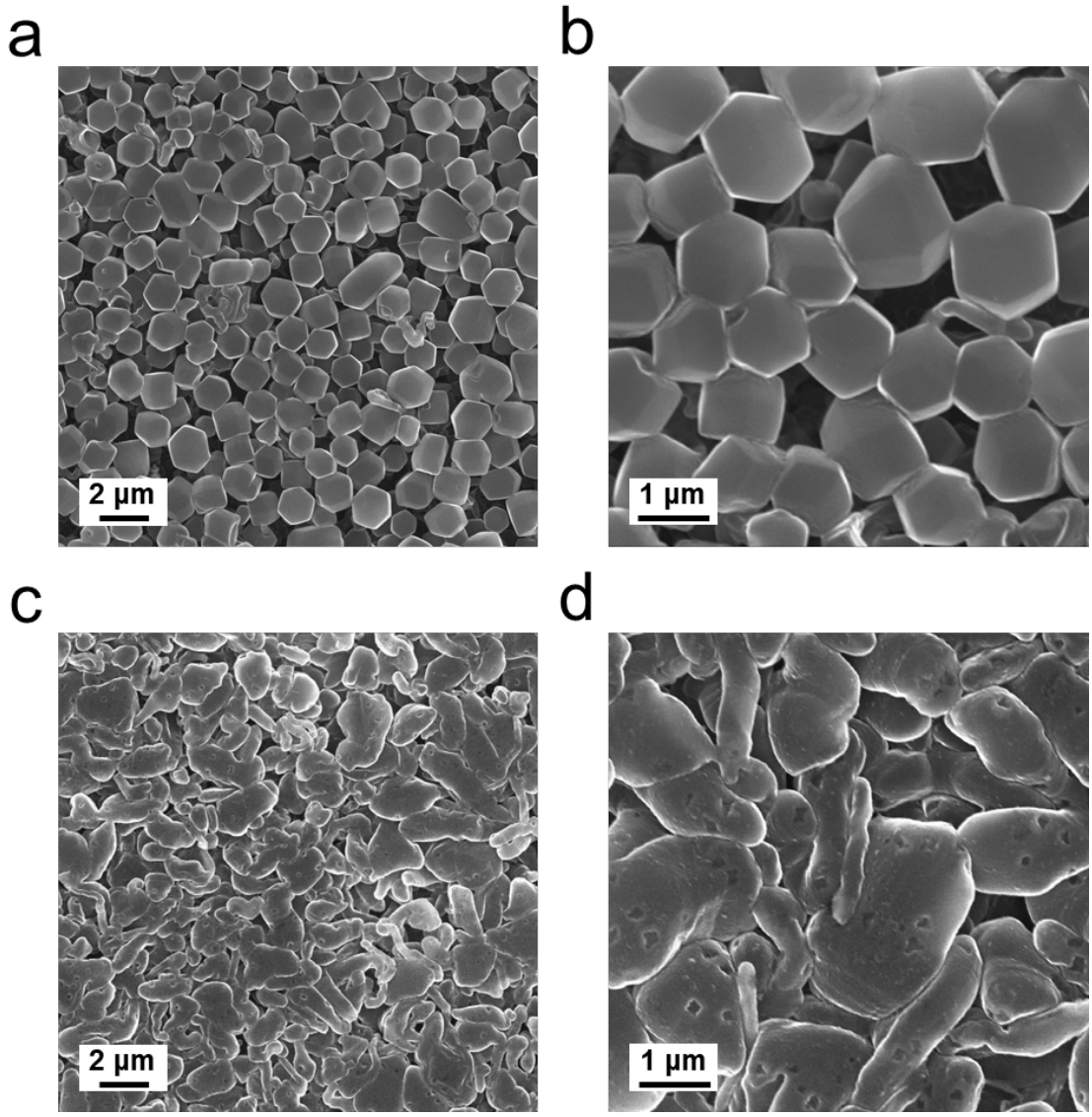

Fig. 2.17 SEM of faceted and column-like Li deposition on Cu current collector in coin cell in electrolyte C. Li polyhedra deposition in Li||Cu coin cell at (**a, b**) 50 mA cm^{-2} with 0.5 mAh cm^{-2}. SEM of column-like Li deposition in Li||Cu coin cell at (**c, d**) 1 mA cm^{-2} with 0.5 mAh cm^{-2}.

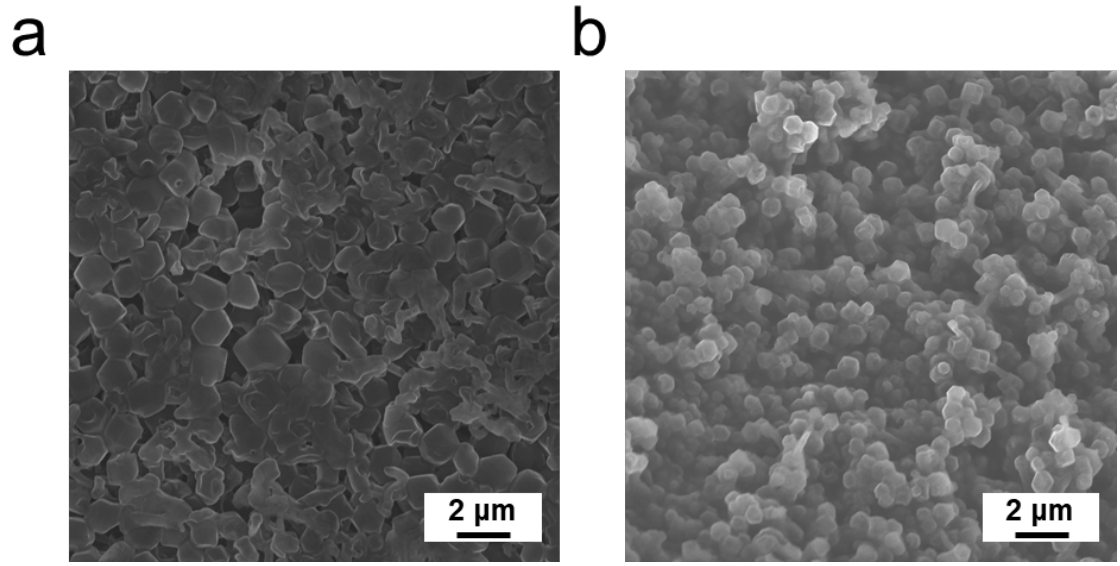

Fig. 2.18 SEM images of faceted Li polyhedral deposited in different geometries with a capacity of 3 mAh cm^{-2}. a, Faceted Li polyhedral (with some particles merging together) deposited on Cu current collector in coin cell at 50 mA cm^{-2}. **b**, Faceted Li polyhedral deposited on UME at 1,000 mA cm^{-2}. A practical deposition capacity of 3 mAh cm^{-2} is demonstrated here. In the UME geometry, morphology of faceted polyhedra can be retained with a capacity of 3 mAh cm^{-2}. While faceted particles can also be observed in the coin cell geometry at this larger capacity, we find that most of the deposited Li facets have merged due to the uniaxial pressure present inside the coin cell.

While our UME studies are crucial for revealing the intrinsic deposition morphology of Li metal without SEI influence, we further show its implications for operation in coin cell batteries. To confirm that there are no mass transfer limitations at a current density of 50 mA cm^{-2}, we performed COMSOL Multiphysics simulations, showing that the Li^+ concentration gradient can be controlled within 0.3 M from counter to working electrode, and we reach a linear steady state in under 10 s in a coin cell geometry (Fig. 2.15). We successfully deposited Li rhombic

dodecahedra at 50 mA cm^{-2} with a capacity of 0.5 mAh cm^{-2} (Fig. 2.16a and Fig. 2.17a,b; images with 3 mAh cm^{-2} are in Fig. 2.18). In contrast, a column-like Li morphology (Fig. 2.1b and Fig. 2.17c,d) is observed at 1 mA cm^{-2} with the same capacity and electrolyte chemistry. This finding at ultrahigh current densities subverts conventional wisdom that argues that high current densities are likely to promote more dendritic growth of Li. Instead, we demonstrate that ultrahigh current densities can lead to the non-dendritic growth of Li rhombic dodecahedra as long as mass transport limitations are avoided and the deposition rate can outpace SEI formation. Furthermore, we find that the rhombic dodecahedra structure is independent of the current collector substrate at 50 mA cm^{-2}, regardless of whether the substrate is lithiophobic (for example, Cu, C and so on) or lithiophilic (for example, Au, Ag and so on) (Fig. 2.16a–d and Fig. 2.19). This finding sharply contrasts with our conventional understanding that the substrate exerts a significant influence on metallic deposition morphology at normal current densities.[38] Since alloy formation kinetics between Au and Li are orders of magnitude slower than the kinetics of SEI formation,[39] it stands to reason that if SEI influence is outpaced at ultrafast current densities, the substrate influence is outpaced as well. Although the morphology dependence on substrates disappears at ultrafast current density, the size dependence of Li polyhedra on overpotential remains consistent with nucleation theory[33] (Fig. 2.20). Our results show that it is possible to outpace SEI formation even in a coin cell geometry, allowing us to explore the practical Li plating and stripping behaviours of the unique Li rhombic dodecahedra.

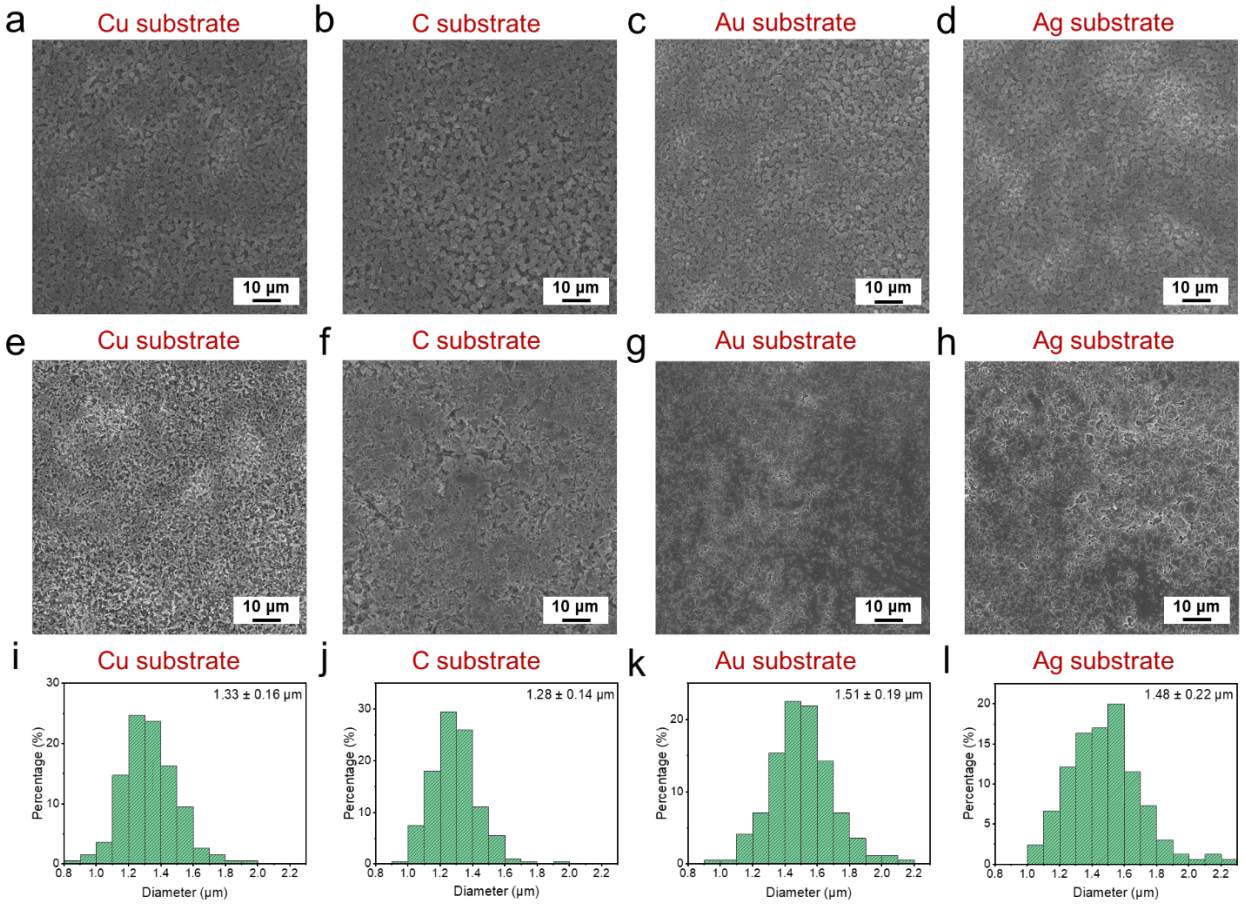

Fig. 2.19 Low magnification SEM images of Li plating morphology at different current densities in coin cell geometry on different substrates showing morphology uniformity. Li polyhedra grown on (**a**) Cu, (**b**) C, (**c**) Au and (**d**) Ag substrates at 50 mA cm^{-2} with a capacity of 0.5 mAh cm^{-2}. Dendritic Li particles grown on (**e**) Cu, (**f**) C, (**g**) Au and (**h**) Ag substrates at 1 mA cm^{-2} with a capacity of 0.5 mAh cm^{-2}. The comparison between the upper and lower rows shows that the high uniformity of faceted Li polyhedra deposition in the coin cell. Size statistics of faceted Li particles deposited on different substrates: (**i**) Cu, (**j**) C, (**k**) Au and (**l**) Ag.

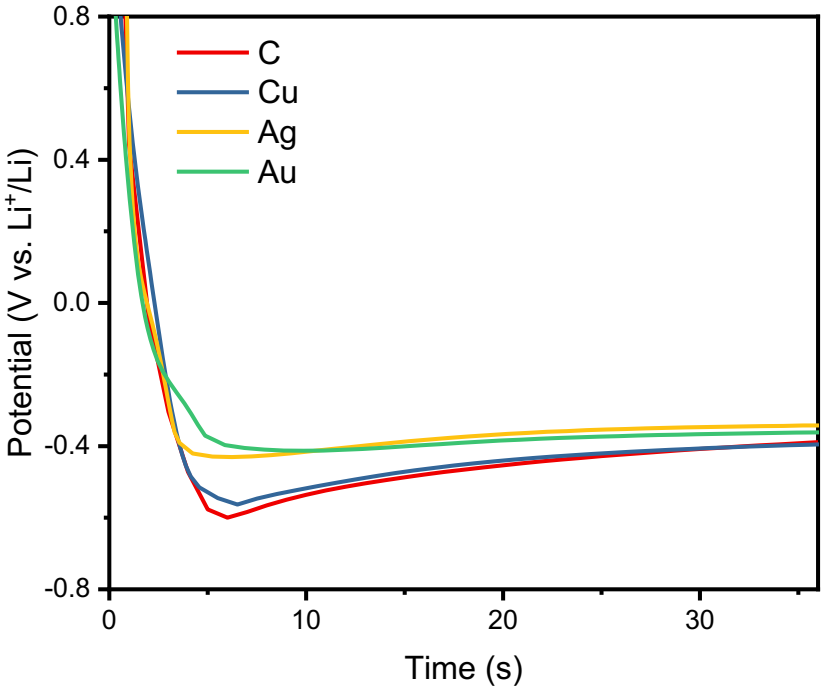

Fig. 2.20 Potential profiles of Li deposition in the coin cell at a current density of 50 mA cm^{-2} for a total capacity of 0.5 mAh cm^{-2} on different substrates.

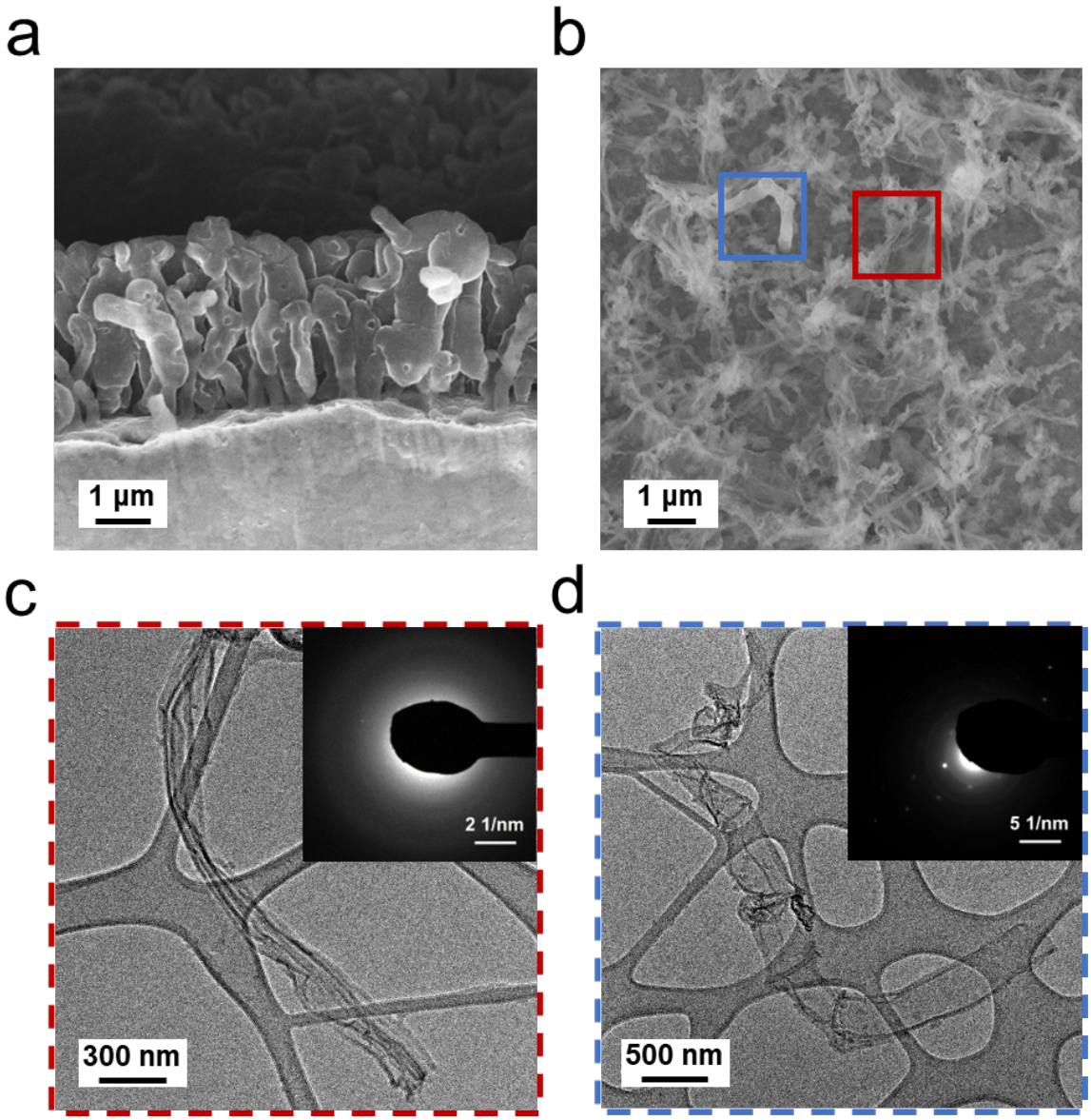

Fig. 2.21 SEM and cryo-EM showing column-like Li plating and stripping behaviors. a, Cross-sectional view of Li columns grown on Cu foil at 1 mA cm^{-2} with capacity of 0.5 mAh cm^{-2}. **b**, Cu foil with abundant empty SEI shells and limited inactive Li after stripping with 1 V cut-off voltage. **c**, Cryo-EM image of empty SEI shell. **d**, Cryo-EM image of inactive Li, inserts are SAED patterns.

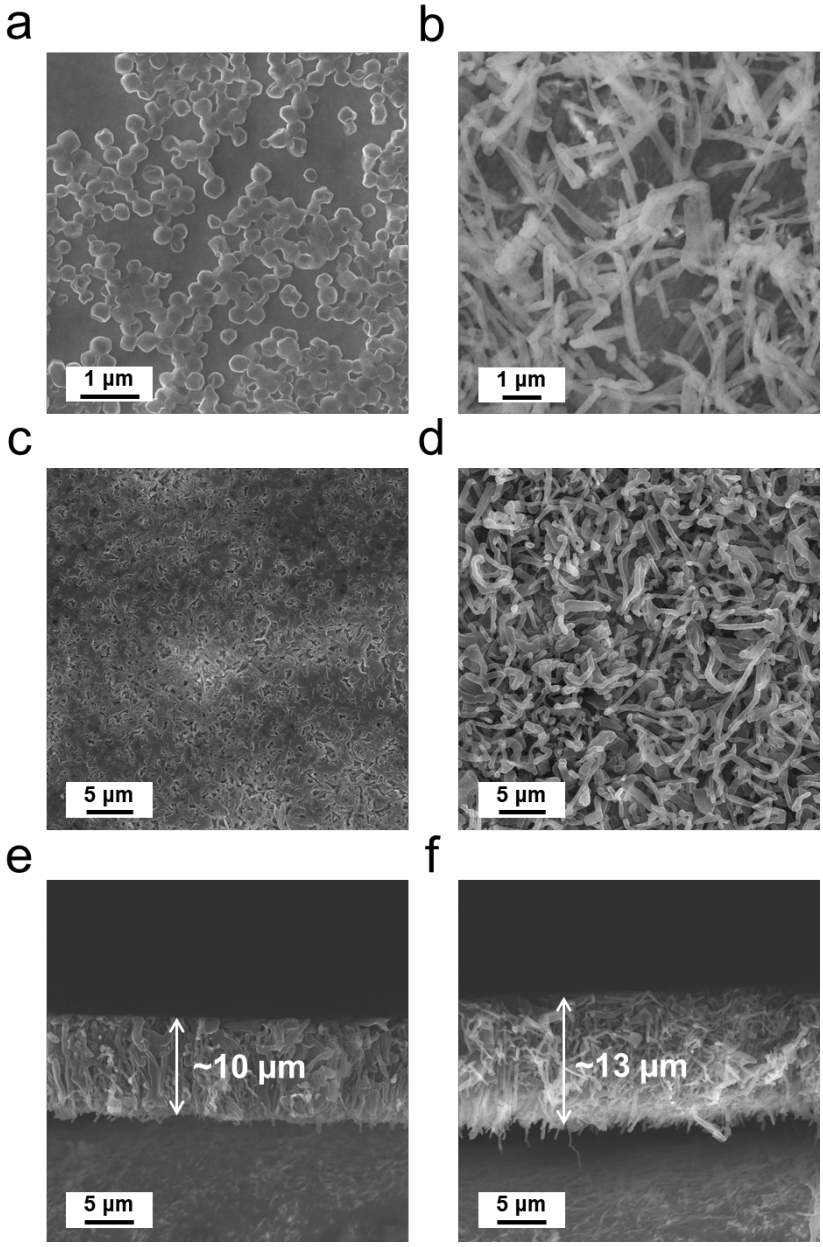

Fig. 2.22 SEM images showing Li deposition morphology with different deposition protocols in electrolyte A in coin cell geometry. Li deposition as nuclei at (**a**) 50 mA cm^{-2} and (**b**) 1 mA cm^{-2} with a capacity of 0.05 mAh cm^{-2}. **c**, Top view and e, cross-sectional view of Li deposition with pulse current method of combination with 50 mA cm^{-2} for 0.05 mAh cm^{-2} and followed by 1 mA cm^{-2} for 0.95 mAh cm^{-2}. **d**, Top view and f, cross-sectional view of Li deposition at 1 mA cm^{-2} with a capacity of 1 mAh cm^{-2}.

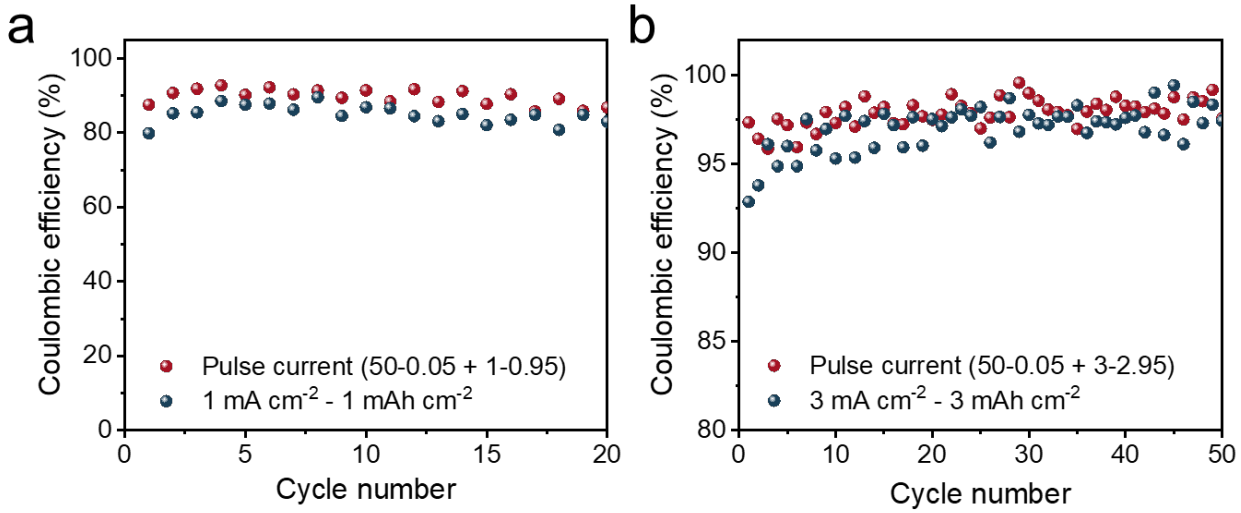

Fig. 2.23 CE comparison between pulse current protocol and normal current density. a, 1 mA cm^{-2} with a capacity of 1 mAh cm^{-2} in electrolyte A (typical electrolyte with normal performance). **b**, 3 mA cm^{-2} with a capacity of 3 mAh cm^{-2} in electrolyte C (well-performed electrolyte).

CE quantifies the reversibility of Li deposition and stripping and is a key metric for battery performance. Despite the uniform deposits of Li rhombic dodecahedra, we find that the CE decreases significantly when cycled at 50 mA cm^{-2} compared with CE at 1 mA cm^{-2} (Fig. 2.16e). Cross-sectional SEM (Fig. 2.16f) and cryo-EM (Fig. 2.16g) of the Li rhombic dodecahedra reveal a poor electrical connection with the substrate, which results in dead Li formation during cycling. In contrast, the column-like Li morphologies observed at 1 mA cm^{-2} appear to have more intimate contact with the substrate (Fig. 2.21a). After stripping to 1 V, SEM and cryo-EM imaging show that mostly empty SEI shells remain with limited inactive Li (Fig. 2.21b–d). However, large amounts of remaining Li metal can be observed after stripping at 50 mA cm^{-2} (Fig. 2.16h). Detailed cryo-EM images show that the rhombic dodecahedron morphology cannot be fully

stripped due to poor electrical contact with the substrate, instead exhibiting a partially shrunken structure (Fig. 2.16i). This indicates that the inactive Li formed through electrical disconnection with the current collector contributes to the decreased CE. Despite this poor initial contact between Li rhombic dodecahedra and the current collector, we can still leverage the well-defined Li {110} surfaces of the Li polyhedra for improved deposition morphology and battery performance. Specifically, we use a pulse-current deposition approach in electrolyte A to first nucleate Li rhombic dodecahedra at ultrafast current densities (50 mA cm^{-2} for 0.05 mAh cm^{-2}) followed by Li growth at normal current densities (1 mA cm^{-2} for 0.95 mAh cm^{-2}) for a total areal capacity of 1 mAh cm^{-2}. SEM images show that Li rhombic dodecahedra are indeed formed after ultrafast deposition (Fig. 2.22a), which serves as a well-defined nucleation surface and facilitates the subsequent growth of dense Li metal during the normal current density deposition (Fig. 2.22c,e). In contrast, constant current deposition at 1 mA cm^{-2} for a capacity of 1 mAh cm^{-2} results in highly dendritic and porous Li morphology in the same electrolyte (Fig. 2.22d,f), leading to potential opportunities for electrical disconnection and inactive Li formation. Nucleation and growth of metallic Li on existing Li {110} surfaces of rhombic dodecahedra will result in denser Li films than Li deposition onto the bare polycrystalline Cu surface,[40] resulting in this morphology difference. Furthermore, this difference in deposition morphology between the two charging protocols results in a 5% CE increase (Fig. 2.23a) for the pulse-current protocol. For more advanced electrolytes like electrolyte C, although the baseline performance using constant current is already high, we still observe an approximately 1% CE increase with the pulse-current protocol (Fig. 2.23b). This initial result highlights how our discovery of the intrinsic Li deposition morphology and its origin can be leveraged to provide important and practical implications for advancing battery research.

2.4 Conclusion

In conclusion, our work here challenges two long-standing axioms of Li electrodeposition: (1) that high current densities promote dendritic Li growth and (2) that electrolyte chemistry governs Li deposition morphology. During ultrafast electrodeposition that avoids Li^+ depletion, our UME and cryo-EM studies reveal the intrinsic morphology of Li metal to be a non-dendritic rhombic dodecahedron, which is independent of electrolyte chemistry and matches the theoretical Wulff construction of a bcc crystal. Furthermore, we demonstrate how such current density regimes can induce unique failure modes that can be mitigated through a pulse-charging protocol. By outpacing SEI formation and decoupling it from Li metal growth, we open up new opportunities to explore how reactive metal deposition fundamentally proceeds without the influence of a surface corrosion film and its impact on battery operation.

2.5 Method

Preparation of electrolyte solutions

LiDFOB (Sigma-Aldrich, ⩾99%), $LiBF_4$ (Sigma-Aldrich, ⩾98%), $LiAsF_6$ (Sigma-Aldrich, 98%), $LiPF_6$ (Thermo Scientific Chemicals, 98%) and LiFSI (Canrd, 99.5%) were dried at 65 °C overnight before using. FEC (Alfa Aesar, 98%) and DEC (Sigma-Aldrich, 99%) were added to obtain a solution of 0.6 M LiDFOB and 0.6 M $LiBF_4$ (0.6 M LiDFOB and 0.6 M $LiBF_4$ in 1:1 v/v FEC/DEC). Similarly, PC (Alfa Aesar, 99%) and FEC were added to obtain a solution of 1 M $LiPF_6$ in PC with 2 wt% $LiAsF_6$ and 2 wt% FEC. DME (Sigma-Aldrich, 99.5%) was added to obtain a 4 M solution of LiFSI (4 M LiFSI in DME). $LiPF_6$ solution in EC and DEC (1 M $LiPF_6$ in 1:1 v/v EC/DEC) was directly purchased from Sigma-Aldrich with battery grade. All chemicals

were used as received without further purification. All electrolytes were made and stored in the Ar-filled glove box ($O_2 < 0.2$ ppm, $H_2O < 0.02$ ppm).

Preparation of UME electrodes

A tungsten (W) wire (Goodfellow, 99.95%) of 25 μm in diameter was threaded through the borosilicate glass pipet. The glass pipet tip was carefully melted using a butane torch lighter to achieve a perfect glass-to-metal sealing,[41] which should prevent any leakage and bubbles between glass insulation and the W wire. Copper (Cu) wire was electrically connected to sealed W wire using silver paste and served to connect with potentiostat (BioLogic VMP3). The open space of the electrode was filled with insulating epoxy. The prepared UME electrode was polished with a 0.1 micron diamond lapping disc and rinsed with ultrapure water (18.25 MΩ cm^{-1}) and acetone before each experiment. Once dry, UME electrodes were placed in the glove box for usage. The Cu UME electrode was constructed similarly to W UME, except that 25-μm W wire was replaced by Cu wire of 255 μm in diameter.

Electrochemical experiments

The UME-based reactor is a 20-ml beaker cell with 2 ml electrolyte and consists of two electrodes, where the UME electrode served as the working electrode and Li foil (0.75 mm thick, Alfa Aesar, 99.9%) of 10 mm in diameter was used as the counter/reference electrode. Li metal with a capacity of 0.5 mAh cm^{-2} was deposited onto the working electrode by applying a constant current of 10 to 1,000 mA cm^{-2}.

In Li||Cu 2032-type coin cells, Cu foil (10 μm thick, Canrd, 99%) of 4 mm in diameter served as the working electrode, and Li foil of 2 mm in diameter served as the counter/reference electrode to avoid mass transport limitations at high current densities needed to outpace SEI formation. Cu foil was rinsed with ultrapure water and acetone to remove surface contaminants before transferring into the glove box. Li foil was mechanically sheared using a polyethylene scraper to remove the surface oxide and improve electrical connection to the stainless steel coin cell case. Sixty microliters of electrolyte was added to each cell using a 25-μm-thick polypropylene–polyethylene–polypropylene separator (Celgard 2325) to divide the two electrodes. Coin cells were loaded onto a battery tester (Land Instruments) and cycled. For other current collector substrates, Ag and Au foils were prepared by e-beam evaporation with a thickness of 200 nm on Cu foil. Graphite paper was bought from Digi-Key Electronics with a thickness of 70 μm.

The assembly of symmetric Li||Li 2032-type coin cells was the same as Li||Cu cells, except that two polished and flattened 1 cm^2 discs of Li foils served as working and counter electrodes. Electrochemical impedance spectroscopy (EIS) measurements were performed at open circuit after approximately 5 min of assembly with a frequency range of 1 MHz to 0.2 Hz and a perturbation amplitude of 5 mV.

Transient LSV measurements were performed with three-electrode beaker cells with iR-correction. The W UME electrode served as the working electrode, while the Li foil of 10 mm in diameter was used for both the counter and reference electrode. The W UME electrode was swept from open circuit voltage to −1.2 V with different scan rates.[3] At the slow scan rates of 10 and 50 mV s^{-1}, we can see that no obvious peak current density is reached, suggesting that the measurement is a

steady-state voltammogram. As the scan rate was increased by three orders of magnitude (10–30 V s^{-1}), the current density–potential response changed. The current density increased sharply after overcoming the nucleation barrier, corresponding to the growth of Li metal, until a current density reached a diffusion-limited peak.

All experiments were performed in the Ar-filled glove box.

Fabrication of Cu chunks-based TEM grids by electrodeposition

Thirty-five milligrams of Cu (II) acetate ($Cu(CO_2CH_3)_2$, Acros, 99%) and 1.3 g sodium citrate tribasic dihydrate ($Na_3C_6H_5O_7 \cdot 2H_2O$, Sigma-Aldrich, ⩾99%) were added into 10 ml of ultrapure water to obtain the aqueous electrolyte. The electrodeposition reactor is a 20-ml beaker with 10 ml electrolyte and consists of two electrodes, in which a 100-mesh stainless steel TEM grid (SPI) was used as the working electrode and a graphite rod (Canrd) served as the counter electrode. Cu chunks with a capacity of 0.5 mAh were deposited onto the working electrode by applying a constant current of 10 mA for 3 min. The prepared Cu TEM grid was cleaned with ultrapure water and dried in a vacuum oven until it was placed in the glove box for use.

SEM sample preparation and imaging

After running the electrochemical experiments described above in the glove box, UME electrode, Cu foil or TEM grid working electrode was gently rinsed with a few drops of anhydrous dioxolane and then affixed to an SEM sample stage using conductive tape after drying. The SEM stage with samples was placed in a Teflon box and tightly sealed by parafilm. The pressure in the glove box and thus, the sealed box was greater than ambient pressure, which prevented air from leaking into

the box. Once taken out of the glove box, the SEM stage was quickly transferred into the SEM chamber (approximately 5 s) to avoid air exposure. All SEM characterizations were conducted using ZEISS Supra 40VP SEM with a 10-kV acceleration voltage.

Cryo-EM sample preparation and imaging

Coin cells were constructed as usual but with a customized TEM grid incorporated onto the Cu foil as the co-current collector. TEM grids with electrodeposited Cu nanostructures were used to serve as local UMEs, producing high electric fields[35] that locally concentrate electrolyte cations to promote ultrafast Li deposition with an estimated current density of 200 mA cm^{-2}, while 300-mesh Cu TEM grids were used for normal Li deposition with an estimated current density of 10 mA^{-2}. To facilitate observation of individual particles under cryo-EM, a capacity of 0.1 mAh cm^{-2} was applied for all cryo-EM samples. After assembling the coin cell in an Ar-filled glove box, the TEM grid was carefully rinsed with a few drops of anhydrous dioxolane. Once dry, the TEM grid with deposited Li was placed in an Eppendorf tube sealed with parafilm and transferred out of the glove box. The pressure in the glove box and thus, the sealed tube was greater than ambient pressure, which prevented air from leaking into the tube. Outside the glove box, pincer pliers held the sealed Eppendorf tube and plunged it quickly into a bath of liquid nitrogen; then, they quickly crushed open the tube after 3 s while still immersed in the liquid nitrogen to expose the grid with deposited Li to cryogen immediately. The grid was stored in a cryo-grid box in liquid nitrogen dewar for usage.

To proceed with cryo-EM imaging, the TEM grid was mounted onto a Gatan 626 TEM cryo-transfer holder using a cryo-transfer station to make sure the whole process took place under liquid

nitrogen. The built-in shutter on the transfer holder was kept closed to prevent air exposure and ice condensation on the sample when inserting the holder into the TEM column (approximately 1 s). A liquid nitrogen dewar attached to the holder maintained the grid at cryogenic temperature (approximately −178 °C) during the whole imaging process. All cryo-EM characterizations were carried out using an FEI Titan 80–300 scanning transmission electron microscope operated at 300 kV. The microscope was equipped with a field-emission gun, an energy-dispersive X-ray spectroscopy detector and an ultrascan 2 × 2 K digital camera. During cryo-EM images acquisition, the corresponding electron dose flux was also recorded. Electron dose rate is less than 100 e $Å^{-2}$ s^{-1} for low magnification cryo-EM images and less than approximately 1,000 e $Å^{-2}$ s^{-1} for high-resolution cryo-EM images. The electron beam exposure time of each image is no more than 30 s, and the acquisition time is 0.4 to 1 s.

EIS fitting

The Nyquist plot (Fig. 2.12d) displays two distinct semicircles. One semicircle comprises the high- to midfrequency range (that is, more than 20 Hz) that is typically attributed to Li^+ transport through the compact SEI layer. The second semicircle corresponds to the low-frequency range (that is, less than 20 Hz) that is attributed to transport through the extended SEI, which comprises electrolyte degradation products not directly interfacing with the metallic Li.[7] The extended SEI is not a rate-determining step for Li^+ transfer. Therefore, the fitting process was performed for the high- to midfrequency range (the first semicircle) corresponding to the compact SEI layer directly interfaced with the Li metal. This is a reasonable approximation and has been used in previous studies[25,42] quantifying Li^+ transport through the SEI film. Although there are a number of equivalent circuit models[43,44] for SEI that give similar results, we chose a particular model (Fig.

2.12d) that is relatively simple for the charge transfer process of the SEI on empirical analysis.[45,46] In addition, this equivalent circuit has recently been leveraged for its simplicity and accuracy in extracting physical parameters and predicting properties of a model SEI system.[42] A schematic of the SEI model corresponding to the equivalent circuit is shown in Fig. 2.14, and the fitting process was completed using the ZFit unit in EC-Lab software. The equivalent circuit consists of a resistor (R_{SEI}) representing the resistance of Li^+ transport through the SEI, a capacitor (C_{SC}) representing the space charge capacitance, a capacitor (C_{SEI}) representing the dielectric response of the SEI and a Warburg diffusion element (W) representing Li^+ diffusion through the SEI. The interfacial charge transfer kinetics (that is, $Li^+ + e^- \rightarrow Li^0$) was neglected in this equivalent circuit since previous study suggested that this is a reasonable approximation.[3] Based on the above circuit model and fitting the result of EIS, we calculate an SEI ionic resistance of $R_{SEI} = 115\ \Omega$.

Ionic transport parameters calculation through the SEI

The conductivity of the SEI (λ_{SEI}) is calculated by

$$\lambda_{SEI} = \frac{l_{SEI}}{R_{SEI}A} = 1.4 \times 10^{-8}\ (\Omega\ cm)^{-1}$$

where l_{SEI} is the SEI thickness measured by statistics from cryo-EM images (Fig. 2.11d) and A is the electrode area. Traditionally, the Nernst–Einstein equation establishes a relationship between ionic conductivity and ion diffusion coefficients. Thus, experimental measurements of SEI conductivity can be used to calculate ion diffusion coefficients according to the Nernst–Einstein equation, which has been widely adopted by the battery community.[42]

The diffusion coefficient of Li^+ through SEI ($D_{Li^+}^{SEI}$) is calculated by

$$D_{Li^+}^{SEI} = (\lambda_{SEI} Z_W A)^2 = 4.4 \times 10^{-9}\ cm^2 s^{-1}$$

where Z_W is the Warburg element, and it was obtained from the EIS equivalent circuit fitting.

The carrier concentration (n) of Li^+ in the SEI is calculated by the Nernst–Einstein equation,

$$n = \frac{\lambda_{SEI} RT}{F^2 D_{Li^+}^{SEI}} = 8.4 \times 10^{-7}\ mol\ cm^{-3}$$

where T is the temperature, R is the standard gas constant and F is the Faraday constant.

The above calculated results are consistent with previous studies of Li^+ transport in the SEI.[37,42]

Diffusion coefficient of Li^+ through electrolyte D_{Li^+} calculation

For a total irreversible one-step, one-electron reaction ($Li^+ + e^- \rightarrow Li$), the Nernst equation and boundary condition can be used to calculate the relationship between peak current density J_p and the effective diffusion coefficient D_{Li^+}:

$$J_p = (2.99 \times 10^5)\alpha^{1/2} C_{Li^+}^* D_{Li^+}^{1/2} v^{1/2}$$

where α is the transfer coefficient and $C_{Li^+}^*$ is the bulk concentration of Li^+.

The transfer coefficient describes how strong the rate of an electrochemical reaction depends on the applied potential. In most electrochemical systems, the transfer coefficient is assumed to be constant and typically lies between 0.3 and 0.7. It is approximated as 0.5 in the absence of actual measurements:

$$D_{Li^+} = 3 \times 10^{-6}\ cm^2 s^{-1}$$

COMSOL Multiphysics simulations

The simulations are performed on COMSOL Multiphysics v.5.6 using the physics module of 'Electrochemistry-Battery' and Butler–Volmer expressions of hydrodynamics. Due to three-dimensional cell geometry being symmetrical along the height of the battery, a two-dimensional cross-section is used to model the three-dimensional geometry of the battery. The electrochemical model consists of an electrolyte domain and two electrode boundaries. Since the electronic conductivity of Cu and Li metal is very high and the electrochemical deposition reactions only take place at the surface of the Cu electrode, the thickness of metal is neglected in the model geometry. In UME geometry, the module of electric field distribution is $500 \times 2{,}000\ \mu m^3$ with the standard electrolyte of 1 M $LiPF_6$ in 1:1 v/v EC/DEC running at a current density of 1,000 mA cm^{-2} at 298 K. Parameters (for example, ionic conductivity, viscosity and so on) of the electrolyte for simulation are given in Table 2.1. The designed working electrode is 25 μm in diameter, and other parts are set to be insulated. In coin cell geometry, the module of electric field distribution is $50 \times 2{,}000\text{-}\mu m^3$ filling with the same electrolyte running at a current density of 50 mA cm^{-2} at 298 K. The time-dependent simulation is applied, and an initialization study step is used to calculate the initial potentials in the cell; 1.8-s (UME geometry) and 36-s (coin cell geometry) time-dependent solvers are set up to store the solution at 0.1-s intervals.

Table 2.1 Parameters of the electrolyte A for COMSOL Multiphysics simulation.

Parameters	Value	Reference
Viscosity	4.4 mPa s^{-1}	47
Ionic conductivity	0.74 S m^{-1}	48

Density	1.293 kg m^{-3}	49

Supplementary Discussion on Minimum Current Density

The **minimum current density** is the lowest current density needed to outpace SEI influence and transition from ill-defined Li morphologies to form well-defined Li rhombic dodecahedra. This minimum current density is not the same for all systems and will depend on cell geometry, temperature, cell pressure, electrolyte chemistry, and other parameters. For example, key differences between coin cell and UME geometries exist that may change the current density needed to outpace SEI influence: (1) the distance between working electrode and counter electrode (~500 µm vs. ~25 µm); (2) cell pressure; and (3) existence (or absence) of a separator impinging on the current collector surface area. **To clarify, our manuscript's goal is not to identify or understand the differences in minimum current density between the coin cell and UME geometry (or other factors), as it will vary depending on the factors listed above.** However, we present an approach that can identify an estimate of this minimum current density. Preliminary UME results (Fig. 2.6) at 50, 150, and 200 mA cm^{-2} in electrolyte A show that faceted polyhedra morphology begins to appear at a current density of 50 mA cm^{-2}, which also produces Li deposits with dendritic morphology. We observe that 200 mA cm^{-2} is the lowest current density to produce **only** rhombic dodecahedron morphology without Li dendrites. This suggests that for electrolyte A, 200 mA cm^{-2} is the minimum current density required to outpace SEI formation in a UME geometry. **We emphasize that a complete understanding of how minimum current density varies with cell geometry and other factors (e.g., temperature, cell pressure, electrolyte chemistry) is beyond the scope of our present manuscript.** Indeed, distinguishing the minimum current density in our coin cell or UME geometry does not impact our manuscript's conclusion,

which is that once SEI influence has been outpaced, the intrinsic Li rhombic dodecahedra morphology is formed.

2.6 References

1 Liu, B., Zhang, J.-G. & Xu, W. Advancing Lithium Metal Batteries. *Joule* **2**, 833-845 (2018).

2 Peled, E. The Electrochemical Behavior of Alkali and Alkaline Earth Metals in Nonaqueous Battery Systems—The Solid Electrolyte Interphase Model. *J. Electrochem. Soc.* **126**, 2047–2051 (1979).

3 Boyle, D. T. et al. Transient Voltammetry with Ultramicroelectrodes Reveals the Electron Transfer Kinetics of Lithium Metal Anodes. *ACS Energy Lett.* **5**, 701-709 (2020).

4 Li, Y. et al. Atomic structure of sensitive battery materials and interfaces revealed by cryo–electron microscopy. *Science* **358**, 506-510 (2017).

5 Li, Y. et al. Correlating Structure and Function of Battery Interphases at Atomic Resolution Using Cryoelectron Microscopy. *Joule* **2**, 2167-2177 (2018).

6 Li, Y., Li, Y. & Cui, Y. Catalyst: How Cryo-EM Shapes the Development of Next-Generation Batteries. *Chem.* **4**, 2250-2252 (2018).

7 Zhang, E. et al. Expanding the cryogenic electron microscopy toolbox to reveal diverse classes of battery solid electrolyte interphase. *iScience* **25**, 105689 (2022).

8 Fang, C. et al. Quantifying inactive lithium in lithium metal batteries. *Nature* **572**, 511-515 (2019).

9 Lin, D., Liu, Y. & Cui, Y. Reviving the lithium metal anode for high-energy batteries. *Nat. Nanotechnol.* **12**, 194-206 (2017).

10 Xu, W. et al. Lithium metal anodes for rechargeable batteries. *Energy Environ. Sci.* **7**, 513-537 (2014).

11 Liu, B. et al. Coupling a Sponge Metal Fibers Skeleton with In Situ Surface Engineering to Achieve Advanced Electrodes for Flexible Lithium-Sulfur Batteries. *Adv. Mater.* **32**, e2003657 (2020).

12 Peled, E. & Menkin, S. Review—SEI: Past, Present and Future. *J. Electrochem. Soc.* **164**, A1703-A1719 (2017).

13 Bai, P., Li, J., Brushett, F. R. & Bazant, M. Z. Transition of lithium growth mechanisms in liquid electrolytes. *Energy Environ. Sci.* **9**, 3221-3229 (2016).

14 Ren, X. et al. Guided Lithium Metal Deposition and Improved Lithium Coulombic Efficiency through Synergistic Effects of LiAsF6 and Cyclic Carbonate Additives. *ACS Energy Lett.* **3**, 14-19 (2017).

15 Zhang, Y. et al. Dendrite-free lithium deposition with self-aligned nanorod structure. *Nano Lett.* **14**, 6889-6896 (2014).

16 Qian, J. et al. Dendrite-free Li deposition using trace-amounts of water as an electrolyte additive. *Nano Energy* **15**, 135-144 (2015).

17 Weber, R. et al. Long cycle life and dendrite-free lithium morphology in anode-free lithium pouch cells enabled by a dual-salt liquid electrolyte. *Nat. Energy* **4**, 683-689 (2019).

18 Zhang, W. et al. Colossal Granular Lithium Deposits Enabled by the Grain-Coarsening Effect for High-Efficiency Lithium Metal Full Batteries. *Adv. Mater.* **32**, e2001740 (2020).

19 Qian, J. et al. High rate and stable cycling of lithium metal anode. *Nat. Commun.* **6**, 6362 (2015).

20 Zhou, S. et al. Incorporation of LiF into functionalized polymer fiber networks enabling high capacity and high rate cycling of lithium metal composite anodes. *Chem. Eng. J.* **404**, 126508 (2021).

21 Zheng, J. et al. Regulating electrodeposition morphology of lithium: towards commercially relevant secondary Li metal batteries. *Chem. Soc. Rev.* **49**, 2701-2750 (2020).

22 Xu, K. Nonaqueous Liquid Electrolytes for Lithium-Based Rechargeable Batteries. *Chem. Rev.* **104**, 4303-4418 (2004).

23 Odziemkowski, M. & Irish, D. E. An Electrochemical Study of the Reactivity at the Lithium Electrolyte/Bare Lithium Metal Interface: I . Purified Electrolytes. *J. Electrochem. Soc.* **139**, 3063-3074 (1992).

24 Verbrugge, M. W. & Koch, B. J. Microelectrode investigation of ultrahigh-rate lithium deposition and stripping. *J. Electroanal. Chem.* **367**, 123-129 (1994).

25 Boyle, D. T. et al. Resolving Current-Dependent Regimes of Electroplating Mechanisms for Fast Charging Lithium Metal Anodes. *Nano Lett.* **22**, 8224–8232 (2022).

26 Boyle, D. T. et al. Correlating Kinetics to Cyclability Reveals Thermodynamic Origin of Lithium Anode Morphology in Liquid Electrolytes. *J. Am. Chem. Soc.* **144**, 20717-20725 (2022).

27 Mao, H. et al. Current-Density Regulating Lithium Metal Directional Deposition for Long Cycle-Life Li Metal Batteries. *Angew. Chem. Int. Ed.* **60**, 19306-19313 (2021).

28 Jiang, F. & Peng, P. Elucidating the Performance Limitations of Lithium-ion Batteries due to Species and Charge Transport through Five Characteristic Parameters. *Sci. Rep.* **6**, 32639 (2016).

29 Du, Z., Wood, D. L., Daniel, C., Kalnaus, S. & Li, J. Understanding limiting factors in thick electrode performance as applied to high energy density Li-ion batteries. *J. Appl. Electrochem.* **47**, 405-415 (2017).

30 Jurng, S., Brown, Z. L., Kim, J. & Lucht, B. L. Effect of electrolyte on the nanostructure of the solid electrolyte interphase (SEI) and performance of lithium metal anodes. *Energy Environ. Sci.* **11**, 2600-2608 (2018).

31 Cao, X. et al. Monolithic solid–electrolyte interphases formed in fluorinated orthoformate-based electrolytes minimize Li depletion and pulverization. *Nat. Energy* **4**, 796-805 (2019).

32 Yu, Z. et al. Molecular design for electrolyte solvents enabling energy-dense and long-cycling lithium metal batteries. *Nat. Energy* **5**, 526-533 (2020).

33 Pei, A., Zheng, G., Shi, F., Li, Y. & Cui, Y. Nanoscale Nucleation and Growth of Electrodeposited Lithium Metal. *Nano Lett.* **17**, 1132-1139 (2017).

34 Sekerka, R. F. Equilibrium and growth shapes of crystals: how do they differ and why should we care? *Cryst. Res. Technol.* **40**, 291-306 (2005).

35 Liu, M. et al. Enhanced electrocatalytic CO2 reduction via field-induced reagent concentration. *Nature* **537**, 382-386 (2016).

36 He, X. et al. The passivity of lithium electrodes in liquid electrolytes for secondary batteries. *Nat. Rev. Mater.* **6**, 1036-1052 (2021).

37 Gunnarsdóttir, A. B., Vema, S., Menkin, S., Marbella, L. E. & Grey, C. P. Investigating the effect of a fluoroethylene carbonate additive on lithium deposition and the solid electrolyte interphase in lithium metal batteries using in situ NMR spectroscopy. *J. Mater. Chem. A* **8**, 14975-14992 (2020).

38 Yan, K. et al. Selective deposition and stable encapsulation of lithium through heterogeneous seeded growth. *Nat. Energy* **1**, 1-8 (2016).

39 Behling, C., Mayrhofer, K. J. J. & Berkes, B. B. Formation of lithiated gold and its use for the preparation of reference electrodes — an EQCM study. *J. Solid State Electrochem.* **25**, 2849-2859 (2021).

40 Hu, X., Gao, Y., Zhang, B., Shi, L. & Li, Q. Superior cycle performance of Li metal electrode with {110} surface texturing. *EcoMat* **4**, e12264 (2022).

41 Sur, U. K., Dhason, A. & Lakshminarayanan, V. A Simple and Low-Cost Ultramicroelectrode Fabrication and Characterization Method for Undergraduate Students. *J. Chem. Educ.* **89**, 168-172 (2011).

42 Guo, R. & Gallant, B. M. Li2O Solid Electrolyte Interphase: Probing Transport Properties at the Chemical Potential of Lithium. *Chem. Mater.* **32**, 5525-5533 (2020).

43 E. Peled, D. G. a. G. A. Advanced Model for Solid Electrolyte Interphase Electrodes in Liquid and Polymer Electrolytes. *J. Electrochem. Soc.* **144**, L208 (1997).

44 Mark W. Verbrugge & Koch, B. J. Microelectrode Study of the Lithium/Propylene Carbonate Interface: Temperature and Concentration Dependence of Physicochemical Parameters. *J. Electrochem. Soc.* **141**, 3053-3059 (1994).

45 A. V. Churikov, I. M. Gamayunova & Shirokov, A. V. Ionic processes in solid-electrolyte passivating films on lithium. *J. Solid State Electrochem.* **4**, 216–224 (2000).

46 Alexei V. Churikov, Eugeny S. Nimon & Lvov, A. L. Impedance of Li-Sn, Li-Cd and Li-Sn-Cd alloys in propylene carbonate solution. *Electrochim. Acta* **42**, 179-189 (1997).

47 Kerner, M., Plylahan, N., Scheers, J. & Johansson, P. Ionic liquid based lithium battery electrolytes: fundamental benefits of utilising both TFSI and FSI anions? *Phys. Chem. Chem. Phys.* **17**, 19569-19581 (2015).

48 Feng, Z., Higa, K., Han, K. S. & Srinivasan, V. Evaluating Transport Properties and Ionic Dissociation of LiPF6in Concentrated Electrolyte. *J. Electrochem. Soc.* **164**, A2434-A2440 (2017).

49 Landesfeind, J. et al. Comparison of Ionic Transport Properties of Non-Aqueous Lithium and Sodium Hexafluorophosphate Electrolytes. *J. Electrochem. Soc.* **168**, 040538 (2021).

Chapter 3: Engineering battery corrosion films by tuning electrical double layer composition

Reprinted (adapted) with permission from Yuan, X.; Cheng, D.; Liu, B.; Liang, Kaiyan.; Liang, Keyue.; Yu, J.; Mecklenburg, M.; Sautet, P.; Li, Y. Engineering battery corrosion films by tuning electrical double layer composition. *Joule* **8**, 3038-3053 (2024). https://doi.org/10.1016/j.joule.2024.07.011.

3.1 Abstract

Battery performance is strongly influenced by the solid electrolyte interphase (SEI) that forms from electrolyte decomposition and remains a key target for engineering design. Whereas traditional approaches to tune the SEI have focused on electrolyte chemistry, we show that manipulating the electric field offers a novel approach. Here, we change the electrical double layer (EDL) composition by either applying or removing the local electric field, which directly controls SEI formation. Surprisingly, the solvent-derived SEI known to form in a conventional electrolyte exhibits anion-enhanced chemistry when the electric field is removed, which is attributed to the Coulombic interaction between the electric field and free anions. With the electric field control, we produce an anion-enhanced SEI in conventional electrolytes that demonstrates improved battery cycling and corrosion resistance. Together, our findings highlight the importance of EDL composition and demonstrate electric field strength as a new parameter to tune SEI structure and chemistry.

3.2 Introduction

Next-generation batteries with energy density beyond that of Li-ion largely depend on the Li metal anode, which is electrodeposited and stripped upon charging and discharging, respectively.[1,2] The

reversibility of this electrodeposition process governs the performance of Li metal batteries but is complicated by electrolyte decomposition, resulting in the formation of the solid electrolyte interphase (SEI).[3,4,5] The SEI layer is ionically conductive yet electronically insulating, conformally passivating the Li metal surface from uncontrolled and continuous degradation.[6,7] The degree of passivation is believed to depend on the SEI chemistry, which is directly influenced by the components within the electrical double layer (EDL) that are decomposed to form the SEI.[8,9,10,11] For example, SEI chemistries derived from anion decomposition (i.e., anion-derived SEI) have been shown to enable much higher cycling efficiencies and Li electrodeposition reversibility than SEI chemistries derived from solvent decomposition (i.e., solvent-derived SEI).[12,13,14,15,16] As a result, producing anion-derived SEI films has emerged as a key design principle in Li metal battery research. One of the approaches for forming anion-derived SEI films has been to engineer the solvation structure of Li ions to contain more anions by using weakly solvating solvents or ultrahigh concentration regimes.[17,18,19] This allows for anions within the solvation shell of Li ions to remain at the EDL interface for decomposition and incorporation into the SEI film. By contrast, the free, unsolvated anions in conventional electrolytes with solvent-dominated Li^+ solvation shells are mostly repelled from the Helmholtz layer by the negative potentials applied[20] during Li electrodeposition, resulting in SEI films that are predominantly solvent-derived (Fig. 3.1a). While tuning the solvation structure has led to improvements in Li metal battery performance, it remains an indirect approach to control the composition of the EDL, which is what truly governs the SEI chemistry. Introducing desired decomposing components into the EDL[20,21] would enable more direct control over the resulting SEI chemistry and overall battery performance.

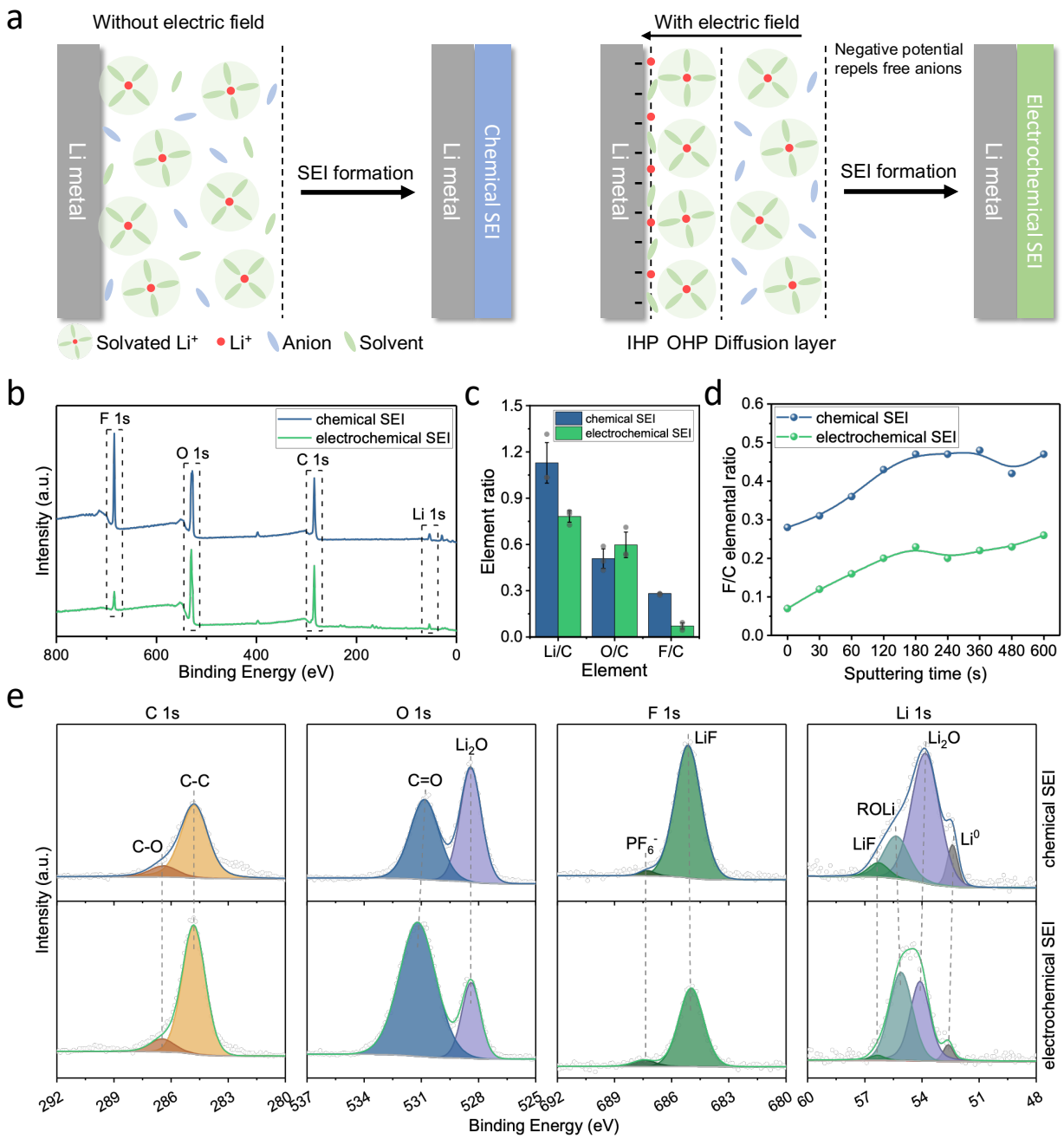

Fig. 3.1 Scheme and XPS analysis on chemical and electrochemical SEI showing that chemical SEI comprises more inorganic components in 1 M $LiPF_6$ in EC/DEC. a, Scheme of chemical and electrochemical SEI formation processes. In the absence of an electric field, solvated Li^+, free anions, and solvents are stochastic distributed (left). With applied electric field, inner Helmholtz plane (IHP) consists of desolvated Li^+ and solvents, while outer Helmholtz plane (OHP)

is occupied by Li solvation structures, with free anions being repelled from the Helmholtz layer. **b**, XPS survey. **c**, The elemental ratios in the SEI calculated from XPS suvey. **d**, The elemental ratio of F/C obtained in the XPS depth profiles. **e**, High-resolution XPS spectra and fittings of C 1s, O 1s, F 1s, and Li 1s.

In this work, we show that the EDL composition and resulting SEI can be directly tuned by modulating the electric field, resulting in different SEI chemistry and structure in the same electrolyte system. We modify the electric field by changing the polarization of the Li metal surface. For example, the anode surface is negatively polarized during galvanostatic electrodeposition of Li metal, establishing an electric field that facilitates electrochemical decomposition of electrolyte to form the SEI layer. In the presence of an electric field, we term this SEI layer an "electrochemical SEI" (Fig. 3.1a). By contrast, an electric field is absent when the Li metal surface is not polarized. Any SEI formed on a non-polarized, pristine Li metal surface is then due to chemical decomposition, and we term this the "chemical SEI" (Fig. 3.1a). In this study, we compare chemical and structural differences between chemical SEI (electric field absent) and electrochemical SEI (electric field present). 1 M lithium hexafluorophosphate ($LiPF_6$) in 1:1 v/v ethylene carbonate (EC)/diethyl carbonate (DEC) is an appropriate model system to study how the electric field can influence the EDL composition. In this electrolyte, the dipole-ion interactions between Li^+ and solvent result in reduced likelihood of salt anions being solvated by Li^+ such that the inner layer of the Li^+ solvation structure is dominated by EC, while PF_6^- ions are excluded.[22,23] Consequently, EC tends to decompose on the Li metal surface, forming a typical solvent-derived SEI that exhibits limited stability and mechanical properties, thus leading to a poor Coulombic efficiency (CE).[24,25] Using 1 M $LiPF_6$ in EC/DEC as a model electrolyte system, we form

electrochemical SEI (i.e., presence of an electric field) by conventional galvanostatic electrodeposition at a constant current density. In the same electrolyte, we form chemical SEI by immersing mechanically polished Li foil in liquid electrolyte. Equivalently, chemical SEI can also be formed using ultrafast Li electrodeposition, unique conditions under which SEI formation is decoupled from Li deposition. Our previous work[26] showed any SEI formed under such conditions is stepwise (i.e., chemically formed after initial Li metal nucleation).

Here, we discover that these electrochemical and chemical SEI films are distinct from one another due to either the presence or absence of an electric field changing the EDL composition. Specifically, we find that in the absence of an electric field, EDL components in a conventional electrolyte (i.e., 1 M $LiPF_6$ in EC/DEC) decompose on the Li metal surface to form an anion-enhanced SEI film (i.e., chemical SEI). This is in stark contrast to the solvent-derived SEI film formed in the same electrolyte under an applied electric field during electrodeposition (i.e., electrochemical SEI). Beyond changes in SEI chemistry, our cryogenic-electron microscopy (cryo-EM)[27] experiments show that the chemical SEI film formed without an electric field is 50% thinner than the electrochemical SEI film formed with an electric field. We attribute these structural and chemical changes in the SEI to the compositional differences in the EDL when applying or removing an electric field (i.e., repulsion of the anion), which is supported by both grand canonical density functional theory (GCDFT) simulation and in situ electrochemical surface-enhanced Raman spectroscopy (SERS) measurements. The anion-enhanced, chemical SEI formed in the absence of an electric field provides improved chemical stability and passivation compared with its solvent-derived counterpart formed in the presence of an electric field. In the context of battery performance, this chemical stability manifests in the resilience to corrosion

during 24 h calendar aging[28,29] and reduced voltage hysteresis during battery cycling. These results introduce electric field as a complementary pathway toward controlling SEI structure and chemistry, with direct implications for battery performance. More broadly, our work encourages alternative approaches to tune the EDL composition (i.e., beyond electric field and solvation structure), which will further efforts in engineering optimal SEI films for future battery chemistries.

3.3 Discussion

To reveal how the presence or absence of an electric field changes the overall chemistry of an SEI film formed in this model electrolyte, we use X-ray photoelectron spectroscopy (XPS), which can distinguish between different types of chemical bonding. Organic SEI components are typically correlated with stronger C 1s peaks, while inorganic SEI components contain more Li, O, and F signals from their respective 1s peaks (Fig. 3.1b). The ratio of Li, O, or F spectra peaks to that of C then quantifies the relative amounts of inorganic components in SEI films (Fig. 3.1c). In our model electrolyte system (i.e., 1 M $LiPF_6$ in EC/DEC), XPS spectra show that the electrochemical SEI (formed under an electric field) contains mostly organic, solvent-derived components (Fig. 3.1b,c), which is consistent with previous works.[30,31,32] High-resolution XPS scans (Fig. 3.1e) also show stronger signals in C–C (284.8 eV) and C–O (286.4 eV) bonding, which are strongly correlated with polymeric SEI components derived from the organic solvent.[30,32] By contrast, chemical SEI formed in the absence of an electric field in this same model electrolyte demonstrates enhanced inorganic components (Fig. 3.1b,c). This is evidenced by the large increase (>3-fold) in the ratio of F to C signals in the chemical SEI film, which persists throughout the thickness of the SEI film (Fig. 3.1d). High-resolution XPS scans of the F and Li (Fig. 3.1e) show that chemical SEI contains increased LiF (56.3 eV), which is known to form from the decomposition of the PF_6^-

anion.[32] Normally under an electric field, anion decomposition is disfavored in this strongly solvating electrolyte system. We show that by removing the electric field, more anions are decomposed and incorporated into the SEI as inorganic components.

In addition to changes in SEI chemistry, the electric field appears to also influence the local nanostructure of the SEI. Using cryo-EM (see experimental procedures), we find distinct differences in the (1) thickness, (2) nanostructure, and (3) chemistry of the chemical and electrochemical SEI. We determine the thickness of an SEI film by averaging ~50 cryo-EM imaging measurements taken from different regions across the deposited Li metal (Fig. 3.2a,f). Interestingly, our histogram of these SEI thicknesses (Fig. 3.2b,g) shows that the electrochemical SEI (~15 ± 2 nm) is 50% thicker than the chemical SEI (~10 ± 1 nm). This suggests that the inorganic components found in the chemical SEI are more electronically insulating, thus forming a thinner passivating SEI film than the electrochemical SEI that is more organic in nature. This passivating property of the chemical SEI has direct implications on improving battery performance (see below). Cryo-EM also reveals distinct nanostructures of chemical and electrochemical SEI films. During battery operating conditions with an applied electric field, the electrochemical SEI exhibits the classic mosaic structure (Fig. 3.2h,i and Fig. 3.3), which was originally proposed by Peled et al.[33] and directly imaged by Li et al.[34] using cryo-EM. The mosaic structure contains nanocrystalline domains (e.g., Li_2O, identified by matching lattice spacings) dispersed heterogeneously within an amorphous matrix. This distribution of nanocrystalline grains can dramatically impact the uniformity of Li-ion transport through the SEI.[35] In the absence of an electric field, the chemical SEI instead exhibits a hybrid nanostructure, a combination of the mosaic model and the multilayer model[34,36] in which the inorganic and organic domains are

arranged in an ordered, multilayer fashion (Fig. 3.2c,d and Fig. 3.4). In addition to the structural motifs of the mosaic model (e.g., nanocrystalline domains in an amorphous matrix), the chemical SEI displays an ordered distribution of Li_2O near the outer surface of the SEI film, which is a clear signature of the multilayer SEI nanostructure. This ordered SEI nanostructure improves the uniformity of Li-ion transport through the SEI, mitigating inactive Li formation during the stripping process.[35] Finally, we chemically map the various SEI films using energy-dispersive spectroscopy (EDS) in scanning transmission electron microscopy (STEM) mode to reveal a stronger presence of O and F in the chemical SEI than electrochemical SEI (Fig. 3.2e,j and Table 3.1), which is consistent with our XPS results. Together, XPS and cryo-EM show that the chemical SEI formed in the absence of the electric field has a distinct chemistry and nanostructure, which is more inorganic and anion-enhanced in nature compared with its electrochemical SEI counterpart.

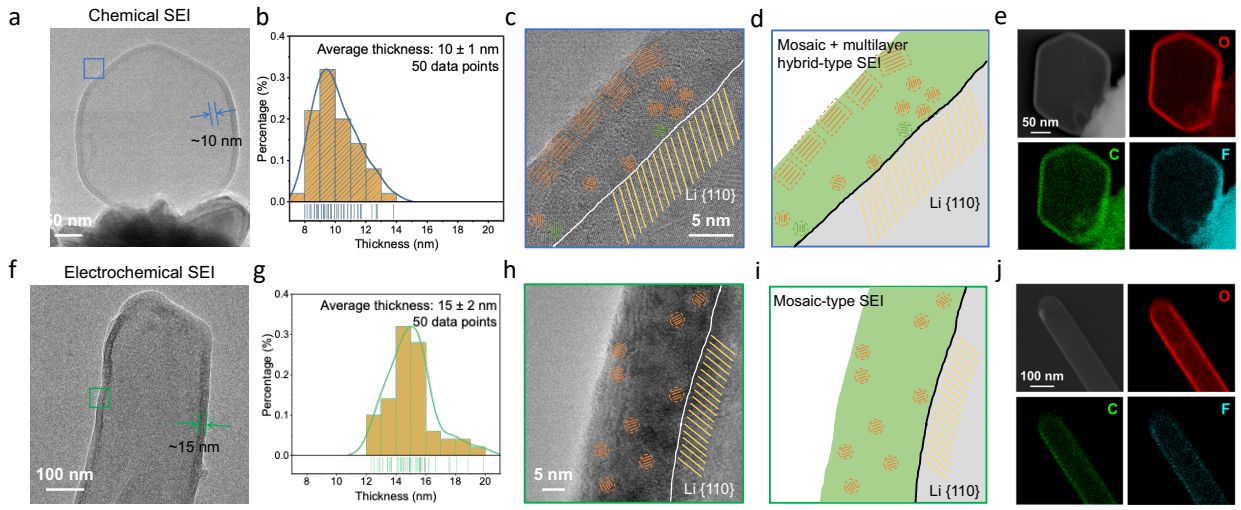

Fig. 3.2 Cryo-EM analysis on structure and chemistry of chemical and electrochemical SEI in 1 M $LiPF_6$ in EC/DEC. a, Cryo-EM image of faceted Li particle covered with a layer of chemical SEI. **b**, Thickness statistics of chemical SEI. **c**, High-resolution cryo-EM image of chemical SEI layer, magnified from the blue box in (**a**). **d**, Schematic of observed mosaic plus

multilayer hybrid type structure of chemical SEI in (**c**). **e**, STEM EDS mapping of chemical SEI. **f–j**, Analogous images to (**a–e**) but collected on electrochemical SEI.

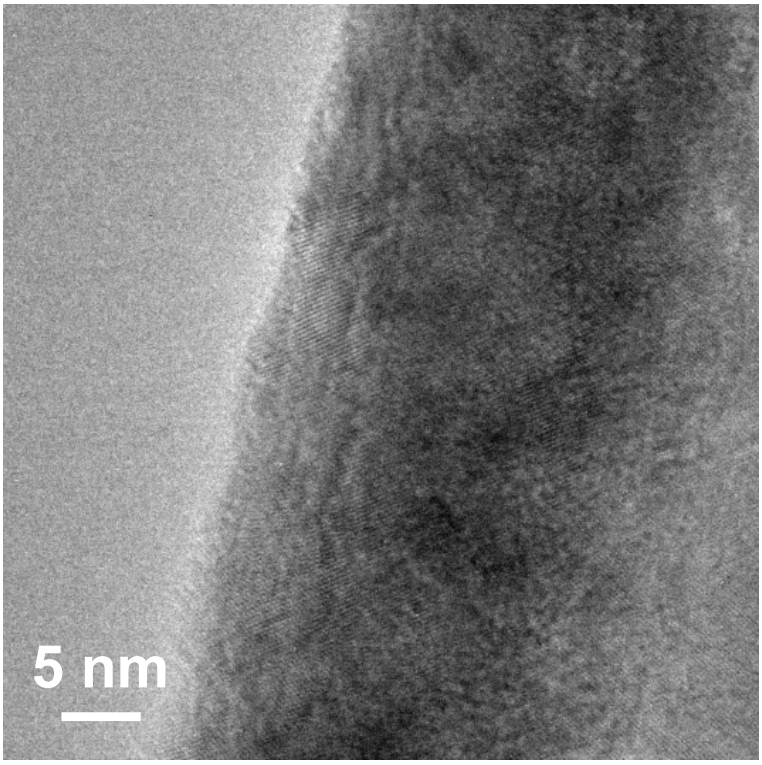

Fig. 3.3 High-resolution cryo-EM image of electrochemical SEI. Raw cryo-EM image of the electrochemical SEI formed in 1M $LiPF_6$ in EC/ DEC from Fig. 3.2h in the main text.

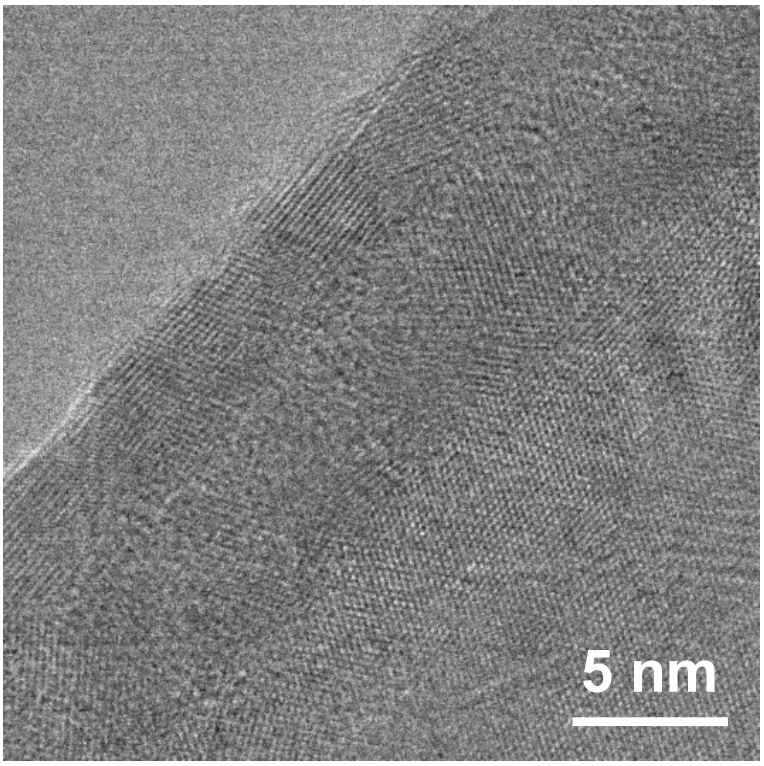

Fig. 3.4 High-resolution cryo-EM image of chemical SEI. Raw cryo-EM image of the chemical SEI formed in 1M $LiPF_6$ in EC/ DEC from Fig. 3.2c in the main text.

Table 3.1 STEM EDS elemental analysis of chemical and electrochemical SEI in 1M $LiPF_6$ in EC/DEC.

SEI type	O ratio (atom %)	C ratio (atom %)	F ratio (atom %)	F/C
Chemical SEI	77.3±3.0	18.3±3.4	4.4±1.1	0.3±0.1
Electrochemical SEI	75.5±1.2	22.7±1.0	1.8±0.2	0.1±0.005
Pulse SEI	73.0±3.8	23.5±3.0	3.5±0.8	0.2±0.02

*Each result contains more than three data points.

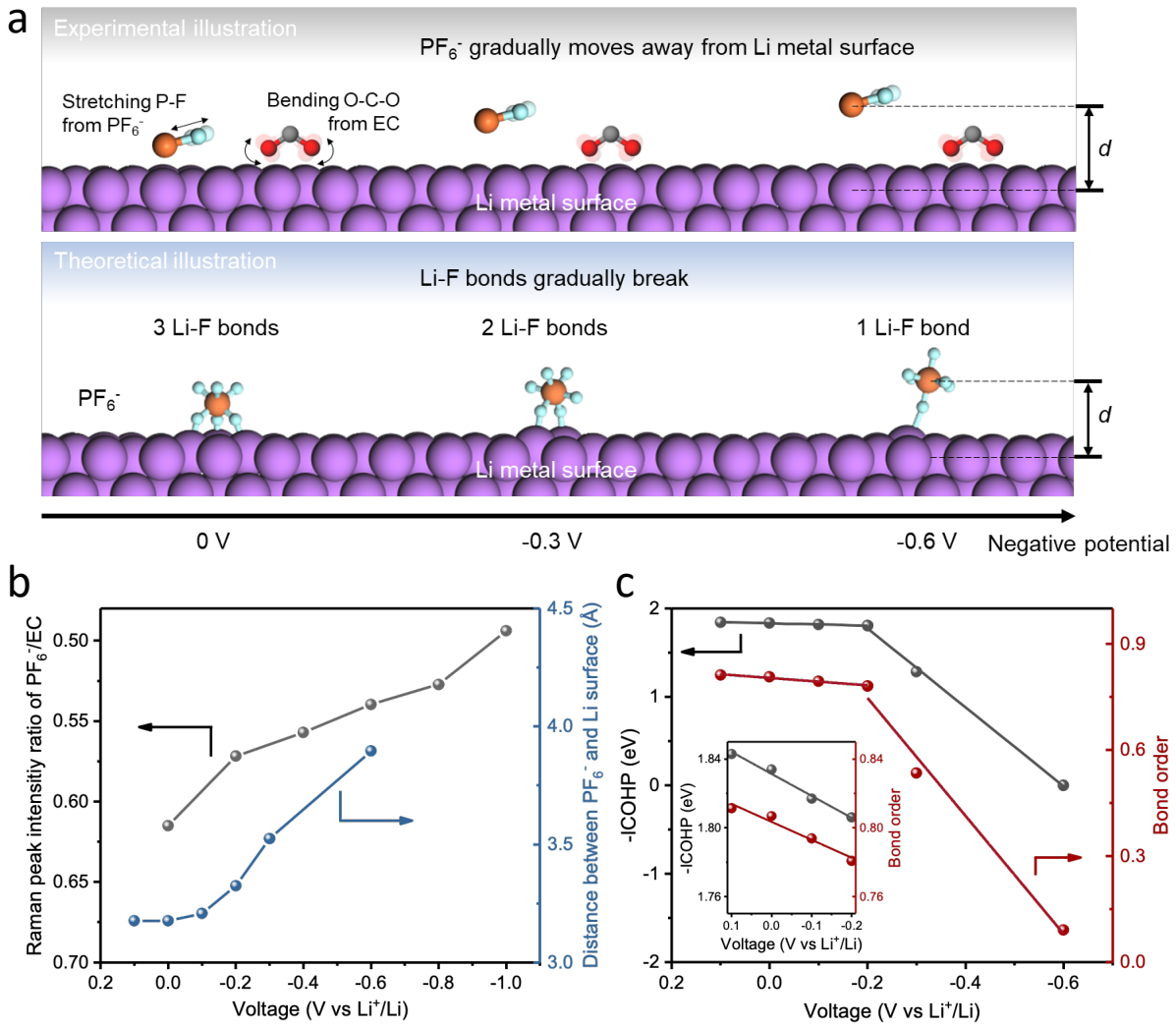

Fig. 3.5 Experimental and theoretical analysis showing anion's decay with negative voltage in 1 M $LiPF_6$ in EC/DEC. a, Experimental illustration (top) showing stretching P-F from PF_6^- decays with the negative potential from *in situ* Raman spectra and theoretical illustration (bottom) of the interaction between PF_6^- and the Li surface as a function of the potential vs. Li^+/Li. **b**, The variation trend of the absolute peak intensity of PF_6^- over EC (left) with respect to voltage calculated from in situ SERS and the distance between PF_6^- and Li surface (right) with respect to voltages from theoretical calculation. **c**, The cumulative ICOHP (left) and bond order (right) of Li–F bonds as the function of voltage.

When SEI films form in the same electrolyte chemistry, the clear differences observed between chemical and electrochemical SEI are likely due to the absence or presence of an external electric field. While spontaneous redox reactions and charge transfer can form a localized electric field, the range of this field is small, and its intensity is negligible (an order of magnitude lower) compared with an externally applied electric field. We propose that the electric field strongly influences EDL composition, which will directly impact which components are reduced to form the SEI film. For example, free anions in our model electrolyte system are likely repelled from the EDL interface by the negatively polarized Li metal surface during electrodeposition (Fig. 3.1a), which would result in predominantly solvent-derived SEI films formed in the presence of an electric field. We use in situ electrochemical SERS to provide experimental evidence for this explanation. Peaks observed in Raman spectra correspond to vibrational modes of specific chemical bonds. By using SERS to measure how the peak signals corresponding to the PF_6^- anion and EC solvent molecule evolve, we can determine how the EDL composition changes as a function of electrode potential. The peak at 740 cm^{-1} corresponds to the stretching P–F bond in free PF_6^- anion (i.e., outside the solvation shell) when it is dissolved in the electrolyte solvent (Fig. 3.6a). The peak at 715 cm^{-1} corresponds to the bending O–C–O bond in the EC solvent molecule (Fig. 3.6a). The ratio between the intensities of these two peaks is then a quantitative descriptor for the relative amount of anion present (Fig. 3.6b). By adding Au nanoparticles[8,23] to our current collector, we can enhance the Raman signal originating from the surface EDL and track how the relative amounts of anion and solvent molecule change as we vary the electrode potential. As the electrode surface is negatively polarized, we expect the negatively charged anions to be repelled away from the EDL and the neutral EC molecule to be largely unaffected by this Coulombic

interaction (Fig. 3.5a). Indeed, this is precisely what our in situ electrochemical SERS experiment demonstrates: as the electrode potential decreases below zero, the ratio of the PF_6^-/EC peaks decreases by almost 20% (Fig. 3.5b). This results in fewer anions being present within the EDL for decomposition and incorporation into the SEI layer and explains the observed differences between chemical and electrochemical SEI.

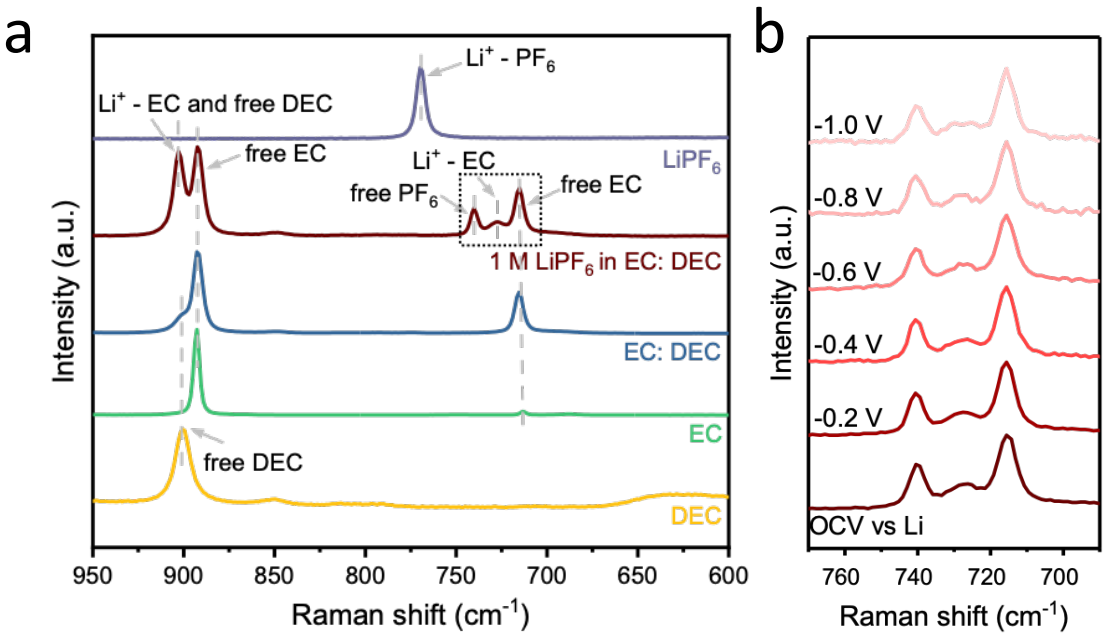

Fig. 3.6 Raman spectra showing anion's decay in 1M $LiPF_6$ in EC/DEC with negative potential. a, Raman spectra of electrolyte and individual salt or solvent included. **b**, *In situ* surface-enhanced Raman spectra of the surface layer of the working electrode under different voltages.

In addition to in situ electrochemical analysis, GCDFT calculations are performed under a constant potential based on the loop-iteration method to support the observed phenomenon (see experimental procedures). We explore the distance, adsorption strength, and Li–F bond strength at the molecular scale as a function of potential to quantify the attraction and repulsion behaviors

between PF_6^- and the Li surface. Our investigation reveals that the PF_6^- molecule chemisorbs to the Li surface through three robust F–Li bonds under positive potential, gradually transitioning to physisorption with increased separation and weakened bonds as the potential becomes negative (Fig. 3.5a and Fig. 3.7). A nearly linear relationship is shown between the applied voltage and the distance between PF_6^- and the Li surface. In other words, increasing the negative polarization of the Li surface repels and separates PF_6^- from the Li metal (Fig. 3.5b). The relationship between the relative position of PF_6^- and the Li surface has been further elucidated through a detailed analysis of the Li–F bonds. With increasing negative potentials, there is a linear decrease in both the integrated crystal orbital Hamilton populations (ICOHPs) and the bond order corresponding to the Li–F interactions, suggestive of a progressive weakening of these bonds (Fig. 3.5c). The cleavage of a single Li–F bond results in a pronounced decline in the cumulative bond strength. Notably, at a potential of −0.6 V vs. Li^+/Li, the interaction between Li and F atoms diminishes to the point of nonexistence, indicative of a repulsive interaction. To illustrate, more positive potentials favor PF_6^- adsorption, while PF_6^- desorbs from the Li surface at more negative potentials (Fig. 3.5a). While it is qualitatively expected that negative potentials would repel anions like PF_6^-, our calculations here provide a quantitative explanation for how the PF_6^- adsorption behavior is modulated by the applied potential and show how the transition between adsorbed and non-adsorbed anions occurs. The molecular-level changes observed through computational analysis align consistently with our experimental findings obtained from in situ SERS.

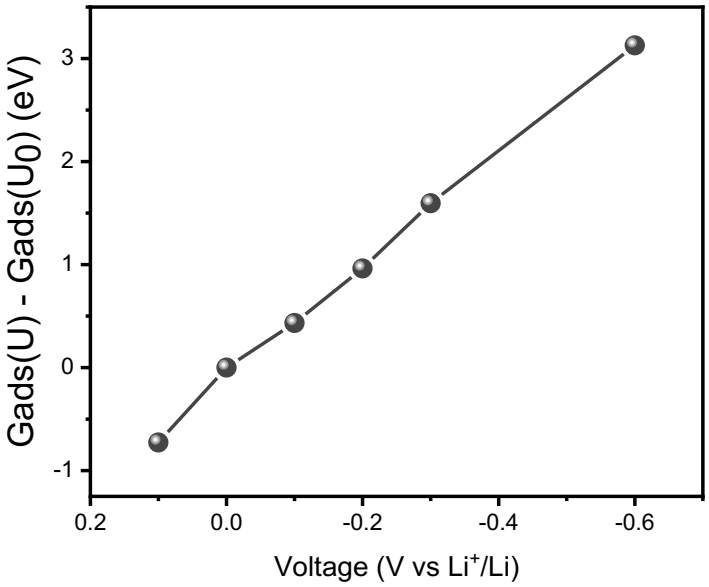

Fig. 3.7 The adsorption energy between the center of PF_6^- anion and the top surface of Li at different applied voltages.

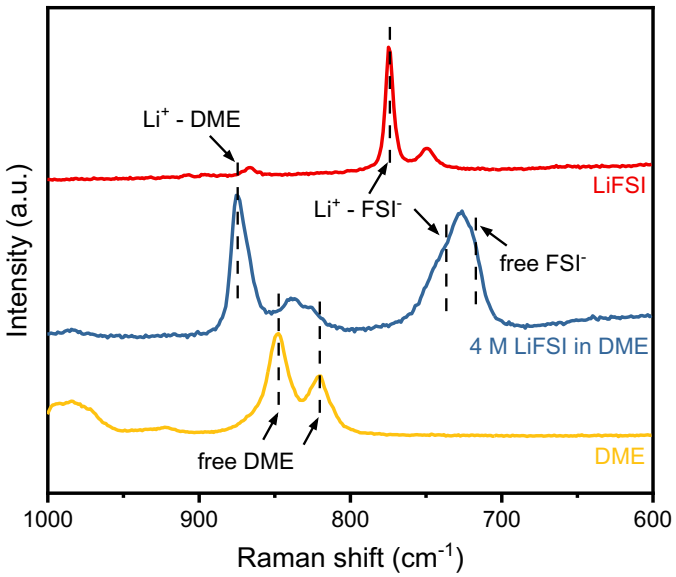

Fig. 3.8 Raman spectra of 4M LiFSI in DME and individual salt or solvent included.

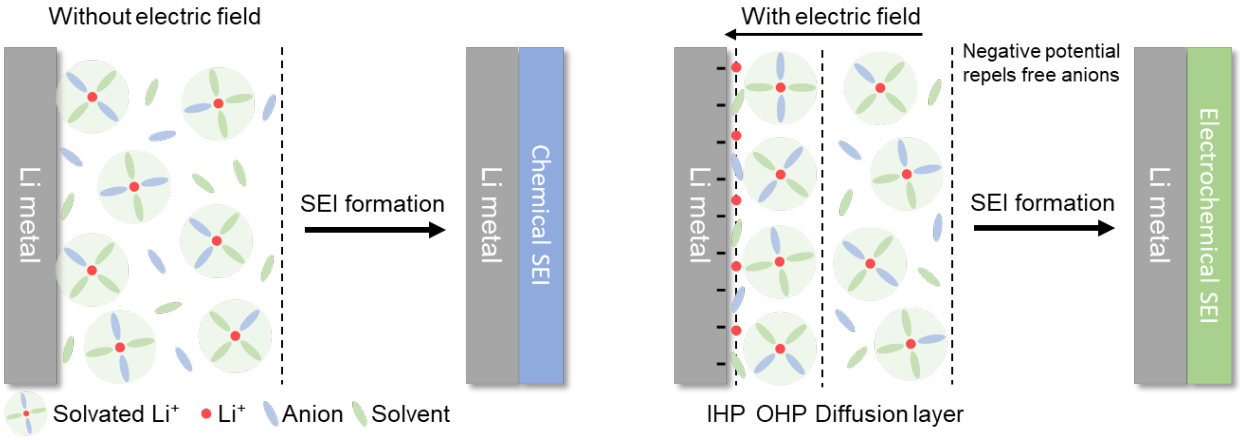

Fig. 3.9 Scheme of chemical and electrochemical SEI formation processes in 4M LiFSI in DME. In the absence of an electric field, solvated Li^+, free anions and solvents are stochastic distributed (left). With applied electric field, inner Helmholtz plane (IHP) consists of desolvated Li^+, anions and solvents, while outer Helmholtz plane (OHP) is occupied by Li solvation structures, with free, unsolvated anions being repelled from the Helmholtz layer.

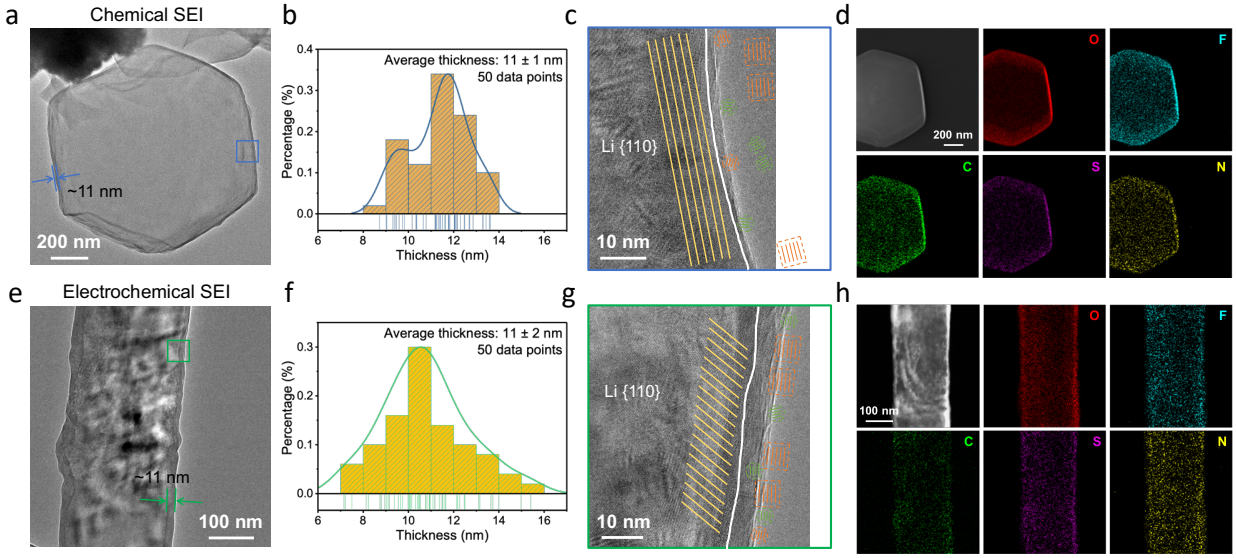

Fig. 3.10 Cryo-EM analysis on structure and chemistry of chemical and electrochemical SEI in 4 M LiFSI in DME. a, Cryo-EM image of faceted Li particle covered with a layer of chemical

SEI. **b**, Thickness statistics of chemical SEI. **c**, High-resolution cryo-EM image of chemical SEI layer, magnified from the blue box in (**a**). d, STEM EDS mapping of chemical SEI. **e–h**, Analogous images to (**a–d**) but collected on electrochemical SEI.

Our findings reveal that the presence or absence of an electric field can influence the composition of the EDL by Coulombic interactions with free anions, thus changing the structure and chemistry of the resulting SEI film. Since the electric field strength can vary dramatically across any electrode surface that is not atomically uniform,[37,38] our results may explain the spatial non-uniformity observed in SEI films formed in electrolytes with many free anions. Specifically, the local concentration of anions within the EDL across the electrode surface may vary substantially due to changes in the local electric field,[8,9] thus causing non-uniformity in the SEI structure and chemistry. For electrolyte chemistries that don't have as many free anions responding to the electric field (e.g., highly concentrated electrolytes), we would expect this spatial variation in electric field to have less of an impact on the resulting SEI film uniformity. In other words, there should not be much distinction between the chemical and electrochemical SEI formed in electrolytes with more anions in the solvation structure. Experimental observations of the chemical and electrochemical SEI films formed in a highly concentrated electrolyte support this conclusion. Due to increased viscosity and insolubility of concentrated $LiPF_6$ (less than 3M) in EC/DEC, we chose 4M Li bis(fluorosulfonyl)imide (LiFSI) in dimethoxyethane (DME)[39,40] as the representative of a highly concentrated electrolyte system with a Li^+ solvation structure containing a larger amount of anions (Fig. 3.8) than conventional electrolytes such as 1 M $LiPF_6$ in EC/DEC. Because this electrolyte has fewer free anions that can respond to an electric field (Fig. 3.9), the chemical and electrochemical SEI formed in 4M LiFSI in DME are observed to be similar. Our cryo-EM images

confirm that chemical and electrochemical SEI in 4M LiFSI in DME have similar thickness (~11 nm, Fig. 3.10a-b, e-f) and nanostructure with abundant dispersed Li_2O and LiF within an amorphous matrix (Fig. 3.10c,g, Fig. 3.11, and Fig. 3.12). Furthermore, STEM EDS show that the distribution of O, F, C, S, and N within the chemical and electrochemical SEI is similarly uniform (Fig. 3.10d,h). Whereas the F/C ratios of chemical and electrochemical SEI differ by more than a factor of three in 1 M $LiPF_6$ in EC/DEC, the chemical and electrochemical SEI formed in 4M LiFSI in DME have similar F/C ratio (Table 3.2). As a result, the SEI films formed in 4M LiFSI are less susceptible to changes in electric field and thus have more uniform structure and composition, leading to enhanced battery performance.[39]

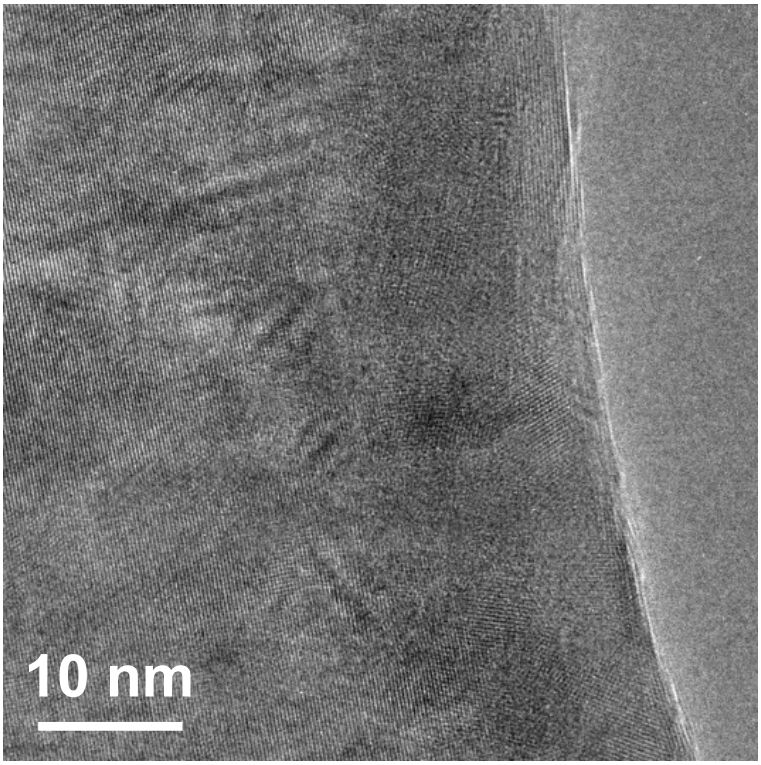

Fig. 3.11 High-resolution cryo-EM image of chemical SEI. Raw cryo-EM image of the chemical SEI formed in 4M LiFSI in DME from Fig. 3.10c in the main text.

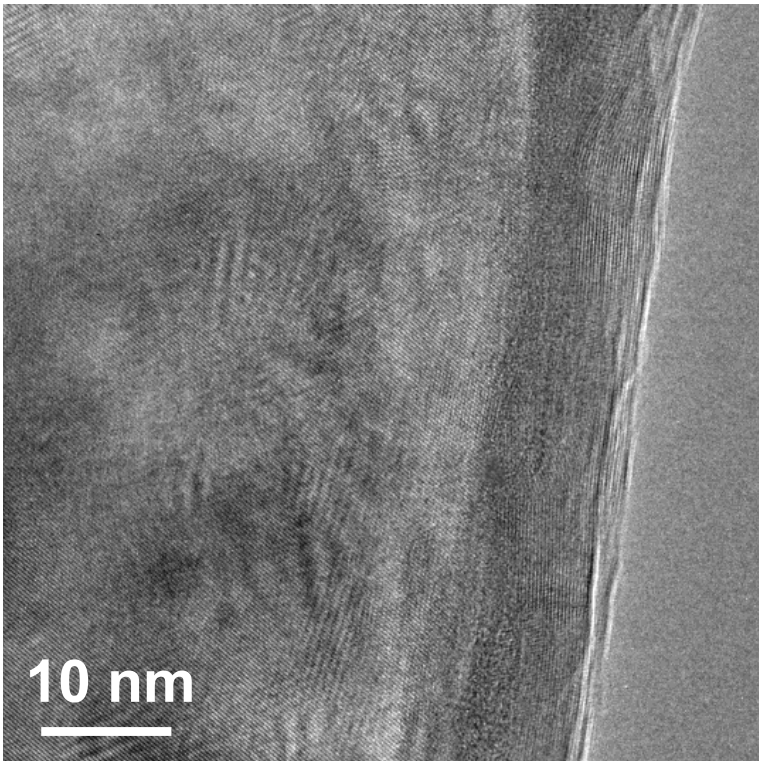

Fig. 3.12 High-resolution cryo-EM image of electrochemical SEI. Raw cryo-EM image of the chemical SEI formed in 4M LiFSI in DME from Fig. 3.10g in the main text.

Table 3.2 STEM EDS elemental analysis of chemical and electrochemical SEI in 4M LiFSI in DME.

SEI type	O ratio (atom %)	C ratio (atom %)	F ratio (atom %)	S ratio (atom %)	N ratio (atom %)	F/C
Chemical SEI	72.7±2.1	13.1±2.0	7.2±0.5	4.2±0.8	3.0±0.5	0.6±0.1
Electrochemical SEI	76.5±2.8	10.9±1.9	6.7±1.4	3.3±0.5	2.7±0.4	0.6±0.1

*Each result contains more than three data points.

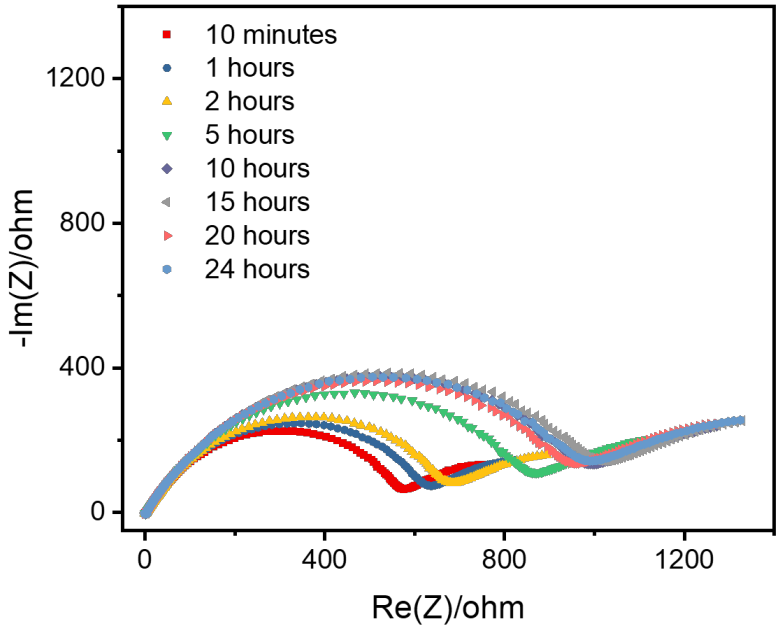

Fig. 3.13 Electrochemical impedance spectroscopy (EIS) of the Li-Li symmetric cell with different resting times. EIS results stabilized after 10 hours, indicating that the stabilization for chemical SEI structure and Li||SEI||electrolyte interfaces need at least 10 hours.

When formed in the absence of an electric field, the chemical SEI is found to be rich in anion components even in conventional electrolytes like 1 M $LiPF_6$ in EC/DEC, which is normally solvent-derived. This has important implications for battery performance since anion-enhanced SEI chemistries are typically associated with strong passivating properties that prevent continued SEI growth. To demonstrate the enhancement that chemical SEI provides for battery cycling and calendar aging, we build Li||lithium iron phosphate (LFP) cells using (1) pristine Li foil and (2) Li foil immersed in liquid electrolyte for 24 h to form a more developed chemical SEI (Fig. 3.13). With the chemical SEI, Li||LFP cells exhibit much lower voltage hysteresis between charging and discharging voltage plateaus (~100 mV, Fig. 3.14a,b) than cells without chemical SEI (~250 mV,

Fig. 3.14c,d). This suggests that the chemical SEI has high ionic conductivity and does not contribute excess impedance compared with even pristine Li foil. Thus, we observe higher capacity and CE for the chemical SEI coin cells in the early cycles, minimizing excess SEI formation (Fig. 3.14e). Furthermore, we show that the capacity loss due to 24-h calendar aging is substantially reduced in chemical SEI coin cells, with less than half as much loss compared with coin cells without chemical SEI (Fig. 3.14f). Our cryo-EM experiments show that the chemical SEI is much more passivating during calendar aging, with the SEI thickness increasing slightly (~5 nm) during 24-h rest at open circuit voltage (Fig. 3.14g,h, and Fig. 3.15a). By contrast, the electrochemical SEI does not offer as much passivation, growing nearly 40 to 80 nm non-uniformly across the Li dendrite after 24-h calendar aging (Fig. 3.14i,j, and Fig. 3.15b).

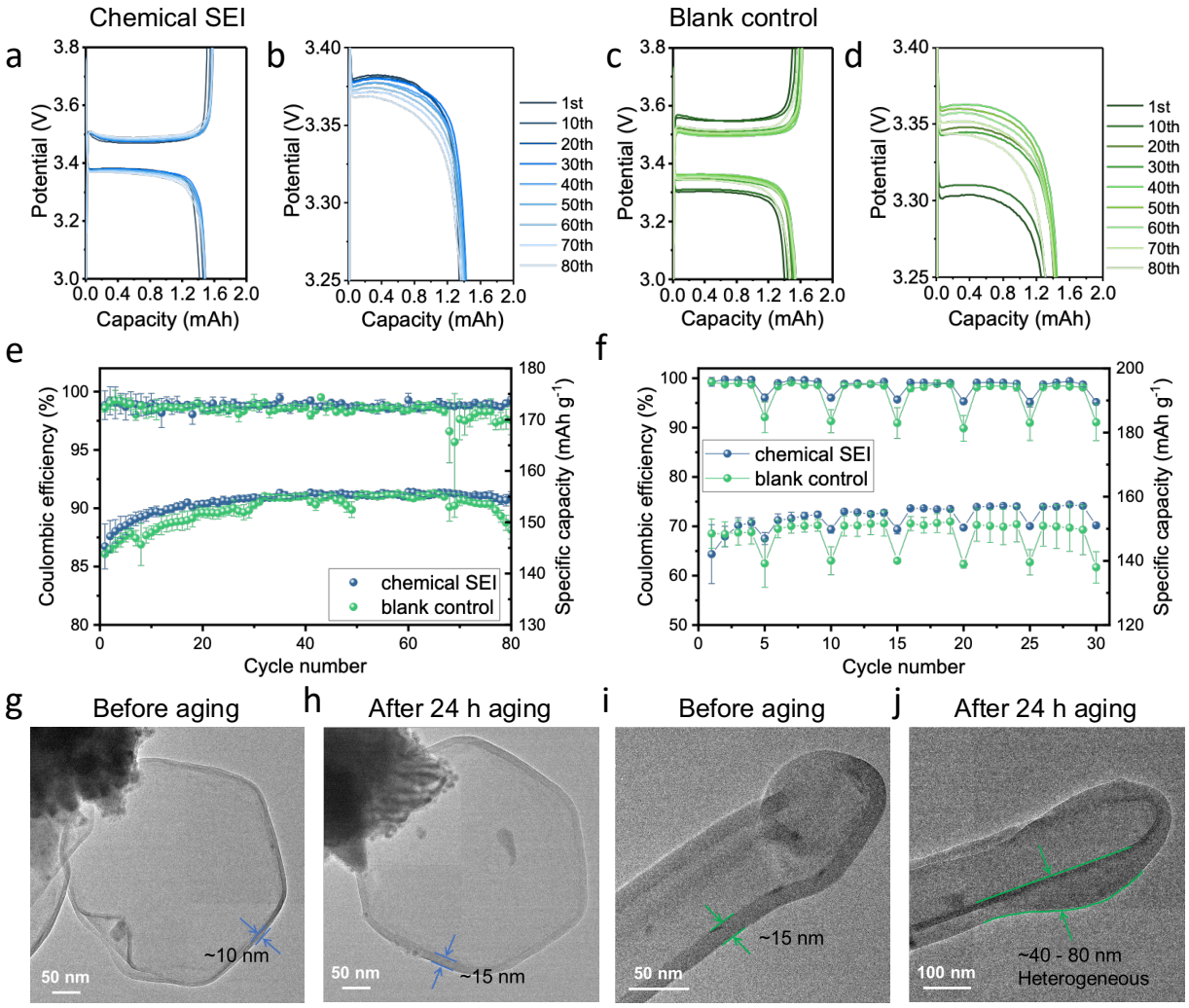

Fig. 3.14 Effect of chemical SEI on electrochemical performance in Li||LFP cells in 1 M $LiPF_6$ in EC/DEC. a, Representative voltage profiles of each ten cycles with zoomed-in view in (**b**). **c**, Representative voltage profiles of each ten cycles with calendar aging during every five cycles with zoomed-in view in (**d**). **e**, CE and specific capacity as a function of cycle number at 0.5 C. **f**, CE and specific capacity with calendar aging during every five cycles. Cryo-EM images of faceted Li particles in (**g**) and after 24-h calendar aging in (**h**). Cryo-EM images of dendritic Li particles in (**i**) and after 24-h calendar aging in (**j**).

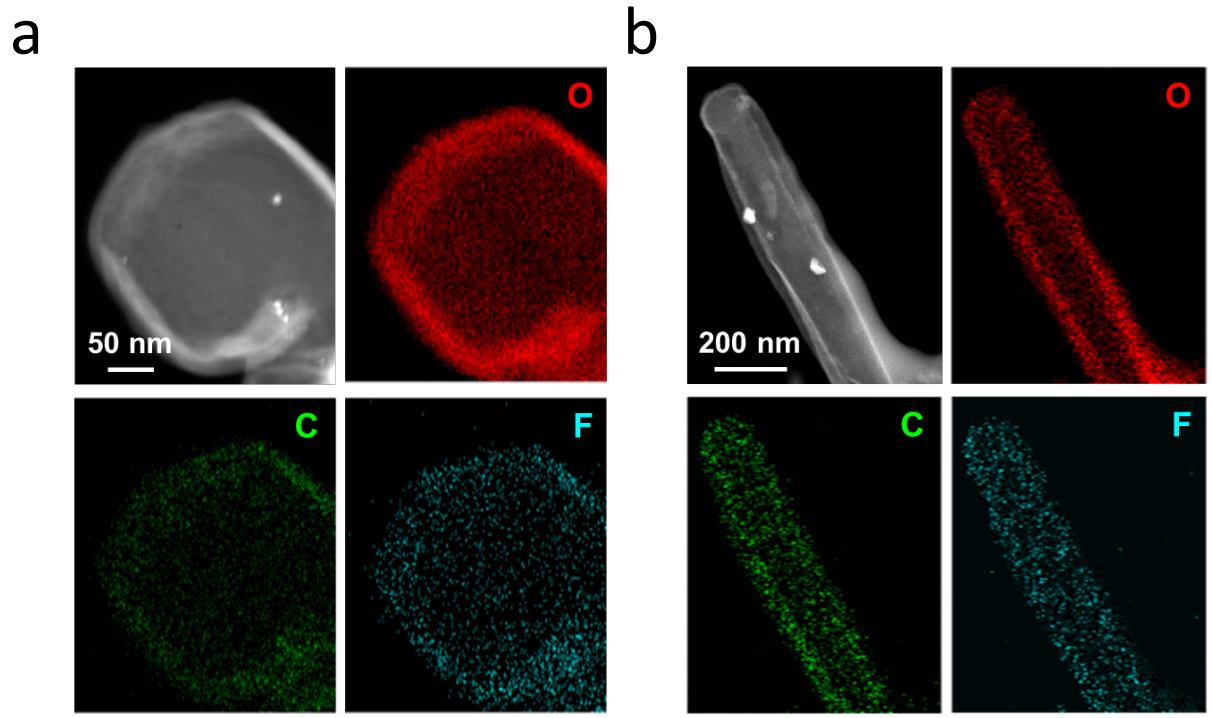

Fig. 3.15 STEM EDS mapping of chemical and electrochemical SEI after 24 hour calendar aging. a, Chemical SEI. **b**, Electrochemical SEI.

In addition to resting and growing chemical SEI before battery cycling, we also suggest periodically adding a rest period where the electric field is removed, allowing anion enrichment in the EDL for chemical SEI formation (anion-enhanced). We use a pulse-current deposition approach in the electrolyte of 1 M $LiPF_6$ in EC/DEC at a current density of 1 mA cm^{-2}, with repeated deposition for 1 s and resting for 3 s, until a capacity of 1 mAh cm^{-2} is reached. Subsequently, the stripping current density is 1 mA cm^{-2} with a cutoff voltage of 1 V. As a control experiment, standard galvanostatic cycling (i.e., no rest period) is performed at a constant current density of 1 mA cm^{-2} for the same capacity. The SEI formed during pulse-current deposition (i.e., "pulse SEI") exhibits the properties intermediate between chemical SEI and electrochemical SEI, including SEI thickness (e.g., pulse SEI thickness is around 13 nm in Fig. 3.16a,b compared with

10 nm for chemical SEI and 15 nm for electrochemical SEI), chemical components (e.g., pulse SEI contains LiF in Fig. 3.16c, while chemical SEI contains LiF and electrochemical SEI has no LiF particles in cryo-EM images), and elemental ratios (F/C ratio in pulse SEI is around 0.15, compared with around 0.3 in chemical SEI and around 0.1 in electrochemical SEI, Fig. 3.16d,e; Table 3.1). The formation of pulse SEI facilitates a more uniform and dense Li growth (Fig. 3.17), leading to increased reversibility of Li stripping. Thus, we observe a 4% CE increase (Fig. 3.16f) for the pulse-current protocol in the Li-Cu coin cell geometry. These results show that the passivating properties of the chemical SEI can positively impact battery performance and motivate the future design of optimal protocols leveraging the electric field to form more ideal SEI films.

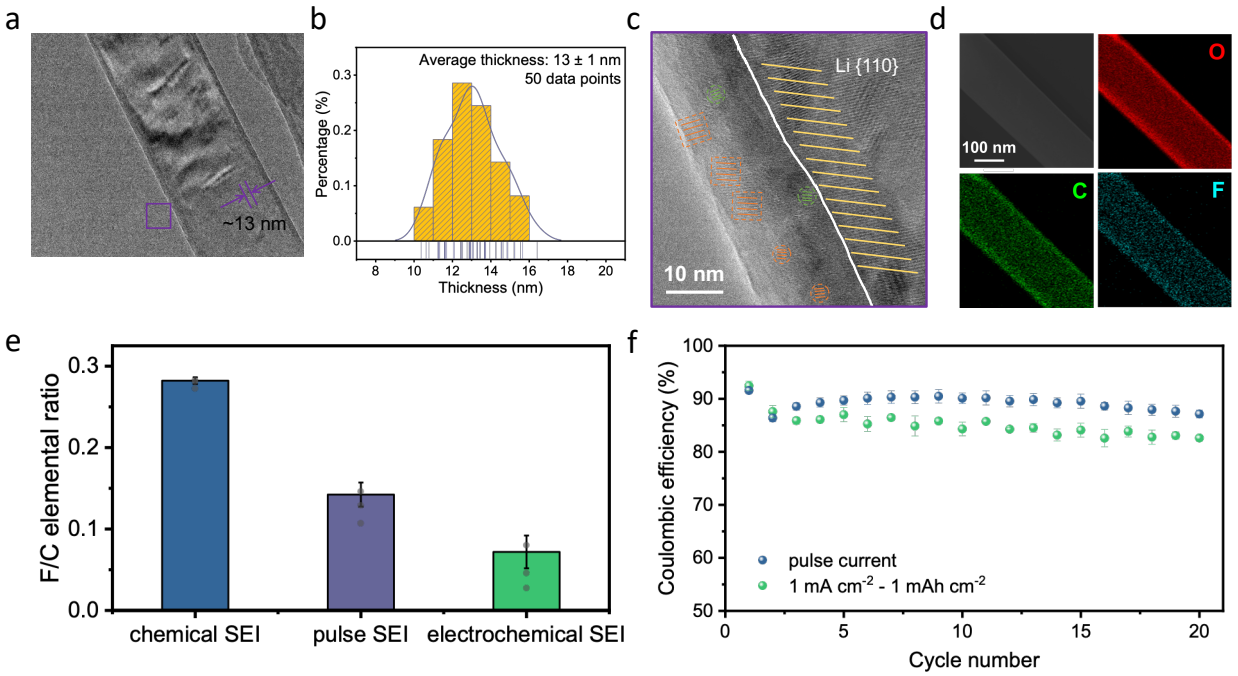

Fig. 3.16 Structural and chemical analysis of pulse SEI in 1 M $LiPF_6$ in EC/DEC. a, Cryo-EM image of Li dendrite covered with a layer of pulse SEI. **b**, Thickness statistics of pulse SEI. **c**, High-resolution cryo-EM image of pulse SEI layer, magnified from the purple box in (**a**). **d**, STEM

EDS mapping of pulse SEI. **e**, F/C elemental ratio of pulse SEI compared with chemical and electrochemical SEI calculated from XPS analysis. **f**, CE comparison between pulse current protocol (at a current density of 1 mA cm^{-2}, with repeated deposition for 1 s and resting for 3 s, until a capacity of 1 mAh cm^{-2} is reached) and standard galvanostatic cycling protocol (at a current density of 1 mA cm^{-2}, until a capacity of 1 mAh cm^{-2} is reached)**.**

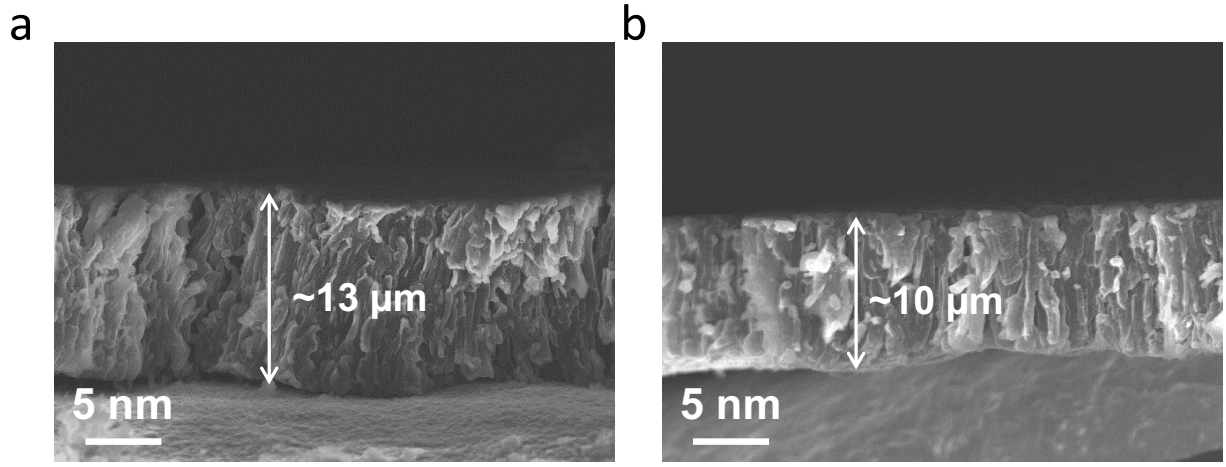

Fig. 3.17 SEM images showing cross-sectional view of Li deposition with different deposition protocols. a, Standard galvanostatic deposition at a current density of 1 mA cm^{-2}, until a capacity of 1 mAh cm^{-2} is reached. b, Pulse current protocol at a current density of 1 mA cm^{-2}, with repeated deposition for 1 s and resting for 3 s, until a capacity of 1 mAh cm^{-2} is reached.

3.4 Conclusion

Our work reveals that the SEI structure and chemistry are strongly influenced by the EDL composition, which can be tuned by the electric field. At negative surface potentials forming an electric field, we show that the electrochemical SEI exhibits solvent-derived components. Without the electric field present, the chemical SEI is more anion rich due to a larger concentration of free

anions within the EDL. The impact of the electric field on the EDL composition is shown experimentally using in situ electrochemical Raman and theoretically using GCDFT. These findings lead to new insights for battery research: (1) that spatial variation in the electric field will lead to SEI non-uniformity and (2) that SEI films normally exhibiting solvent-derived compositions can be engineered to anion-enhanced chemistries to improve battery cycling and corrosion resistance. More broadly, our results will encourage future approaches to tune the EDL composition that can enable closer control over SEI structure and composition.

3.5 Method

Preparation of electrolyte solutions

$LiPF_6$ solution in EC and DEC (1M $LiPF_6$ in EC/DEC) was directly purchased from Sigma-Aldrich with battery grade. LiFSI (Canrd, 99.5%) were dried at 65 °C overnight prior to use. DME (Sigma-Aldrich, 99.5%) was added to obtain 4M solution of LiFSI (4M LiFSI in DME). All chemicals were used as received without further purification. All electrolytes were made and stored in the Ar-filled glovebox (O_2 < 0.2 ppm, H_2O < 0.02 ppm).

Electrochemical experiments

In Li||LFP 2032-type coin cells, LFP foil (mass percent of active material is around 88%, area mass loading of active material on current collector is around 12 mg cm^{-2}, Canrd) of 10 mm in diameter was served as working electrode, and Li foil (70 μm thick, Canrd) of 15 mm in diameter was served as the counter/reference electrode. Li foil was mechanically sheared using a polyethylene scraper to remove the surface oxide and improve electrical connection to the stainless-steel coin cell case. After mechanically shearing, the clean, pristine Li foil was used to make coin cells with the below

procedures in the blank control sample. Li foil along with a chemical SEI was obtained by immersing Li foil in 1 M $LiPF_6$ in EC/DEC for 24 h.

In Li||Cu 2032-type coin cells, Cu foil (10 μm thick, Canrd, 99%) of 12 mm in diameter served as the working electrode, while Li foil of 10 mm in diameter served as the counter/reference electrode. Similar with Li||LFP cell, Li foil was mechanically sheared for processing prior using. Cu foil was rinsed with ultrapure water and acetone to remove surface contaminants before transferring into the glove box.

60 μL electrolyte was added to each cell using a 25 μm thick polypropylene-polyethylene-polypropylene separator (Celgard 2325) to divide the two electrodes. Coin cells were loaded onto a battery tester (Land Instruments) and cycled.

All battery assembly experiments were performed in the Ar-filled glovebox.

XPS sample preparation and characterization

XPS sample of electrochemical SEI was obtained by running Li||Cu 2032-type coin cells, and a 300-mesh bare Cu TEM grid (Ted Pella) was incorporated onto Cu foil, which served as the working electrodes. Electrochemical SEI together with metallic Li were deposited on the TEM grid at a normal current density of 1 mA cm^{-2} for 10 min. During this process, the SEI grows concurrently with Li dendrites, indicating that this SEI is formed through the electrolyte decomposition under the influence of an electric field. After disassembling the coin cell in an Ar-filled glovebox, TEM grid was carefully raised with a few drops of anhydrous dioxolane. For the

pulse SEI sample, the battery assembly was the same as that for the electrochemical SEI sample. The only difference is the addition of a 3 s pause for every 1 s of applying a current density of 1 mA cm^{-2}, with the total operation time maintained at 10 min. For the chemical SEI sample, after Li foil of 3 mm in diameter was mechanically sheared, it was immersed in 1 M $LiPF_6$ in EC/DEC for 10 min to grow chemical SEI and carefully raised with a few drops of anhydrous dioxolane. Once dry, SEI samples were placed onto the XPS stage and then transferred to the XPS (Kratos AXIS Ultra DLD spectrometer) chamber using an air-tight transfer holder.

Cryo-EM sample preparation and imaging

Cryo-EM samples were obtained from Li||Cu coin cells. Their assembly was the same as Li||LFP cells, except that Cu foil of 12 mm diameter stacked together with a customized TEM grid served as the working electrodes. To grow chemical SEI on Li particles for convenient imaging through cryo-EM, we apply an ultrafast current density of 200 mA cm^{-2} to deposit faceted Li particles, effectively outpacing the SEI formation.[26,41] Subsequently, when the current ceased and the electric field is absent, chemical SEI is formed on the surface of the faceted Li particle due to physical contact with the electrolyte. To realize ultrafast current density, we used Cu chunk-based TEM grids as local ultramicroelectrodes prepared in the same way as our previous publication.[26] For a fair comparison, the combined duration of electrodeposition and standing time is 10 min for chemical SEI, consistent with the preparation time for the electrochemical SEI samples. The preparation process of electrochemical SEI and pulse SEI in cryo-EM is identical to that of the XPS sample described above.

After assembling the coin cell in an Ar-filled glovebox, TEM grid was carefully rinsed with a few drops of anhydrous dioxolane. Once dry, the TEM grid with deposited Li was placed in an Eppendorf tube sealed with parafilm and transferred out of glovebox. The pressure in the glovebox, and thus the sealed tube, was greater than ambient pressure, which prevented air from leaking into the tube. Outside the glovebox, pincer pliers held the sealed Eppendorf tube and plunged quickly into a bath of liquid nitrogen, then quickly crushed open the tube after 3 s while still immersed in the liquid nitrogen to expose the grid with deposited Li to cryogen immediately. The grid was stored in a cryo-grid box in liquid nitrogen dewar for usage.

To proceed with cryo-EM imaging, the TEM grid was mounted onto a Gatan 626 TEM cryo-transfer holder using a cryo-transfer station to make sure the whole process took place under liquid nitrogen. The built-in shutter on the transfer holder was kept closed to prevent air exposure and ice condensation onto the sample when inserting the holder into the TEM column. A liquid nitrogen dewar attached to the holder maintained the grid at cryogenic temperature during the whole imaging process. All cryo-EM characterizations were carried out using an FEI Titan 80-300 scanning transmission electron microscope operated at 300 kV with a Gatan Ultrascan camera. During cryo-EM images acquisition, the corresponding electron dose flux was also recorded. Electron dose rate (flux) is less than 100 e $Å^{-2}$ s^{-1} for low-magnification cryo-EM images and less than 1,000 e $Å^{-2}$ s^{-1} for high-resolution cryo-EM images. The electron beam exposure time of each image is no more than 30 s, and the acquisition time is 0.4–1 s.

In situ surface-enhanced Raman experiments

A sealed three-electrode electrochemical Raman cell (Gaoss Union) was used to perform in situ surface-enhanced Raman experiments. A layer of coarse Au nanoparticles with a thickness of 20 nm was evaporated on the Cu mesh to serve as the working electrode for a surface enhancement effect, and Li foil served as the counter/reference electrode. The electrochemical potentiostat (BioLogic VMP3) was used to apply voltage on the Raman cell from open circuit voltage to −1 V vs. Li^+/Li, and Raman scanning was carried out in the meantime. The Raman system (Renishaw) used in this experiment was equipped with a 785 nm diode laser.

Calculational setup

DFT calculations are performed using the Vienna Ab-Initio Simulation Package (VASP) with the Perdew-Burke-Ernzerhof functional,[42] and van der Waals interactions between atoms are corrected by using D3.[43] The core electrons are described with the projector augmented wave (PAW) method.[44] The convergence criteria for electronic and force minimization are set to 10^{-6} eV and 0.02 eV/Å for structure optimization. The cutoff energy for the kinetic energy of the plane wave is 450 eV. (4 × 4)-4 layer (110) surface is chosen for modeling Li, where the Brillouin zone is sampled using the (4 × 4 × 1) gamma-centered k-point grid.

GCDFT is performed to obtain the potential-dependent energetics, where the number of electrons is allowed to change to adapt the change of work function along the reaction pathway. The potential-dependent grand canonical free energy can be expressed by a surface charging model:

$$\Omega(U) = \Omega(U) - q(U) \cdot FU = \Omega(U_0) - \frac{1}{2}C(U - U_0)^2$$

where $\Omega(U)$ is the electronic energy of the surface at the U potential in standard hydrogen electrode (SHE) scale, $q(U)$ is the charge difference against the neutral condition, and F is the

Faradaic constant. C stands for the effective capacitance and U_0 represents the potential of zero charge (pzc). For more details of GCDFT, see our previous work.[45,46,47] The self-consistent implicit solvation model VASPsol is used to represent the polarizable electrolyte region. The dielectric constant 45.9 and the Debye screening length 2.33 Å are used, as they correspond to the experimental electrolyte. We use a cutoff charge of 0.0002 to avoid unphysical invasion of the implicit solvent invasion into the Li layers.[48] The COHP analysis was performed using the LOBSTER program with the pbeVaspFit2015 basis set.[49]

An iterative method is used to achieve structural optimization under constant potential rather than constant charge.

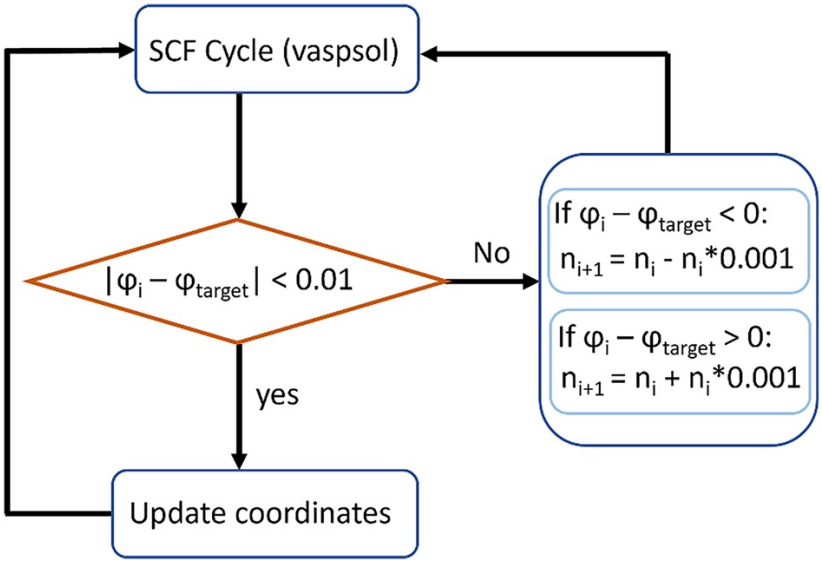

3.6 References

1 Liu, B., Zhang, J.-G. and Xu, W. Advancing Lithium Metal Batteries. *Joule* **2**, 833-845 (2018).

2 Liu, B., Zhang, Y., Pan, G., Ai, C., Deng, S., Liu, S., Liu, Q., Wang, X., Xia, X. and Tu, J. Ordered lithiophilic sites to regulate Li plating/stripping behavior for superior lithium metal anodes. *J. Mater. Chem. A* **7**, 21794-21801 (2019).

3 Lin, D., Liu, Y. and Cui, Y. Reviving the lithium metal anode for high-energy batteries. *Nat. Nanotechnol.* **12**, 194-206 (2017).

4 Wu, H., Jia, H., Wang, C., Zhang, J. G. and Xu, W. Recent Progress in Understanding Solid Electrolyte Interphase on Lithium Metal Anodes. *Adv. Energy Mater.* **11**, 2003092 (2020).

5 Liu, B., Zhang, Y., Wang, Z., Ai, C., Liu, S., Liu, P., Zhong, Y., Lin, S., Deng, S., Liu, Q. et al. Coupling a Sponge Metal Fibers Skeleton with In Situ Surface Engineering to Achieve Advanced Electrodes for Flexible Lithium-Sulfur Batteries. *Adv. Mater.* **32**, e2003657 (2020).

6 Zhao, Q., Stalin, S. and Archer, L. A. Stabilizing metal battery anodes through the design of solid electrolyte interphases. *Joule* **5**, 1119-1142 (2021).

7 Xu, Y., Jia, H., Gao, P., Galvez-Aranda, D. E., Beltran, S. P., Cao, X., Le, P. M. L., Liu, J., Engelhard, M. H., Li, S. et al. Direct in situ measurements of electrical properties of solid–electrolyte interphase on lithium metal anodes. *Nat. Energy* **8**, 1345–1354 (2023).

8 Zhang, W., Lu, Y., Wan, L., Zhou, P., Xia, Y., Yan, S., Chen, X., Zhou, H., Dong, H. and Liu, K. Engineering a passivating electric double layer for high performance lithium metal batteries. *Nat. Commun.* **13**, 2029 (2022).

9 Yan, C., Li, H. R., Chen, X., Zhang, X. Q., Cheng, X. B., Xu, R., Huang, J. Q. and Zhang, Q. Regulating the Inner Helmholtz Plane for Stable Solid Electrolyte Interphase on Lithium Metal Anodes. *J. Am. Chem. Soc.* **141**, 9422-9429 (2019).

10 Xu, R., Shen, X., Ma, X. X., Yan, C., Zhang, X. Q., Chen, X., Ding, J. F. and Huang, J. Q. Identifying the Critical Anion-Cation Coordination to Regulate the Electric Double Layer for an Efficient Lithium-Metal Anode Interface. *Angew. Chem. Int. Ed.* **60**, 4215-4220 (2021).

11 Wu, Q., McDowell, M. T. and Qi, Y. Effect of the Electric Double Layer (EDL) in Multicomponent Electrolyte Reduction and Solid Electrolyte Interphase (SEI) Formation in Lithium Batteries. *J. Am. Chem. Soc.* **145**, 2473-2484 (2023).

12 Wang, H., Yu, Z., Kong, X., Kim, S. C., Boyle, D. T., Qin, J., Bao, Z. and Cui, Y. Liquid electrolyte: The nexus of practical lithium metal batteries. *Joule* **6**, 588-616 (2022).

13 Ren, X., Gao, P., Zou, L., Jiao, S., Cao, X., Zhang, X., Jia, H., Engelhard, M. H., Matthews, B. E., Wu, H. et al. Role of inner solvation sheath within salt-solvent complexes in tailoring electrode/electrolyte interphases for lithium metal batteries. *Proc. Natl. Acad. Sci. U. S. A.* **117**, 28603-28613 (2020).

14 Yu, Z., Rudnicki, P. E., Zhang, Z., Huang, Z., Celik, H., Oyakhire, S. T., Chen, Y., Kong, X., Kim, S. C., Xiao, X. et al. Rational solvent molecule tuning for high-performance lithium metal battery electrolytes. *Nat. Energy* **7**, 94-106 (2022).

15 Xu, K. Electrolytes and interphases in Li-ion batteries and beyond. *Chem. Rev.* **114**, 11503-11618 (2014).

16 Chen, J., Fan, X., Li, Q., Yang, H., Khoshi, M. R., Xu, Y., Hwang, S., Chen, L., Ji, X., Yang, C. et al. Electrolyte design for LiF-rich solid–electrolyte interfaces to enable high-performance microsized alloy anodes for batteries. *Nat. Energy* **5**, 386-397 (2020).

17 Wang, H., Huang, W., Yu, Z., Huang, W., Xu, R., Zhang, Z., Bao, Z. and Cui, Y. Efficient Lithium Metal Cycling over a Wide Range of Pressures from an Anion-Derived Solid-Electrolyte Interphase Framework. *ACS Energy Lett.* **6**, 816-825 (2021).

18 Ren, X., Chen, S., Lee, H., Mei, D., Engelhard, M. H., Burton, S. D., Zhao, W., Zheng, J., Li, Q., Ding, M. S. et al. Localized High-Concentration Sulfone Electrolytes for High-Efficiency Lithium-Metal Batteries. *Chem.* **4**, 1877-1892 (2018).

19 Cao, X., Gao, P., Ren, X., Zou, L., Engelhard, M. H., Matthews, B. E., Hu, J., Niu, C., Liu, D., Arey, B. W. et al. Effects of fluorinated solvents on electrolyte solvation structures and electrode/electrolyte interphases for lithium metal batteries. *Proc. Natl. Acad. Sci. U. S. A.* **118**, e2020357118 (2021).

20 Jiang, L., Li, D., Xie, X., Ji, D., Li, L., Li, L., He, Z., Lu, B., Liang, S. and Zhou, J. Electric double layer design for Zn-based batteries. *Energy Storage Mater.* **62**, 102932 (2023).

21 Li, D., Tang, Y., Liang, S., Lu, B., Chen, G. and Zhou, J. Self-assembled multilayers direct a buffer interphase for long-life aqueous zinc-ion batteries. *Energy Environ. Sci.* **16**, 3381-3390 (2023).

22 Daniel M. Seo, Joshua Lee Allen, Lindsay A. Gardner, Sang-Don Han, Boyle, P. D. and Henderson, W. A. Electrolyte Solvation and Ionic Association: Cyclic Carbonate and Ester-LiTFSI and -LiPF6 Mixtures. *ECS Trans.* **50**, 375-380 (2013).

23 Yang, G., Ivanov, I. N., Ruther, R. E., Sacci, R. L., Subjakova, V., Hallinan, D. T. and Nanda, J. Electrolyte Solvation Structure at Solid-Liquid Interface Probed by Nanogap Surface-Enhanced Raman Spectroscopy. *ACS Nano* **12**, 10159-10170 (2018).

24 Han, B., Zhang, Z., Zou, Y., Xu, K., Xu, G., Wang, H., Meng, H., Deng, Y., Li, J. and Gu, M. Poor Stability of Li(2) CO(3) in the Solid Electrolyte Interphase of a Lithium-Metal Anode Revealed by Cryo-Electron Microscopy. *Adv. Mater.* **33**, e2100404 (2021).

25 Gao, Y., Du, X., Hou, Z., Shen, X., Mai, Y.-W., Tarascon, J.-M. and Zhang, B. Unraveling the mechanical origin of stable solid electrolyte interphase. *Joule* **5**, 1860-1872 (2021).

26 Yuan, X., Liu, B., Mecklenburg, M. and Li, Y. Ultrafast deposition of faceted lithium polyhedra by outpacing SEI formation. *Nature* **620**, 86-91 (2023).

27 Zhang, E., Mecklenburg, M., Yuan, X., Wang, C., Liu, B. and Li, Y. Expanding the cryogenic electron microscopy toolbox to reveal diverse classes of battery solid electrolyte interphase. *iScience* **25**, 105689 (2022).

28 Liu, B., Yuan, X. and Li, Y. Colossal Capacity Loss during Calendar Aging of Zn Battery Chemistries. *ACS Energy Lett.* **8**, 3820-3828 (2023).

29 Boyle, D. T., Huang, W., Wang, H., Li, Y., Chen, H., Yu, Z., Zhang, W., Bao, Z. and Cui, Y. Corrosion of lithium metal anodes during calendar ageing and its microscopic origins. *Nat. Energy* **6**, 487–494 (2021).

30 Zhao, Y., Zhou, T., Jeurgens, L. P. H., Kong, X., Choi, J. W. and Coskun, A. Electrolyte engineering for highly inorganic solid electrolyte interphase in high-performance lithium metal batteries. *Chem.* **9**, 547-549 (2023).

31 Tan, Y. H., Lu, G. X., Zheng, J. H., Zhou, F., Chen, M., Ma, T., Lu, L. L., Song, Y. H., Guan, Y., Wang, J. et al. Lithium Fluoride in Electrolyte for Stable and Safe Lithium-Metal Batteries. *Adv. Mater.* **33**, e2102134 (2021).

32 Guo, R., Wang, D., Zuin, L. and Gallant, B. M. Reactivity and Evolution of Ionic Phases in the Lithium Solid–Electrolyte Interphase. *ACS Energy Lett.* **6**, 877-885 (2021).

33 E. Peled, D. G. a. G. A. Advanced Model for Solid Electrolyte Interphase Electrodes in Liquid and Polymer Electrolytes. *J. Electrochem. Soc.* **144**, L208 (1997).

34 Li, Y., Li, Y., Pei, A., Yan, K., Sun, Y., Wu, C.-L., Joubert, L.-M., Chin, R., Koh, A. L., Yu, Y. et al. Atomic structure of sensitive battery materials and interfaces revealed by cryo–electron microscopy. *Science* **358**, 506-510 (2017).

35 Li, Y., Huang, W., Li, Y., Pei, A., Boyle, D. T. and Cui, Y. Correlating Structure and Function of Battery Interphases at Atomic Resolution Using Cryoelectron Microscopy. *Joule* **2**, 2167-2177 (2018).

36 Aurbach, D., Ein-Ely, Y. and Zaban, A. The Surface Chemistry of Lithium Electrodes in Alkyl Carbonate Solutions. *J. Electrochem. Soc.* **141**, L1 (1994).

37 Zhang, X., Wang, A., Liu, X. and Luo, J. Dendrites in Lithium Metal Anodes: Suppression, Regulation, and Elimination. *Acc. Chem. Res.* **52**, 3223-3232 (2019).

38 Liu, M., Pang, Y., Zhang, B., De Luna, P., Voznyy, O., Xu, J., Zheng, X., Dinh, C. T., Fan, F., Cao, C. et al. Enhanced electrocatalytic CO2 reduction via field-induced reagent concentration. *Nature* **537**, 382-386 (2016).

39 Qian, J., Henderson, W. A., Xu, W., Bhattacharya, P., Engelhard, M., Borodin, O. and Zhang, J. G. High rate and stable cycling of lithium metal anode. *Nat. Commun.* **6**, 6362 (2015).

40 Holoubek, J., Liu, H., Wu, Z., Yin, Y., Xing, X., Cai, G., Yu, S., Zhou, H., Pascal, T. A., Chen, Z. et al. Tailoring Electrolyte Solvation for Li Metal Batteries Cycled at Ultra-Low Temperature. *Nat. Energy* **6**, 303-313 (2021).

41 Boyle, D. T., Kong, X., Pei, A., Rudnicki, P. E., Shi, F., Huang, W., Bao, Z., Qin, J. and Cui, Y. Transient Voltammetry with Ultramicroelectrodes Reveals the Electron Transfer Kinetics of Lithium Metal Anodes. *ACS Energy Lett.* **5**, 701-709 (2020).

42 Kresse and Furthmüller, J. Efficient iterative schemes for ab initio total-energy calculations using a plane-wave basis set. *Phys. Rev. B* **54**, 11169 (1996).

43 Grimme, S., Antony, J., Ehrlich, S. and Krieg, H. A consistent and accurate ab initio parametrization of density functional dispersion correction (DFT-D) for the 94 elements H-Pu. *J. Chem. Phys.* **132**, 154104 (2010).

44 Kresse, G., and Joubert, D. From ultrasoft pseudopotentials to the projector augmented-wave method. *Phys. Rev. B* **59**, 1758 (1999).

45 Steinmann, S. N., Michel, C., Schwiedernoch, R. and Sautet, P. Impacts of electrode potentials and solvents on the electroreduction of CO2: a comparison of theoretical approaches. *Phys. Chem. Chem. Phys.* **17**, 13949-13963 (2015).

46 Steinmann, S. N. and Sautet, P. Assessing a First-Principles Model of an Electrochemical Interface by Comparison with Experiment. *J. Phys. Chem. C* **120**, 5619-5623 (2016).

47 Steinmann, S. N., Sautet, P. and Michel, C. Solvation free energies for periodic surfaces: comparison of implicit and explicit solvation models. *Phys. Chem. Chem. Phys.* **18**, 31850-31861 (2016).

48 Peng, L., Wei, Z., Wan, C., Li, J., Chen, Z., Zhu, D., Baumann, D., Liu, H., Allen, C. S., Xu, X. et al. A fundamental look at electrocatalytic sulfur reduction reaction. *Nat. Catal.* **3**, 762-770 (2020).

49 Nelson, R., Ertural, C., George, J., Deringer, V. L., Hautier, G. and Dronskowski, R. LOBSTER: Local orbital projections, atomic charges, and chemical-bonding analysis from projector-augmented-wave-based density-functional theory. *J. Comput. Chem.* **41**, 1931-1940 (2020).

Chapter 4: Imaging of nitrogen fixation at lithium solid electrolyte interphases via cryo-electron microscopy

Adapted with permission from Steinberg, K.; Yuan, X.; Klein, C. K.; Lazouski, N.; Mecklenburg, M.; Manthiram K.; Li, Y. Imaging of nitrogen fixation at lithium solid electrolyte interphases via cryo-electron microscopy. *Nature Energy* **8**, 138-148 (2023). https://doi.org/10.1038/s41560-022-01177-5. Copyright (2023) Springer Nature.

4.1 Abstract

Lithium (Li) metal chemistry, widely studied in the context of batteries, is now emerging as a key enabler beyond energy storage, notably in electrified chemical manufacturing. One compelling example is electrochemical Li-mediated ammonia synthesis, a promising route to decarbonize the ammonia industry by replacing the energy- and carbon-intensive Haber–Bosch process. Among ambient-condition approaches, Li-mediated nitrogen reduction stands out, yet the role of metallic Li and its passivation layer (i.e., the solid electrolyte interphase, called SEI), remains poorly understood. Here, we use cryogenic transmission electron microscopy (cryo-EM) and wealth of knowledge of Li metal in batteries to investigate Li reactivity and SEI behavior in electrified ammonia synthesis. We find that the proton donor (such as ethanol) critically governs Li's reactivity toward nitrogen. In the absence of ethanol, the SEI passivates Li metal, suppressing nitrogen fixation. Ethanol disrupts this passivation, enabling continuous Li reactivity at the interface.

4.2 Introduction

Ammonia is a cornerstone molecule in the global chemical industry, valued not only for its dominant role in fertilizer production but also for its versatility as a feedstock in numerous nitrogen-containing compounds.[1-5] In the context of a transitioning energy landscape, ammonia is increasingly recognized for its potential as a carbon-free energy vector, owing to its high energy density, ease of liquefaction, and compatibility with existing distribution infrastructure. Despite its broad utility, current industrial ammonia synthesis relies almost exclusively on the Haber–Bosch process, which operates under harsh thermodynamic conditions and consumes significant fossil-derived hydrogen.[5,6] This results in substantial greenhouse gas emissions, making ammonia production responsible for a notable fraction of global carbon dioxide output.[7,8] These limitations motivated the development of alternative ammonia synthesis pathways that are more sustainable, decentralized, and compatible with intermittent renewable energy sources.[9]

Electrochemical ammonia synthesis represents a compelling route toward sustainable ammonia production.[10] It offers the potential to operate under ambient conditions, utilize water as the hydrogen source, and be powered entirely by renewable electricity. Among the various strategies under exploration, lithium (Li)-mediated electrochemical ammonia synthesis (LiMEAS) has emerged as one of the most effective strategies, owing to its high Faradaic efficiency and steady performance improvements in recent years.[11-13] In this approach, Li metal is electrochemically deposited from the electrolytes, typically containing lithium tetrafluoroborate ($LiBF_4$) or lithium perchlorate ($LiClO_4$) dissolved in tetrahydrofuran (THF) and subsequently reacts with nitrogen and a proton donor to form ammonia (Fig. 4.1).[11, 14-17] Li is widely known for its role in

rechargeable batteries, while recent developments in LiMEAS have revealed a compelling new dimension of Li metal chemistry that extends well beyond batteries.

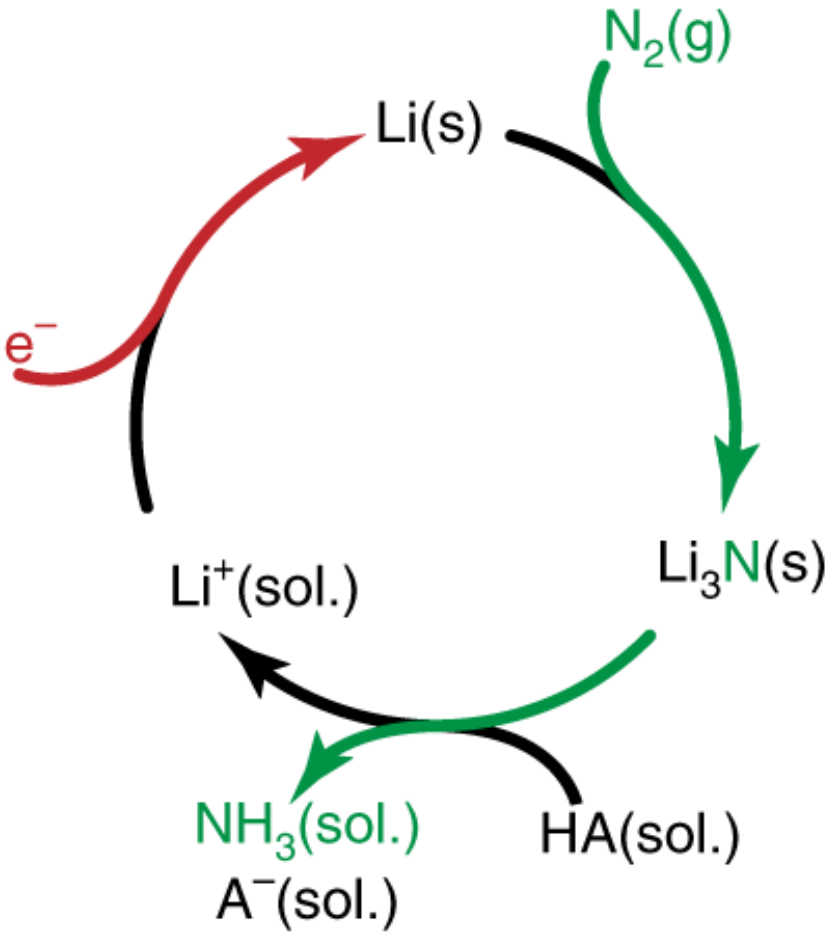

Fig. 4.1 Reaction pathways involved in a Li-mediated catalytic cycle for nitrogen reduction.[11]

Despite its promise, the mechanistic role of Li metal in LiMEAS remains a subject of active investigation due to its high reactivity. Some studies suggest that Li metal is consumed through thermochemical steps involving nitridation and protonation (Fig. 4.2a),[14-16,18] whereas others[19-20] propose an electrocatalytic mechanism in which Li or its compounds mediate nitrogen reduction without being consumed (Fig. 4.2b). Another group of theory added the discussion about the solid

electrolyte interphase (SEI), a passivation layer that forms spontaneously at the Li metal surface due to electrolyte decomposition.[21-22] The SEI governs Li-ion transport and surface reactivity, yet its precise influence on nitrogen fixation remains poorly understood. Although chemical titrations and surface characterization techniques have provided useful insights, spatially resolved probing of Li metal and the SEI under operating conditions continues to be a major challenge. The SEI is frequently invoked to explain the complex interfacial phenomena observed in LiMEAS, yet its mechanistic role remains only partially understood. The proposed explanations highlight the importance of relative transport rates of Li-ions, nitrogen, and protons through a non-reactive SEI (Fig. 4.2c-d).[19,23] In this view, mismatches in diffusion rates can lead to the accumulation of metallic Li, the formation of Li nitride, or increased hydrogen evolution, all of which reduce selectivity. This work here emphasized the influence of the proton donor's identity and concentration in regulating SEI permeability, particularly with respect to nitrogen transport across the interface. Currently, the molecular-scale mechanism of LiMEAS remains unresolved due to the inherent difficulty of characterizing Li metal and its SEI with sufficient spatial and chemical resolution under operating conditions, which continues to pose a significant experimental challenge.

In this work, we employed a multiscale approach to investigate the role of surface chemistry in LiMEAS. By integrating bulk quantification of reaction products with scanning electron microscopy (SEM), X-ray photoelectron spectroscopy (XPS), and cryogenic electron microscopy (cryo-EM), we probed Li reactivity across multiple length scales. Cryo-EM, in particular, enabled high-resolution visualization of Li and interfacial structures, building on its demonstrated utility in battery research.[24-27] Our results reveal that Li nitridation is highly sensitive to surface

passivation: in the absence of a proton donor such as ethanol, the SEI effectively inhibits the reaction between Li metal and nitrogen. Ethanol addition disrupts the formation of a fully passivating SEI, allowing for continuous surface reactivity and the sustained consumption of metallic Li during deposition. Together, these findings indicate that LiMEAS proceeds through ongoing thermochemical reactions at a partially passivated Li surface, representing a rare instance in Li electrochemistry where corrosion-like behavior across the SEI is essential for device operation.

This work is the result of close collaboration. My collaborators led the effort in designing and performing the extensive experimental studies, including quantitative analysis of reaction products and characterizations. Their careful work laid the foundation for our understanding of reactivity trends in the system. My contribution complemented these efforts by drawing on my background in Li metal chemistry and expertise in cryo-EM to characterize Li metal and its interfacial behavior during LiMEAS. In this chapter, I approach the findings from the perspective of a battery engineer and cryo-EM practitioner, focusing on how Li behaves in this new electrochemical environment and what its interfacial signatures reveal.

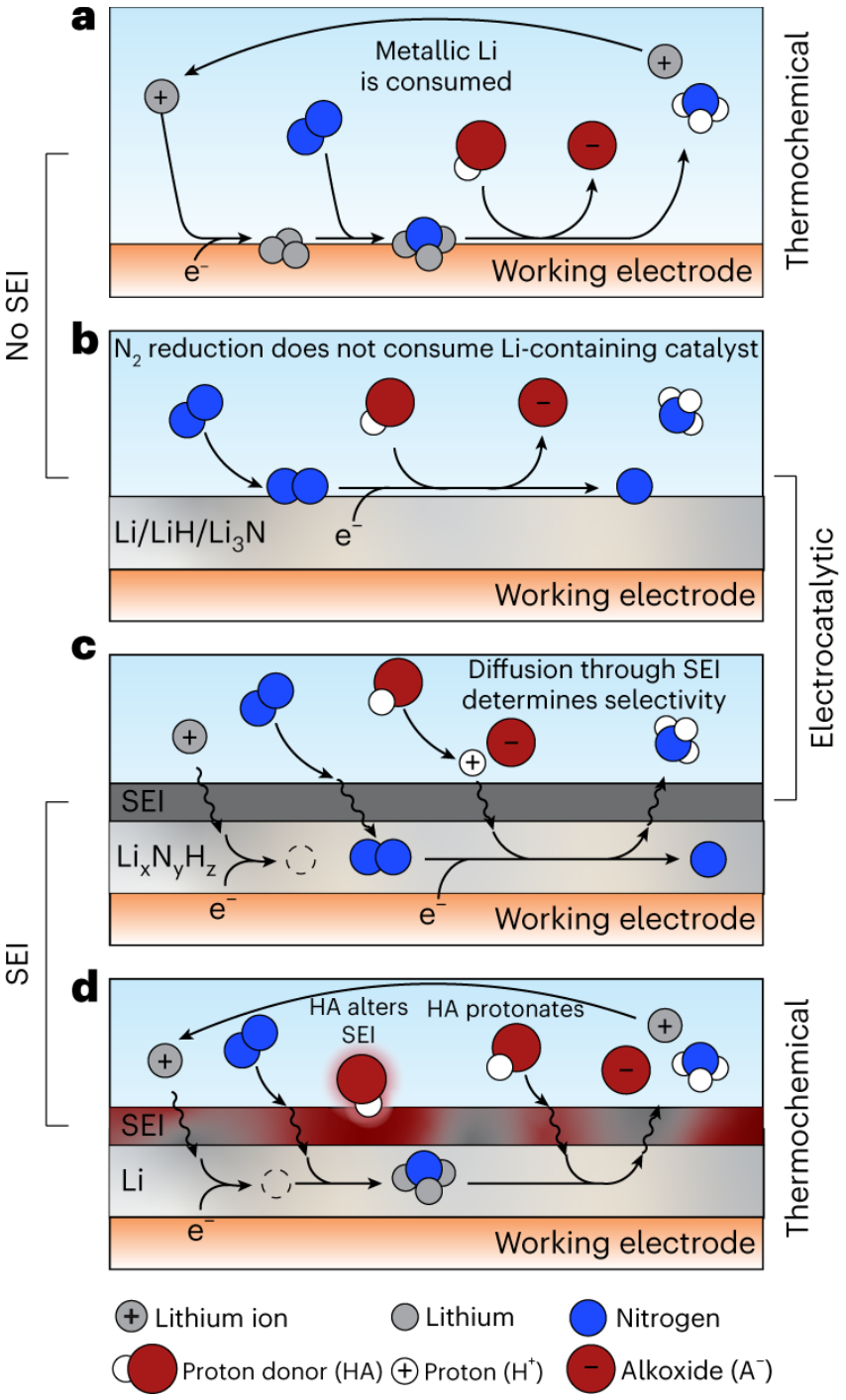

Fig. 4.2 Previously proposed reaction mechanisms of Li-mediated ammonia synthesis. a, Thermochemical mechanism.[16] **b**, Electrocatalytic mechanism.[20] **c**, SEI transport model.[19] **d**, SEI permeability model.[23]

4.3 Discussion

To systematically probe the influence of nitrogen and proton donors on Li surface reactivity in LiMEAS, we developed four well-defined model systems that varied in gas environment and the presence or absence of ethanol. These systems included: (A) argon atmosphere without a proton donor (no HA, Ar), (B) nitrogen atmosphere without a proton donor (no HA, N_2), (C) argon with 0.1M ethanol (EtOH, Ar), and (D) nitrogen with 0.1M ethanol (EtOH, N_2). The conditions were carefully chosen to facilitate surface characterization rather than to maximize electrochemical performance. Ambient pressure, low current density, and flooded electrode configurations allowed for more controlled and interpretable measurements. By independently controlling the presence of nitrogen and ethanol, we aimed to isolate their respective effects on Li's interfacial chemistry and the formation of reduced nitrogen species.

To evaluate the impact of each variable, we quantified key reaction products including ammonia, Li nitride, hydrogen gas, and residual metallic Li (Fig. 4.3). Ammonia was measured using the salicylate assay,[16,28] while Li nitride and related fixed nitrogen species were quantified through acid titration followed by the same colorimetric method (Fig. 4.3b). Significant ammonia formation was observed only in the system containing both nitrogen and ethanol (system D), with an average Faradaic efficiency of 5.8% (Fig. 4.3c). Li nitride yields were highest in this system as well, but remained low overall (Fig. 4.3d), supporting the idea that protonation of fixed nitrogen species is rapid and limits their accumulation at the electrode surface.[16,20,29] Hydrogen evolution was monitored using online gas chromatography, which revealed a substantial increase in hydrogen Faradaic efficiency in the presence of ethanol, rising from less than 2% to approximately 60% (Fig. 4.3e). This confirms that ethanol is the dominant hydrogen source. Galvanostatic

stripping[30-31] was used to quantify the remaining electrochemically connected Li metal. In systems without ethanol, more than half the charge passed corresponded to recoverable metallic Li. In contrast, systems with ethanol showed nearly complete consumption of metallic Li during operation (Fig. 4.3f). When the Faradaic efficiencies of ammonia, hydrogen, and Li nitride are combined, they account for approximately 60-70% of the total charge (Fig. 4.3b). The remaining charge likely contributes to the formation of inactive Li and the SEI. These experiments were led by my collaborators and provided the quantitative foundation for the interfacial analysis presented in the following sections.

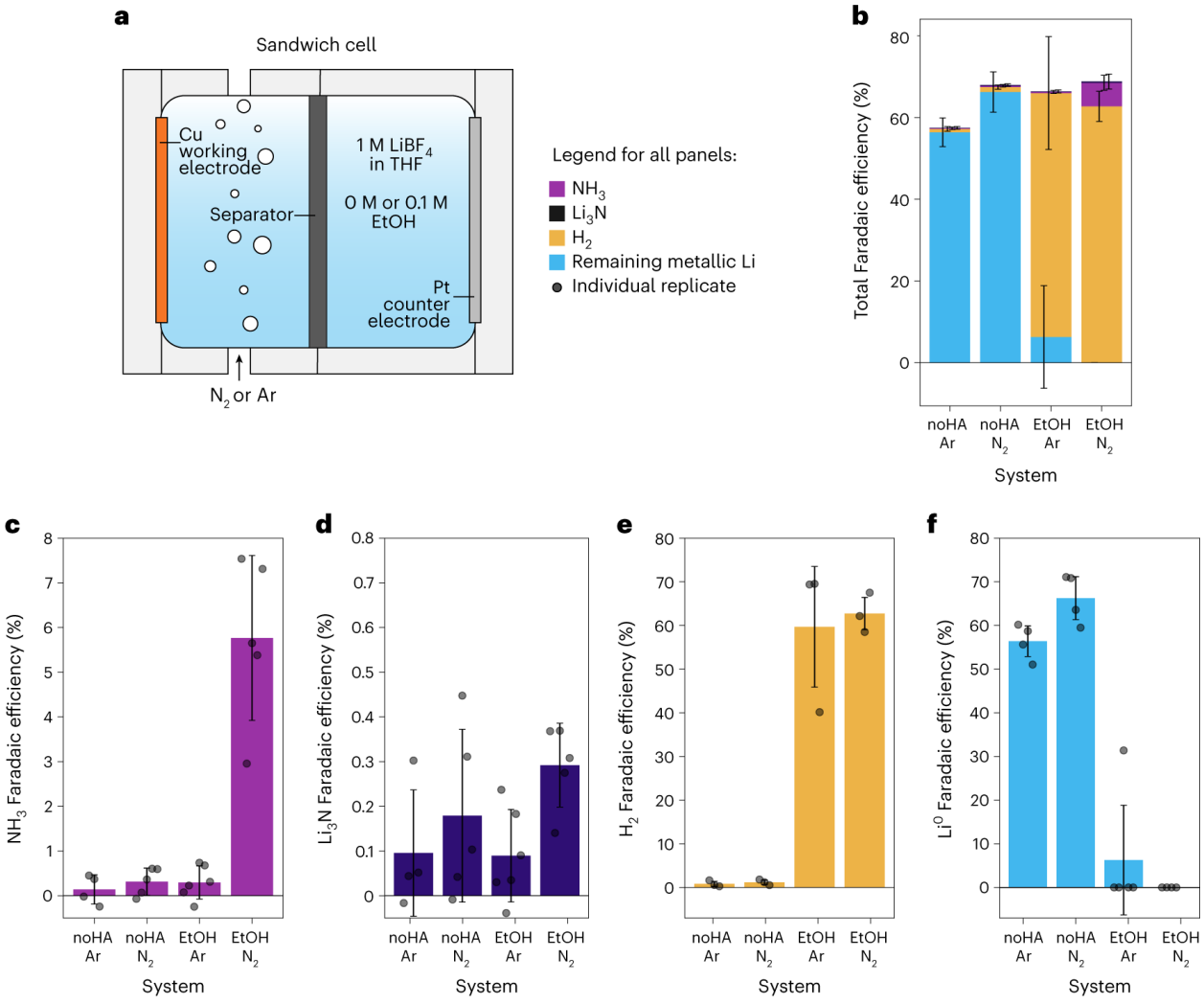

Fig. 4.3 Quantification of key products. a, Diagram of cell set-up used in these experiments. All experiments used a current density of −3 mA cm^{-2}, and total charge of 1 mAh. **b**, Total Faradaic efficiencies of quantified products, stacked vertically for each model system in the order Li^0, H_2, NH_3 and Li_3N, from bottom to top. Bars represent the mean of replicates shown in **c–f**, with error bars showing one standard deviation. Error bars are staggered such that they represent Li^0, H_2, NH_3 and Li_3N from left to right and are centred vertically at the top of the bar for each species. Average Faradaic efficiencies for **c**) ammonia, **d**) Li nitride, **e**) dihydrogen, **f**) remaining metallic Li.

To further understand the role of the proton donor in modulating Li surface reactivity, we investigated the morphology and interfacial composition of Li deposits using a combination of SEM and cryo-EM. SEM imaging was first employed to reveal morphological differences across the model systems. Representative images from nitrogen-containing systems with and without ethanol are shown in Fig. 4.4, and complete SEM and cryo-EM data for all four systems are provided in Figs. S4.1–S4.12. In the absence of ethanol, Li deposits formed under nitrogen atmosphere exhibit a typical morphology found in Li metal batteries, consisting of dense networks of filaments and larger agglomerates (Fig. 4.4a and Figs. S4.1e, Fig. S4.3). This morphology is nearly identical to that observed in the argon atmosphere without ethanol (Fig. S4.2), suggesting that the introduction of nitrogen alone does not significantly alter Li metal deposition. In contrast, when ethanol is introduced as a proton donor, the morphology changes markedly (Fig. 4.4e). Instead of mossy Li filaments, we observe the formation of rounded, discontinuous particles scattered on the Cu substrate, with many regions of bare Cu foil visible (Fig. 4.4e and Fig. S4.1m, Fig. S4.5). These deposits display low contrast and image smearing under the electron beam,

consistent with the charging behavior expected of electrically insulating materials.[32] This observation suggests that the deposits are predominantly composed of the SEI components rather than metallic Li. Taken together, these data imply that the presence of ethanol alters the passivation dynamics at the Li surface, leading to morphologies dominated by SEI residue instead of Li metal.

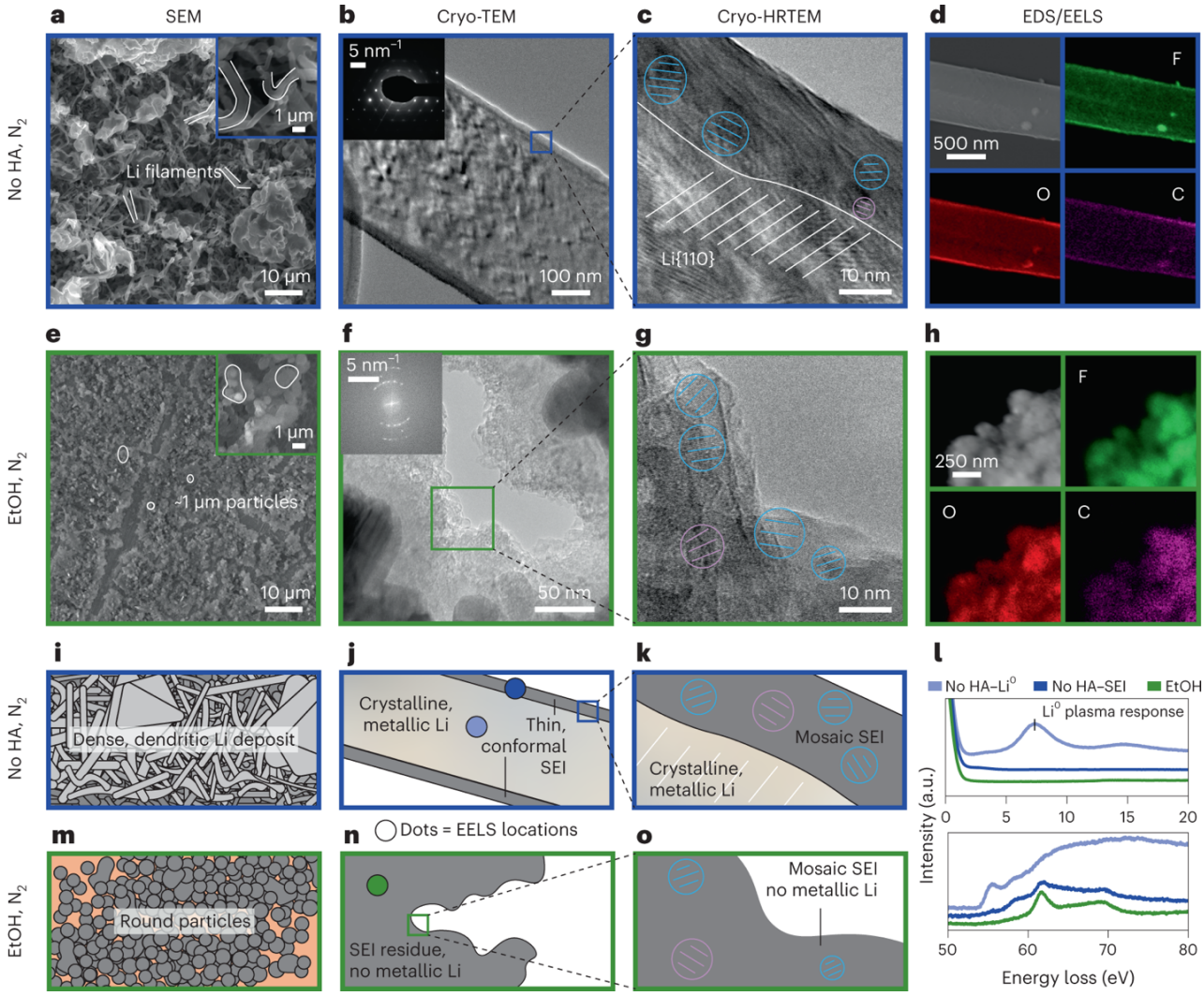

Fig. 4.4 Imaging results from the 'no HA, N_2' and 'EtOH, N_2' model systems. a, SEM image of the 'no HA, N_2' system, with inset at higher magnification. **b**, Cryo-EM image of the 'no HA, N_2' system, with inset SAED image. **c**, High-resolution cryo-EM image of the 'no HA, N_2' system,

with the Li lattice and several of the mosaic SEI crystalline regions annotated. **d**, Cryo-STEM EDS mapping of the 'no HA, N_2' system. **e–h**, analogous images to **a–d** but collected on the 'EtOH, N_2' system. Note that f includes an inset fast Fourier transform of image g rather than SAED, but both are included in Fig. S4.11. **i–k, m–o**, Illustrations of the morphology observed at different scales of imaging for each sample. Dots in j and n represent the three regions used to generate EELS spectra in l. **l**, Representative cryo-STEM EELS spectra of the 'no HA, N_2' sample collected in the metallic Li region (light blue) and the SEI region (darker blue) and of the 'EtOH, N_2' sample. Top plot displays the low-loss region, and bottom plot displays the Li K-edge core-loss region. Enlarged versions of all the images shown here and corresponding images for Ar-feed gas model systems can be found in Figs. S4.2-4.13.

To gain higher-resolution insight into these surface structures and their composition, we turned to cryo-EM. We developed a sample preparation protocol for this system based on the experience in Li metal batteries (Fig. 4.5).[26] To prepare cryo-EM samples, Cu-based transmission electron microscopy (TEM) grids were placed at the working electrode together with Cu foil during electrochemical operation. Following each experiment, the grids were plunge-frozen in liquid nitrogen. The cryo-transfer process prevents the exposure of Li metal and SEI to air and moisture, thereby preserving their native state. Cryogenic imaging conditions further stabilize the highly reactive Li–SEI interface and minimize electron beam-induced damage, enabling visualization of nanostructures that are otherwise difficult to observe using conventional TEM at room temperature.

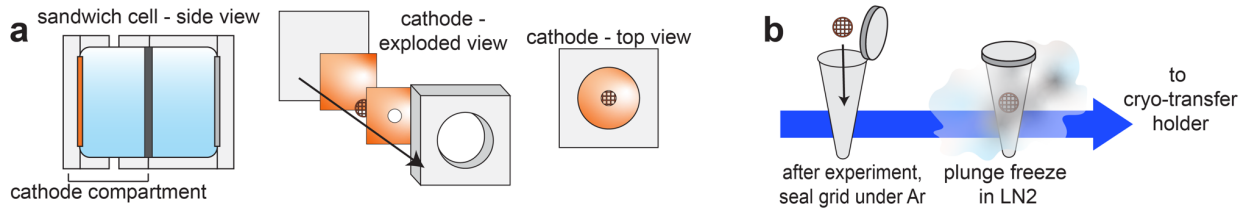

Fig. 4.5 Illustration of cryo-EM sample preparation process. a, TEM grids are sandwiched between Cu foils at the working electrode to expose the grid to LiMEAS surface conditions. **b**, After experiments, TEM grids are sealed under Ar then plunge-frozen in liquid nitrogen before transferring to a cryo-transfer holder for imaging.

Cryo-EM imaging of samples formed without ethanol (systems A and B) reveals Li deposits that closely resemble those documented in the battery literature.[25-27] Selected area electron diffraction (SAED) patterns display sharp spots consistent with crystalline Li, oriented along the [011] and [111] zone axes (Fig. 4.2b and Fig. S4.10). High-resolution images show well-defined lattice fringes matching the {110} planes of Li metal (Fig. 4.4c and Fig. S4.7). The SEI appears as a 20–30 nm thick coating surrounding the Li filaments, characterized by a mosaic-like microstructure (Fig. 4.4c).[25-26] This structure includes domains of crystalline inorganic species embedded in an amorphous organic matrix. Based on lattice spacing measurements, the crystalline regions are assigned to Li fluoride (LiF) and either Li hydroxide (LiOH) or Li oxide (Li_2O). In contrast, cryo-EM of samples formed with ethanol (systems C and D) shows no evidence of metallic Li. Instead, the observed structures are composed entirely of SEI-type materials (Fig. 4.4e and Fig. S4.8, Fig. S4.9). Fast Fourier transforms (FFT) of high-resolution images reveal polycrystalline ring patterns, with lattice spacings corresponding to LiF and LiOH (Fig. 4.4f and Fig. S4.10). Similar to the SEI in the ethanol-free systems, the SEI formed in the presence of ethanol exhibits a heterogeneous

mosaic structure with interspersed crystalline and amorphous regions (Fig. 4.4g and Fig. S4.10). However, in these samples, no regions consistent with crystalline Li are observed. The amorphous domains are highly beam-sensitive and exhibit structural changes under prolonged exposure, reinforcing their assignment as non-metallic SEI components.

To complement imaging and diffraction data, we performed elemental mapping using scanning transmission electron microscopy (STEM) coupled with energy-dispersive X-ray spectroscopy (EDS). Elements heavier than boron were detected in all samples. In both ethanol-containing and ethanol-free systems, fluorine, oxygen, and carbon are present and are uniformly distributed within the SEI regions. In ethanol-free samples, these elements are primarily concentrated near the Li-SEI interface, suggesting a compact but compositionally homogeneous SEI (Fig. 4.4d). In ethanol-containing systems, the elemental distribution remains similarly uniform throughout the deposits (Fig. 4.4h), consistent with the formation of a bulk-like SEI rather than a layered structure.

To further probe chemical bonding and validate phase assignments, we performed electron energy loss spectroscopy (EELS) on samples from both ethanol-free and ethanol-containing systems, using nitrogen as the feed gas. Low-loss EELS spectra from the ethanol-free samples confirm the presence of metallic Li, with a distinct plasmon peak near 7.5 eV (Fig. 4.4l).[24] The Li K-edge core-loss spectra also show a sharp feature at approximately 55 eV,[33] further confirming the metallic nature of these regions. In contrast, the ethanol-containing samples lack these signatures and instead exhibit spectral features corresponding to LiF, indicating the dominance of fluoride-rich SEI in these conditions. The ethanol-free samples also show additional Li K-edge features

consistent with LiOH, suggesting that the SEI in these systems includes a broader range of inorganic components.

Together, cryo-EM results and complementary analyses suggest that the presence of ethanol fundamentally alters interfacial chemistry in LiMEAS by disrupting the formation of a passivating SEI. In ethanol-free systems, the SEI forms from the reduction of electrolyte components such as THF and BF_4^-, resulting in a compact, inorganic-rich interphase that effectively blocks nitrogen access to metallic Li. Although Li-ions can still migrate through the SEI, the lack of electron or nitrogen transport leads to the accumulation of dendritic Li metal without productive nitrogen fixation (Fig. 4.6a). In contrast, when ethanol is introduced, the SEI becomes dominated by amorphous organic species derived from ethanol decomposition. This ethanol-modified interphase appears more permeable to both nitrogen and electrolyte species, enabling continuous Li consumption at the surface and promoting the desired thermochemical reactivity (Fig. 4.6b).

High-resolution cryo-EM images reveals that while the inorganic, crystalline SEI phases such as LiF and LiOH remain largely intact across both conditions, the amorphous organic matrix is significantly disrupted in the presence of ethanol. This structural disruption may occur through several pathways. While the precise mechanism by how ethanol enables continuous Li metal reactivity remains under investigation, several hypotheses can be proposed based on our observations (Fig. 4.6c).

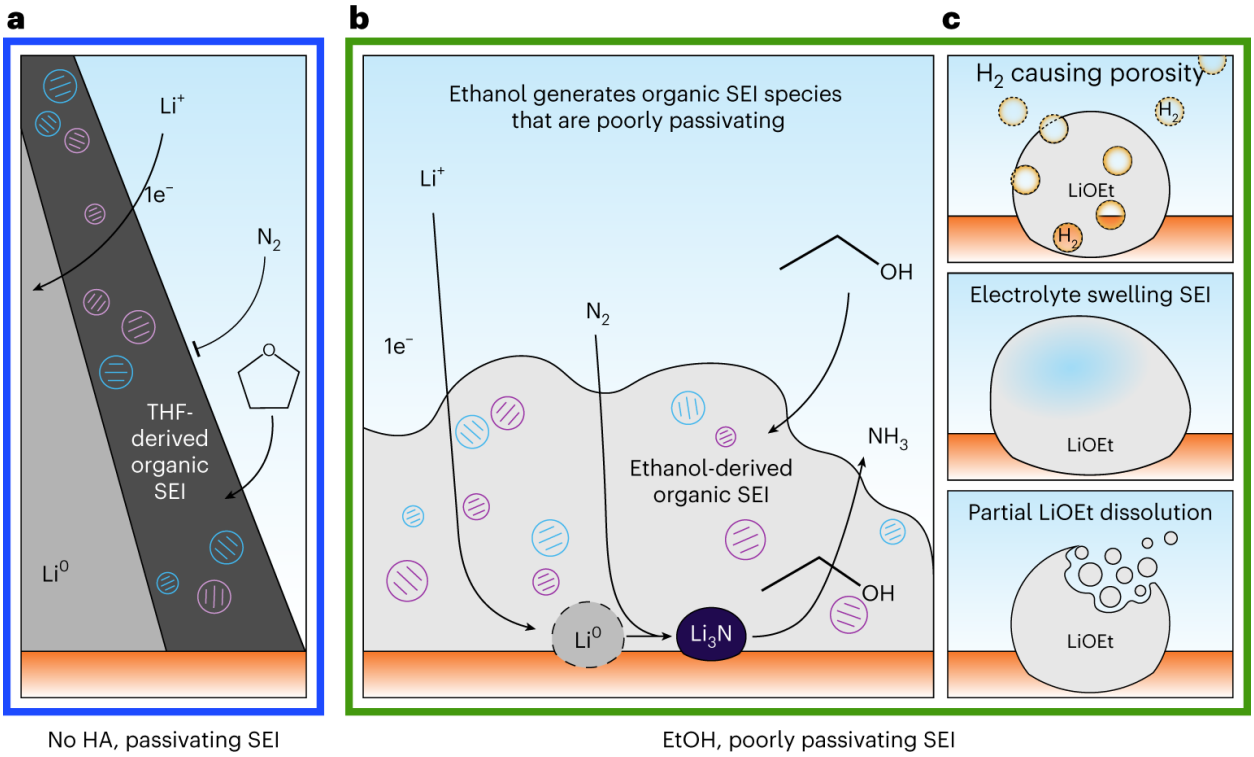

Fig. 4.6 SEI materials and their role in LiMEAS. a, SEI generated by THF and $LiBF_4$ breakdown in the absence of proton donor inhibits N_2 reactivity with Li. **b**, The addition of ethanol leads to organic components of the SEI that are permeable to nitrogen and other electrolyte components, enabling Li reactivity including nitrogen fixation. **c**, Mechanisms by which ethanol-derived SEI materials could result in poor passivation. Top to bottom, poor passivation could result from hydrogen gas generation that induces porosity in the SEI, from a high degree of SEI swelling in electrolyte, or because of partial solubility of SEI components, such as Li ethoxide (LiOEt).

One possibility is that hydrogen gas generated from the reaction between Li and ethanol mechanically disrupts the SEI, compromising its structural integrity and allowing nitrogen and electrolyte to reach the reactive Li surface. A second possibility is that ethanol directly contributes to the formation of SEI species that are inherently less passivating and more permeable to

dinitrogen, thereby facilitating interfacial reactivity. A third hypothesis is based on prior cryo-EM studies of vitrified interfaces, which have shown that SEIs swell in the presence of electrolyte, particularly when rich in organic components. Such swelling has been correlated with poor Li passivation and unstable cycling behavior. By analogy, an ethanol-derived SEI, composed primarily of amorphous organic products, may swell more readily, increasing contact between dissolved nitrogen and metallic Li. Additionally, if Li ethoxide is even partially soluble in the electrolyte, SEI components may be lost to dissolution, further destabilizing the interphase and enabling sustained reactivity.

These findings collectively redefine the role of the SEI in LiMEAS. Unlike in batteries, where the SEI is typically valued for its ability to passivate and protect Li metal, LiMEAS requires a reactive interphase that enables sustained Li metal consumption by nitrogen. Through a multiscale approach combining product quantification with high-resolution imaging, we identified the proton donor as the key driver of surface reactivity. In the absence of a proton donor, Li metal accumulates at the electrode as mossy deposits coated with a passivating SEI, inhibiting nitrogen fixation. In contrast, ethanol-derived SEIs are dominated by amorphous organic products that enable continuous Li reactivity, likely by increasing interphase permeability and structural instability. Although the role and behavior of Li metal and the SEI differ fundamentally between batteries and LiMEAS, insights from the battery field remain highly instructive. For example, electrolyte design in Li metal batteries often aims to promote the formation of stable and passivating SEI, and the underlying design principles, including solvent structures and interphase engineering, can be reconsidered in reverse to guide the development of porous and reactive SEIs needed for LiMEAS.

4.4 Conclusion

In this study, we used a multiscale approach combining products quantification and cryo-EM to uncover how surface chemistry governs reactivity in LiMEAS. We identified the proton donor as a key factor controlling interfacial behavior: without it, Li is passivated by a dense SEI; with it, Li remains reactive under a disordered, amorphous-rich interphase. Cryo-EM enabled direct visualization of these interfacial structures, offering rare insight into SEI morphology and composition under reactive conditions. Although LiMEAS requires a porous SEI layer that enables continuous Li metal reactivity, which is different from the SEI in Li metal batteries, design strategies from battery systems can inform the development of porous and reactive SEIs for LiMEAS. Conversely, insights from LiMEAS broaden our understanding of dynamic interfacial chemistry, highlighting the value of cross-system learning in electrochemical interface design.

4.5 Methods

Cryo-TEM sample preparation and imaging

To deposit Li metal on TEM grids, one to four TEM grids were incorporated into the working electrode set-up as illustrated in Fig. 4.5 and Fig. 4.7-8. This set-up ensured that the grids were electrically connected to the copper working electrode and exposed to electrolyte and thus could accumulate Li and its passivation species just like the rest of the working electrode. After the experiment, the cell was deconstructed and the TEM grids were carefully rinsed with a few drops of anhydrous THF. The TEM grid was then sealed in an individual Teflon-sealed Eppendorf tube by tightly capping it and wrapping with parafilm. The Eppendorf tubes were then removed from the glovebox and quickly plunged in liquid nitrogen to freeze. Because the pressure in the glovebox, and thus the Eppendorf tube, was greater than ambient pressure, the tubes were air-tight during

transfer. Bolt cutters were used to quickly break open the Eppendorf tube and expose the grid to cryogen, and tweezers were used to move the grids into a cryo-grid box for storage, all under liquid nitrogen. For ease of storage and transport, polypropylene centrifuge tubes with strings attached were used to scoop up the grid boxes in liquid nitrogen and then transferred to a thermos, with the strings used to label and access individual grid boxes. Samples could be stored in the thermos under liquid nitrogen for several hours before imaging.

To conduct cryo-TEM, samples were affixed to a Gatan 626 cryo-transfer holder using a cryo-transfer station to ensure that the whole process occurred under LN_2. The transfer holder's built-in shutter was kept closed over the sample while inserting the sample into the TEM column (~1 s), preventing contact between the sample and air. After sample insertion, the cryo-transfer holder maintains the grid temperature at −178 °C. All TEM imaging was performed using a FEI Titan 80–300 scanning transmission electron microscope operated at an accelerating voltage of 300 kV, an instrument in the UCLA's CNSI's Electron Imaging Center for Nanomachines. It is equipped with an extreme field-emission gun (X-FEG), Oxford X-MaxTEM 100 N TLE Windowless silicon drift detector (SDD) 100 mm^2 EDS, and a Gatan Ultrascan 2 K × 2 K charge-coupled device (CCD) camera.

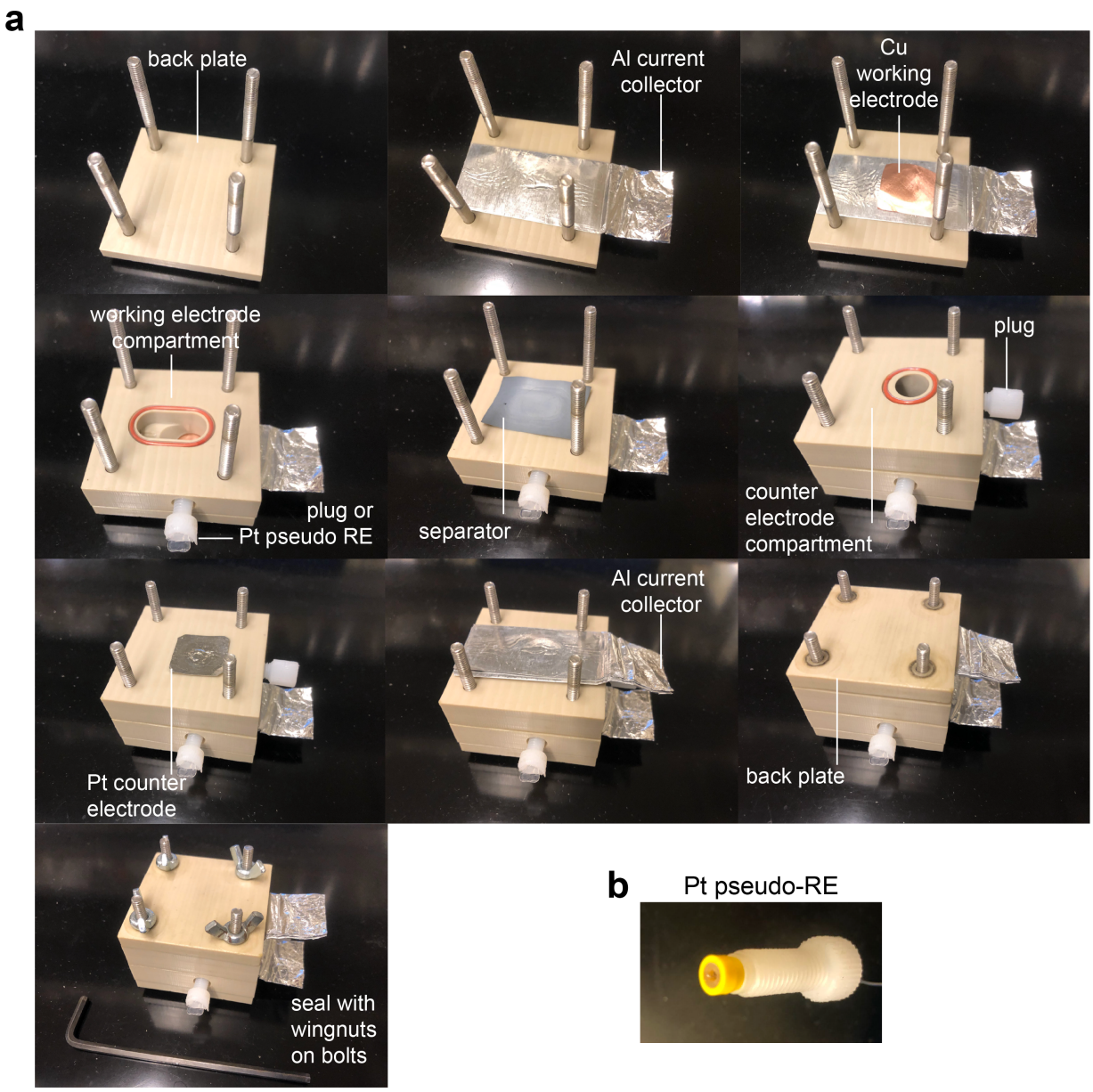

Fig. 4.7 Sandwich cell construction. a, Steps for constructing the sandwich cells used in this study. b, Image of Pt pseudo-RE used here.

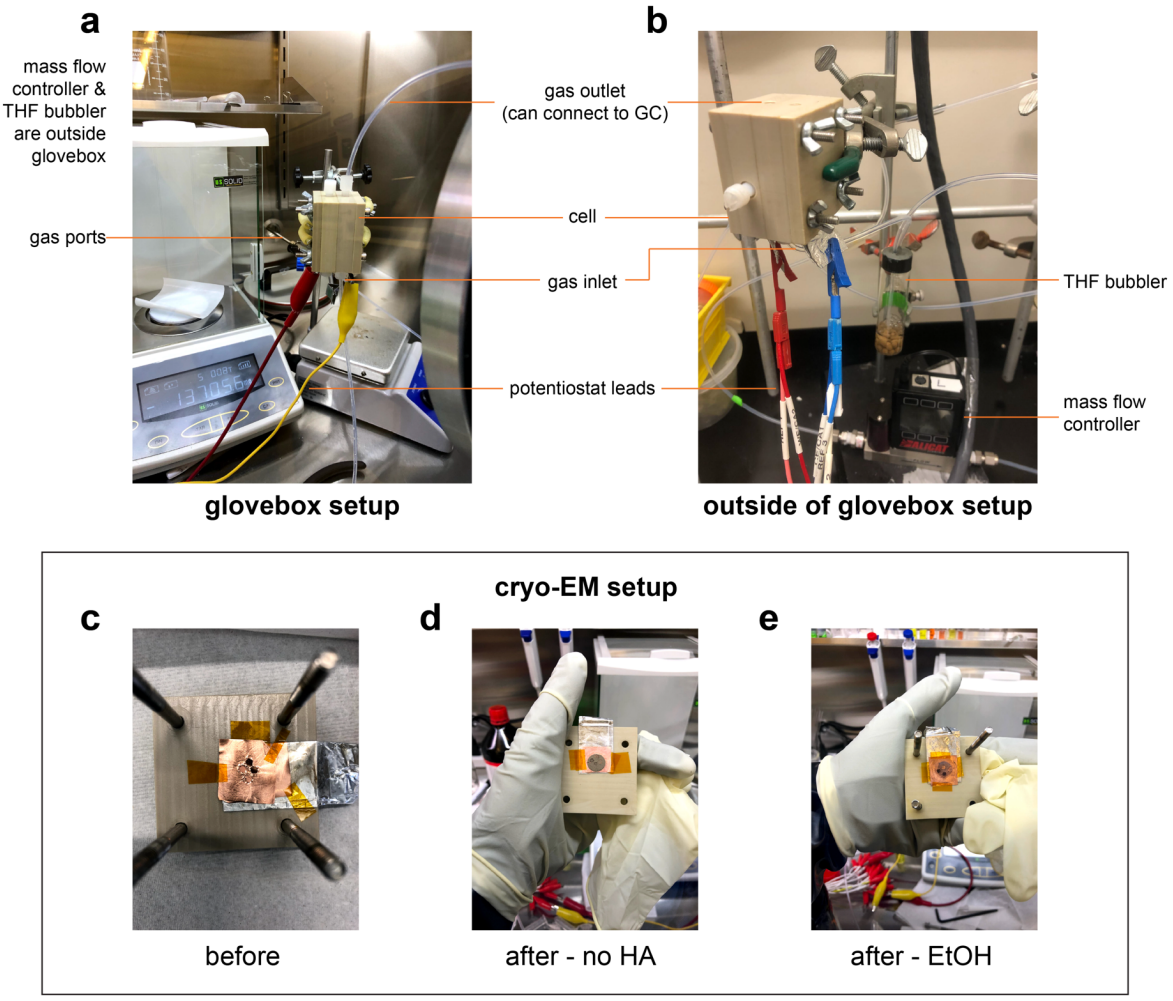

Fig. 4.8 Experimental setups used in this study. a, Cell setup used in glove box for imaging and characterization experiments. b, Cell setup used for experiments outside the glovebox, such as product quantification. c-e, Cryo-EM setup to incorporate TEM grids at the working electrode. Usually, each cell had four grids included, two Cu grids and two lacey carbon grids with deposited Cu chunks. Note that the lacey carbon grids appear darker in color against the Cu before experiments were performed in c. Typical working electrode appearance after experiments is shown in d and e, with experiments with no proton donor demonstrating a dense and mossy deposit (d) and experiments with ethanol having a less obvious surface deposit (e).

Electron flux is less than 100 e $Å^{-2}$ s^{-1} for low-magnification TEM images and less than 1,000 e $Å^{-2}$ s^{-1} for high-resolution TEM images. The electron beam exposure time of each image is no more than 30 s, and the acquisition time is 0.4 s to 1 s.

For additional experimental details, please refer to the published paper: Steinberg, K.; Yuan, X.; Klein, C. K.; Lazouski, N.; Mecklenburg, M.; Manthiram K.; Li, Y. Imaging of nitrogen fixation at Li solid electrolyte interphases via cryo-electron microscopy. *Nature Energy* **8**, 138-148 (2023).

4.6 Supplementary figures

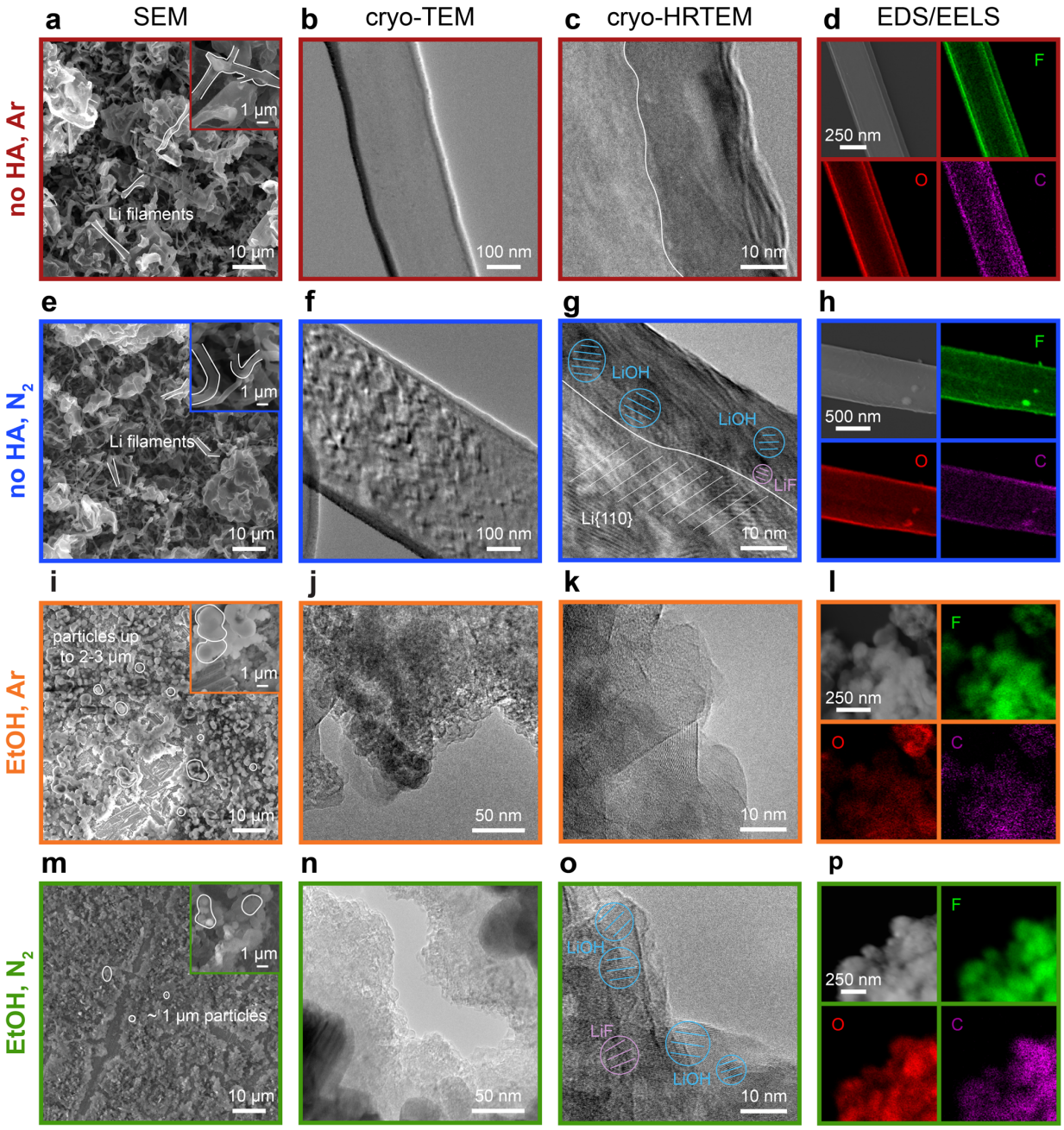

Fig. S4.1 Imaging results for all four model systems. a, SEM image of the no HA, Ar system, with inset at higher magnification. **b**, Cryo-TEM image of the no HA, Ar system. **c**, High-resolution cryo-TEM image of the no HA, Ar system, with the SEI-Li interface annotated. **d**, Cryo-STEM EDS mapping of the no HA, Ar system. **e-h, i-l**, and **m-p**, analogous images to **a-d**, but

collected on the other model systems. Enlarged versions of these images can be found in Fig. S4.2-11.

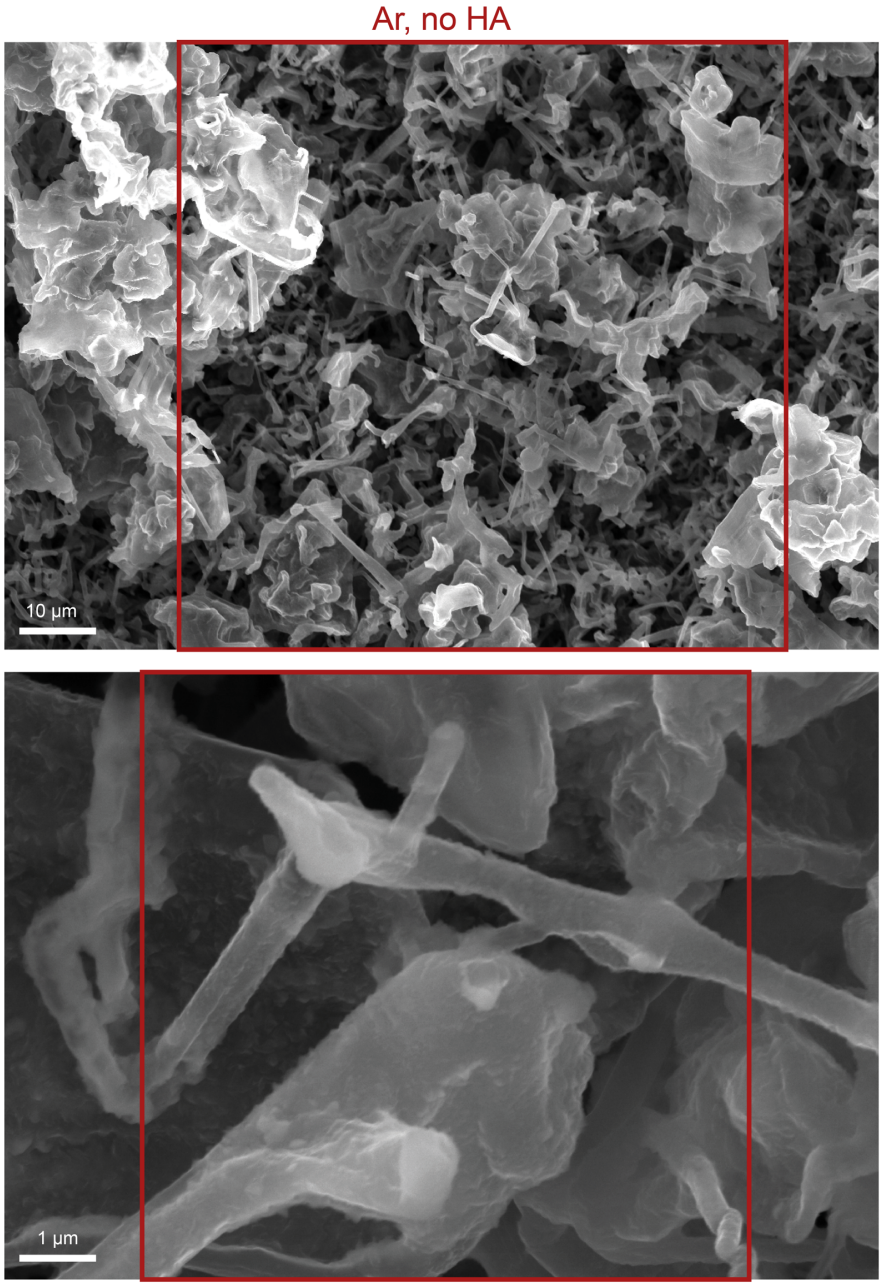

Fig. S4.2 Enlarged versions of the SEM images shown in Fig. S4.1 for the Ar, no HA case. Red boxes denote the areas used for the cropped versions.

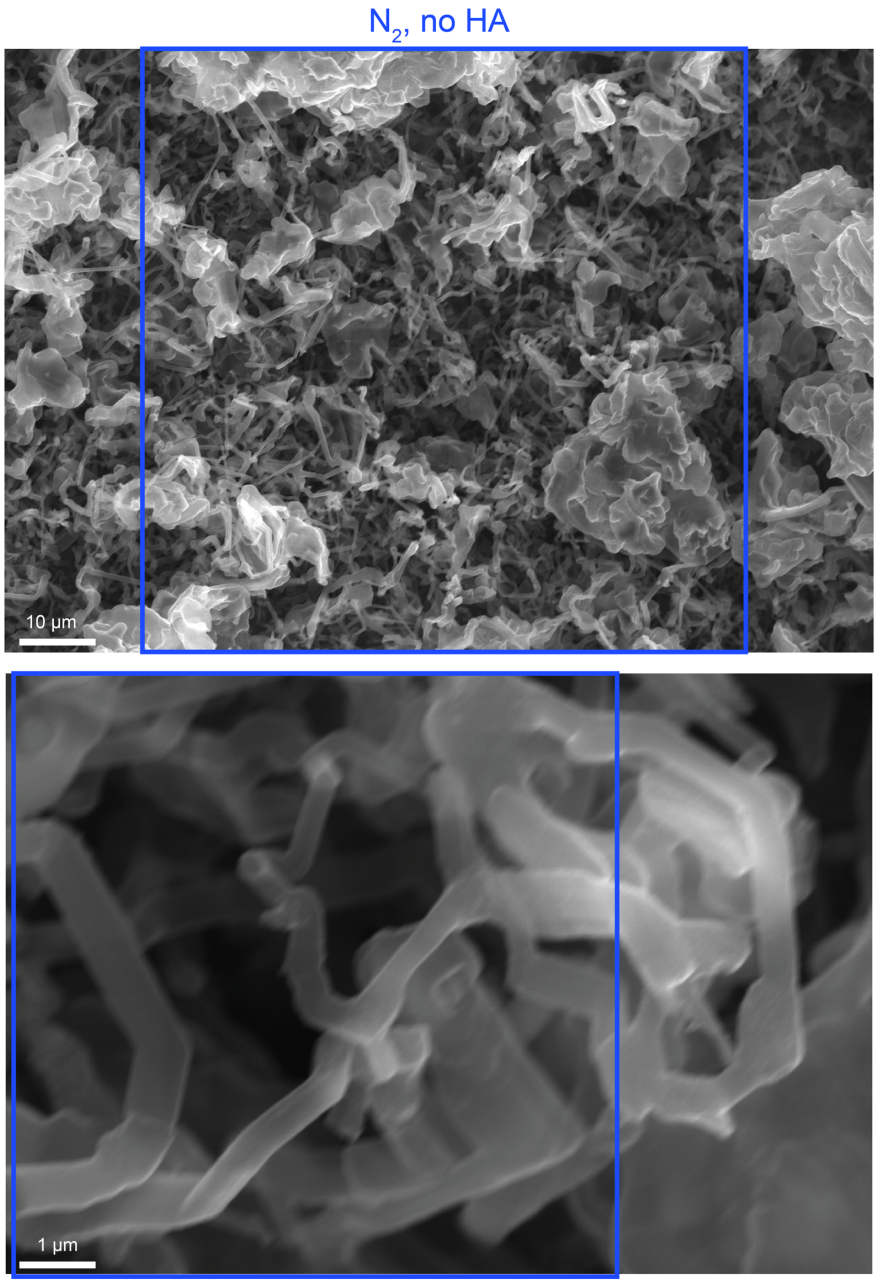

Fig. S4.3 Enlarged versions of the SEM images shown in Fig. 4.4 and Fig. S4.1 for the N_2, no HA system. Blue boxes denote the areas used for cropped versions.

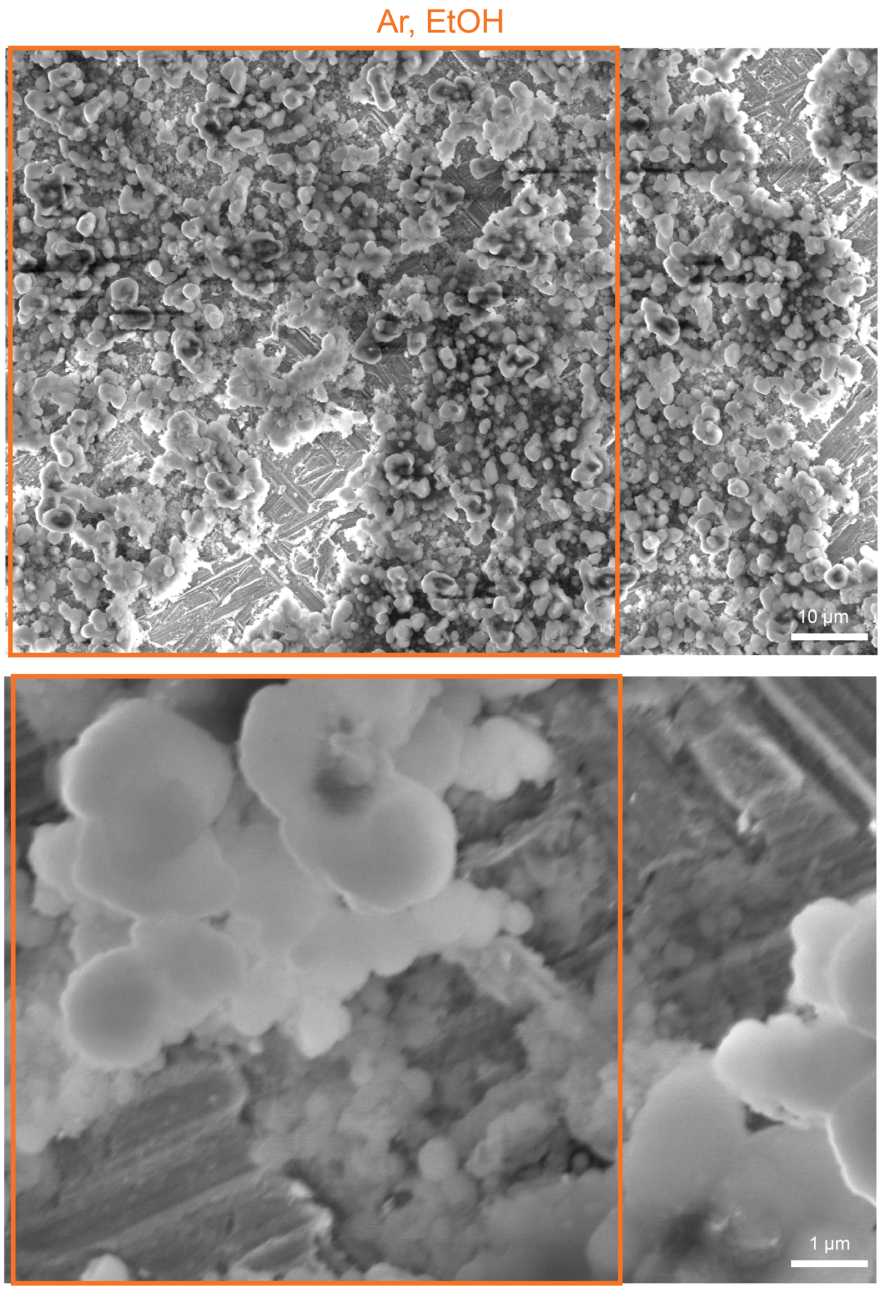

Fig. S4.4 Enlarged versions of the SEM images shown in Fig. S4.1 for the Ar, EtOH system.

Orange boxes denote the areas used for the cropped versions.

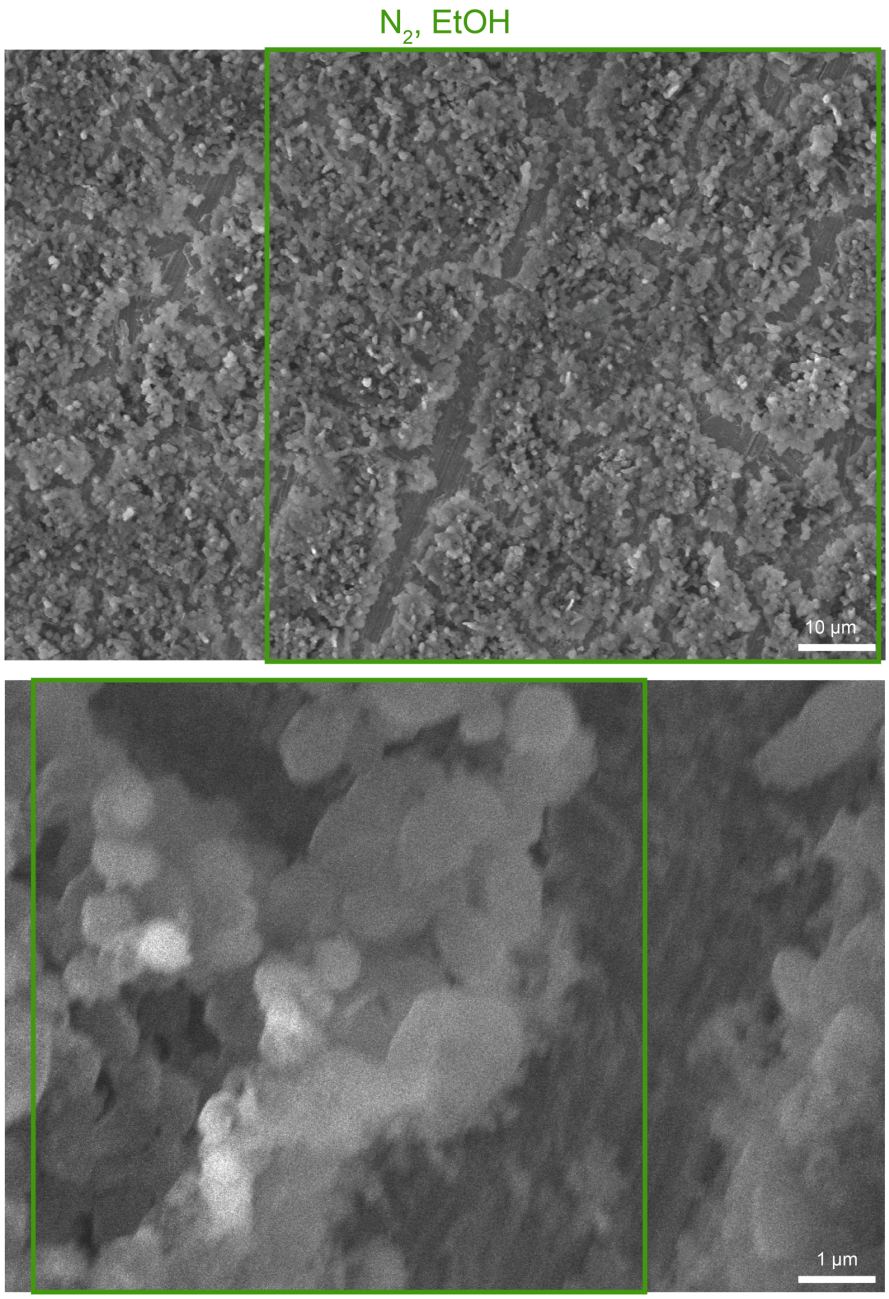

Fig. S4.5 Enlarged versions of the SEM images shown in Fig. 4.4 and Fig. S4.1 for the N_2, no HA system. Green boxes denote the areas used for the cropped versions.

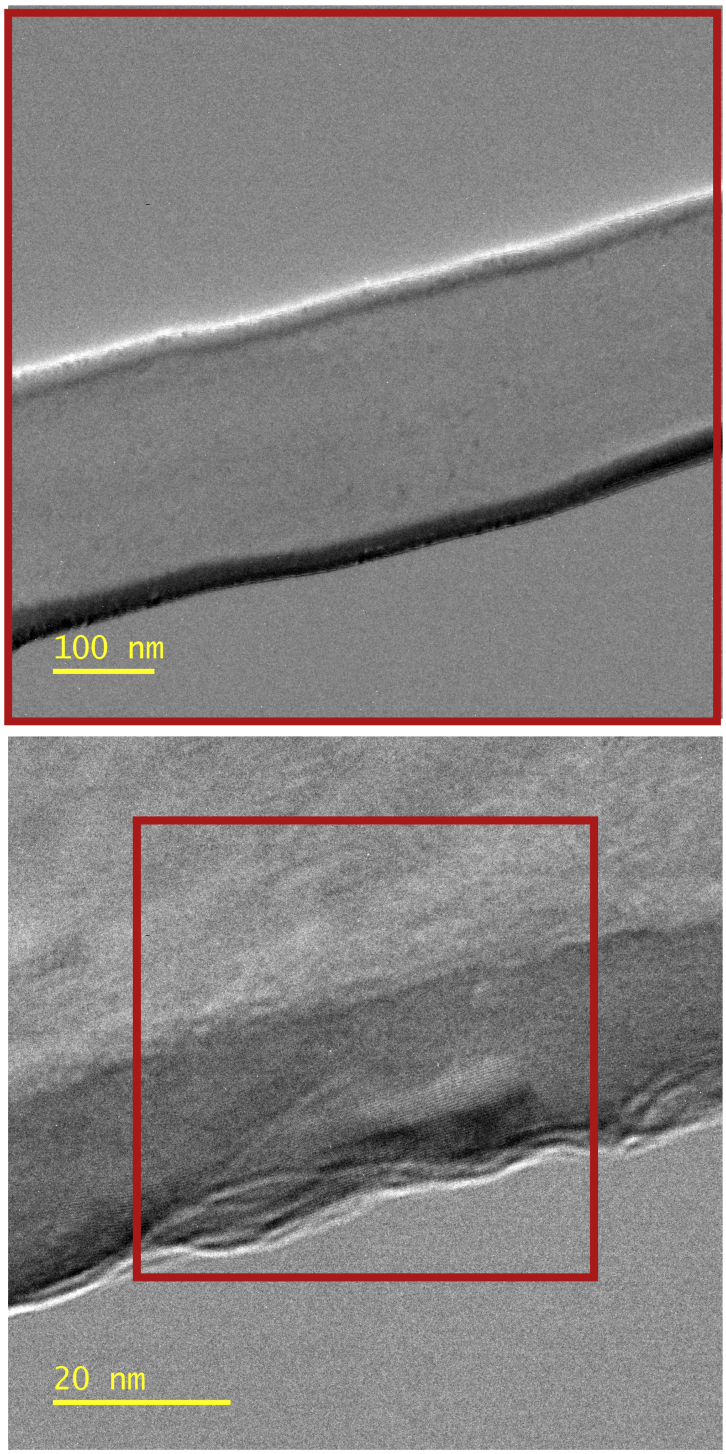

Fig. S4.6 Enlarged versions of the cryo-TEM images shown in Fig. S4.1 for the Ar, no HA system. Red boxes denote the areas used for the cropped versions**.**

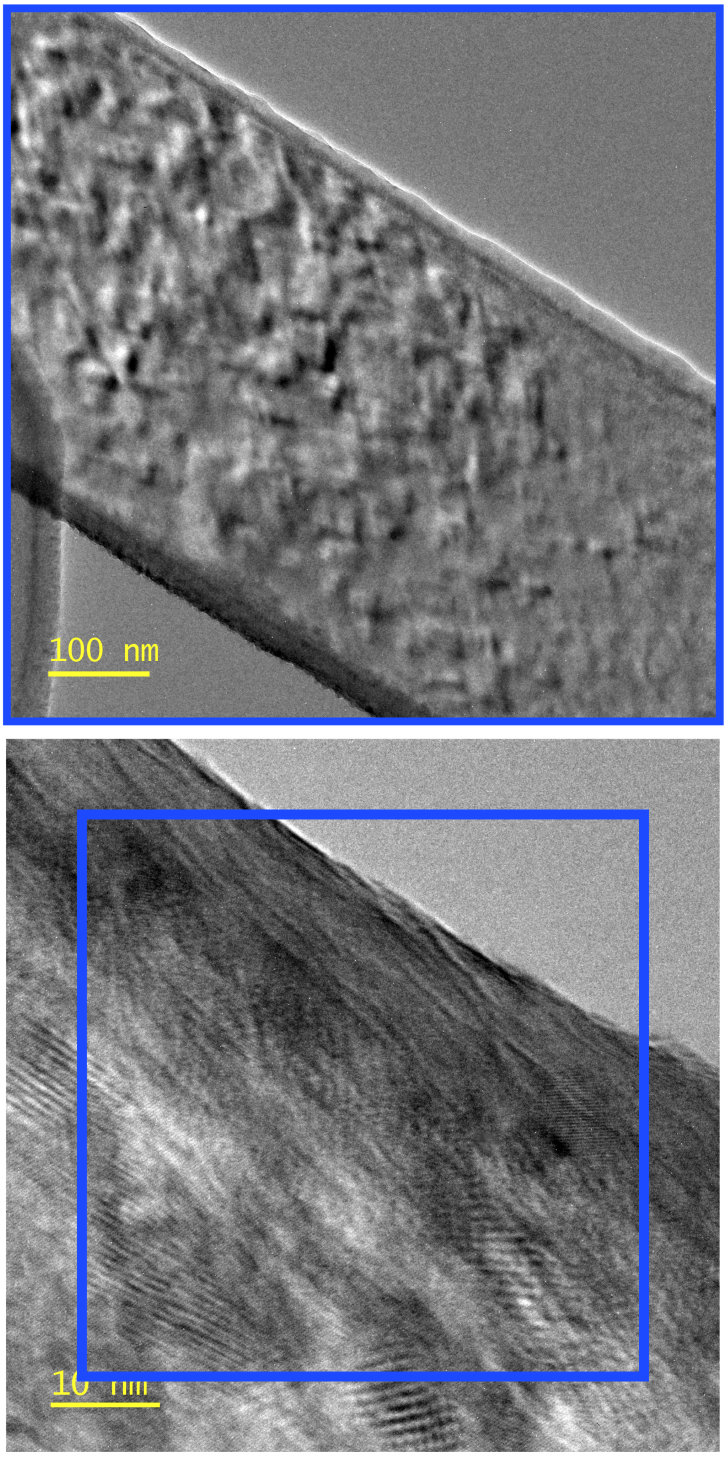

Fig. S4.7 Enlarged versions of the cryo-TEM images shown in Fig. 4.4 and Fig. S4.1 for the N_2, no HA system. Blue boxes denote the areas used for cropped versions.

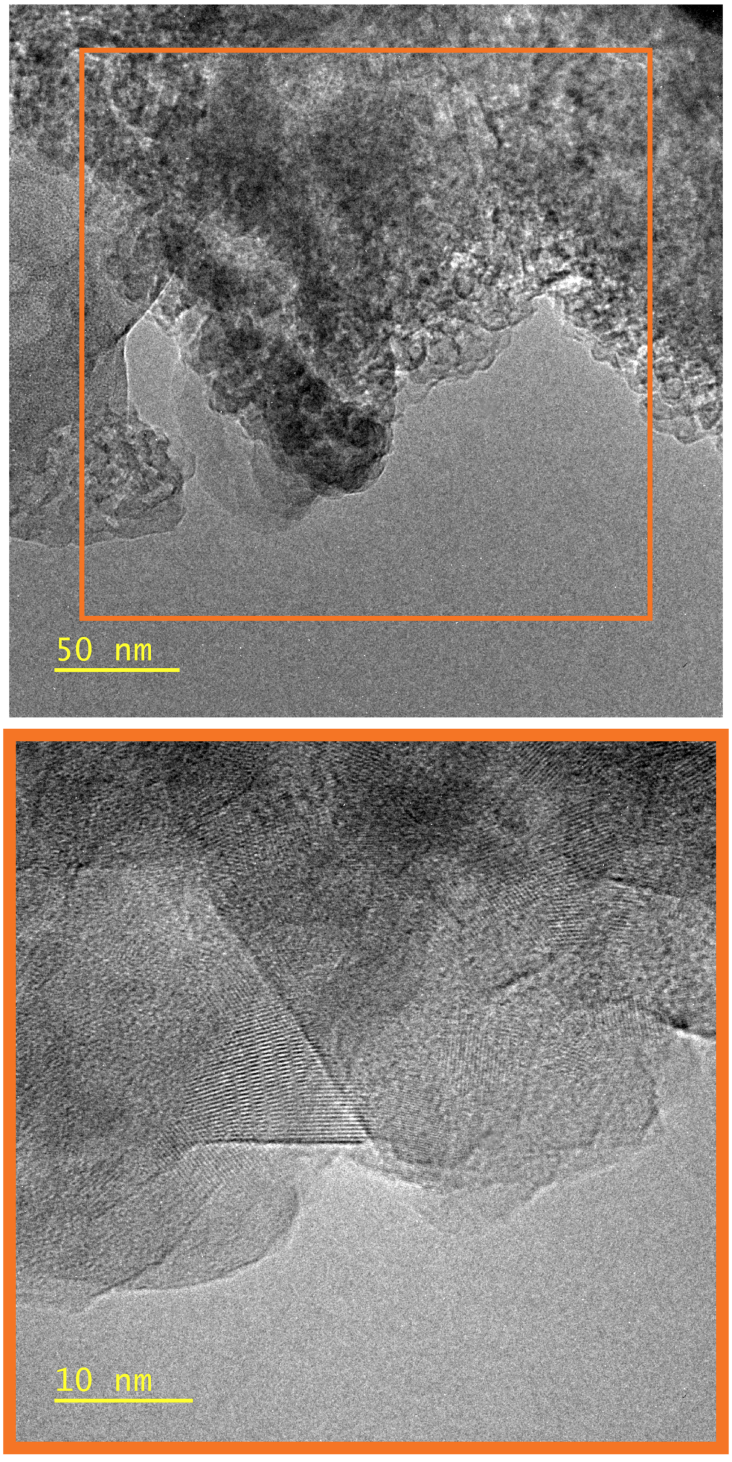

Fig. S4.8 Enlarged versions of the cryo-TEM images shown in Fig. S4.1 for the Ar, EtOH system. Orange boxes denote the areas used for cropped versions.

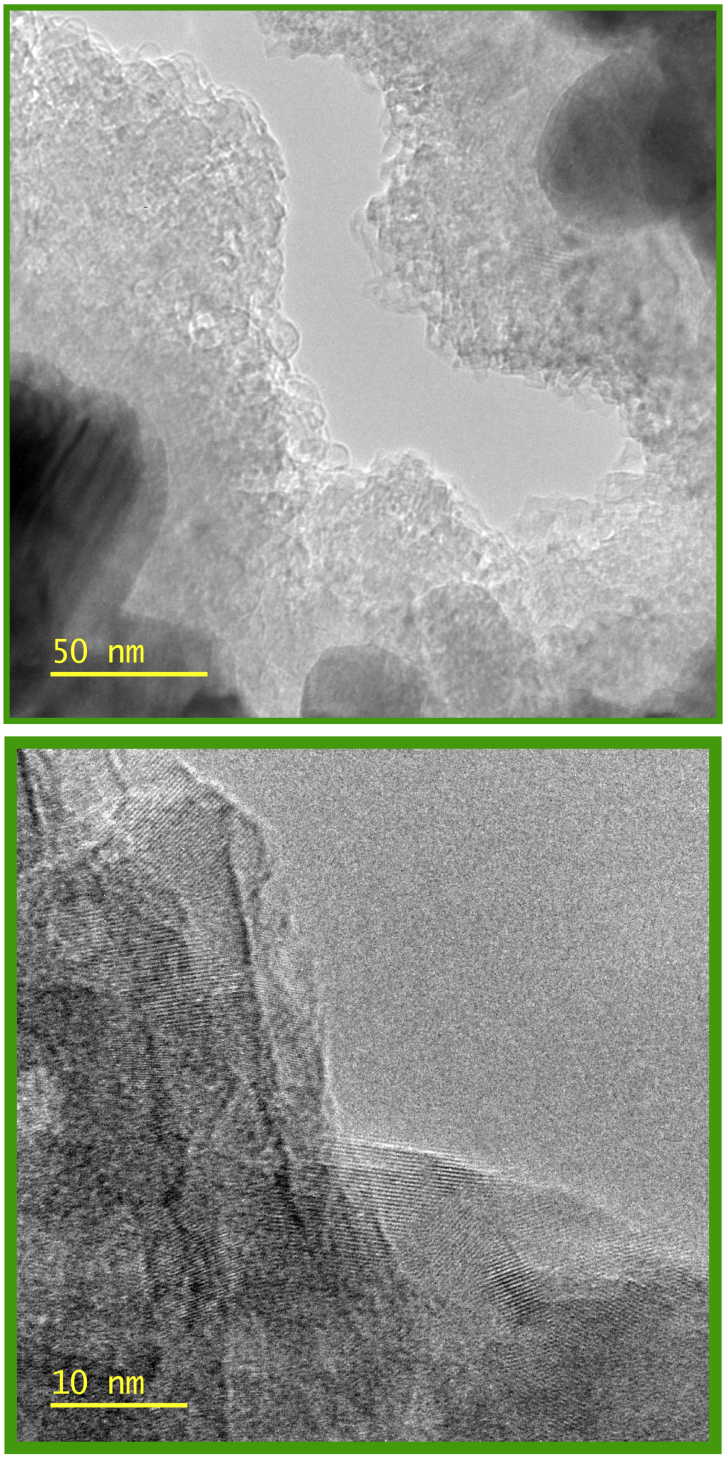

Fig. S4.9 Enlarged versions of the cryo-TEM images shown in Fig. 4.4 and Fig. S4.1 for the N_2, EtOH system. Green boxes denote the areas used for cropped versions.

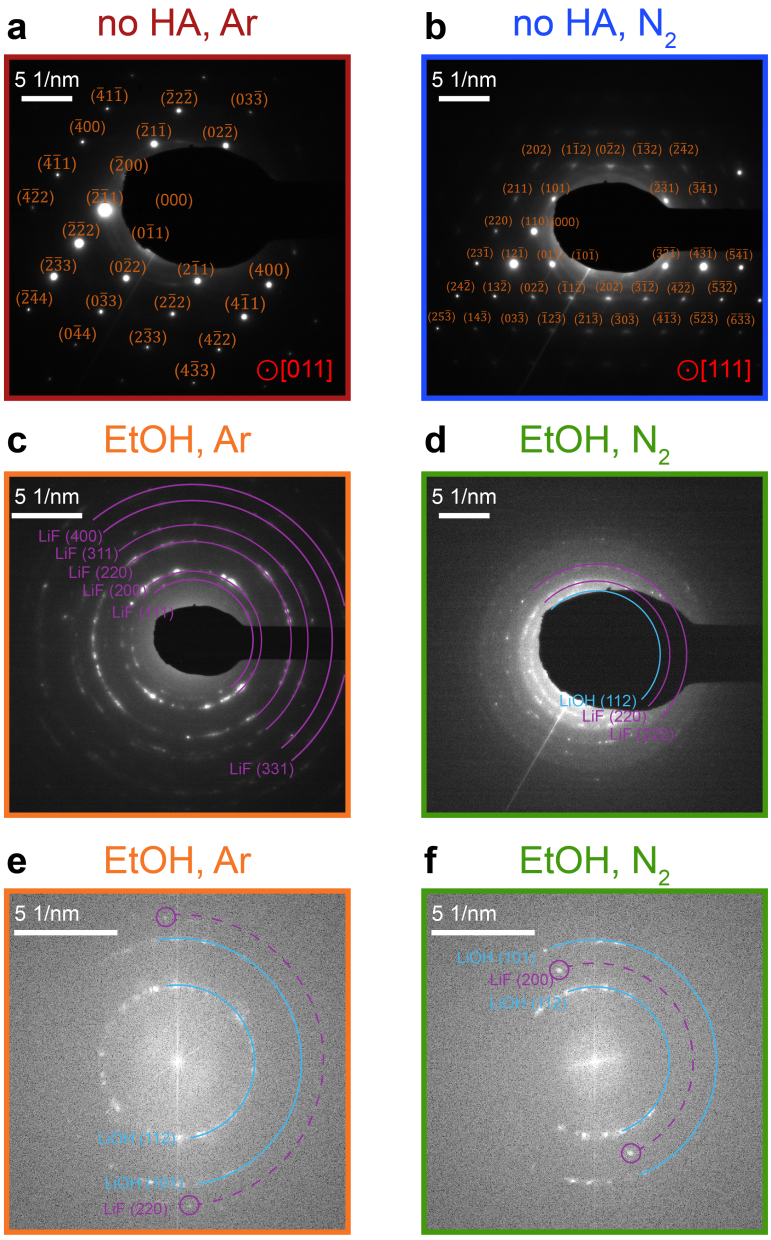

Fig. S4.10 Enlarged and indexed versions of cryo-TEM SAED and FFT images. a, Ar, no HA SAED. **b**, N_2, no HA SAED. **c**, Ar, EtOH SAED. **d**, N_2, EtOH SAED. **e**, Ar, EtOH FFT of HRTEM image. **f**, N_2, EtOH FFT of HRTEM image. Miller indices are assigned for **a**, **b**, which correspond to crystalline Li viewed along the [011] and [111] zone axis, respectively. **c-f** are labelled with relevant crystalline phases that match each polycrystalline ring.

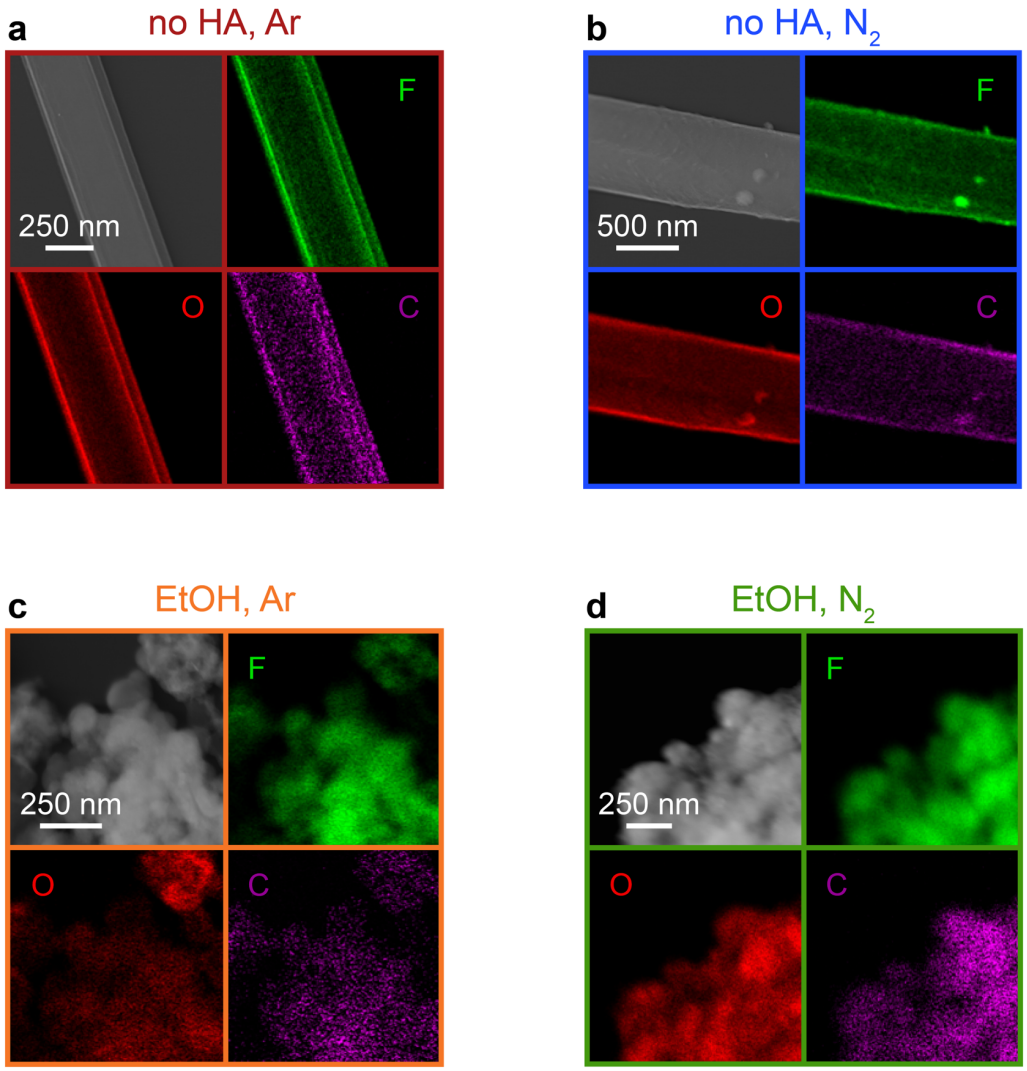

Fig. S4.11 Cryo-STEM EDS mapping of each of the model systems, enlarged versions of those shown in Fig. 4.4 and Fig. S4.1. Note that EDS provides only elemental analysis, not information about chemistry or local bonding environments, and only detects elements heavier than boron. These limitations were part of the motivation behind conducting XPS on the same four model systems, but EDS maps can still provide insights into the elements present in SEI species, and local variations in elemental composition. Maps are shown only for the elements detected above the spectrometer threshold concentration.

a

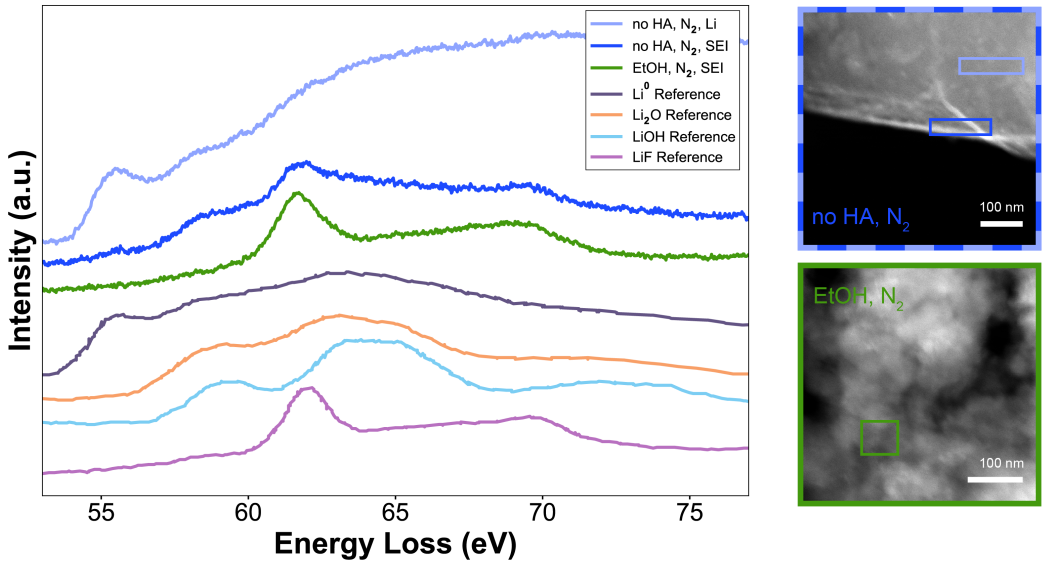
no HA, N2, Li
no HA, N2, SEI
EtOH, N2, SEI
Li0 Reference
Li2O Reference
LiOH Reference
LiF Reference
Intensity (a.u.)
55
60
65
70
75
Energy Loss (eV)
no HA, N2
100 nm
EtOH, N2
100 nm

b

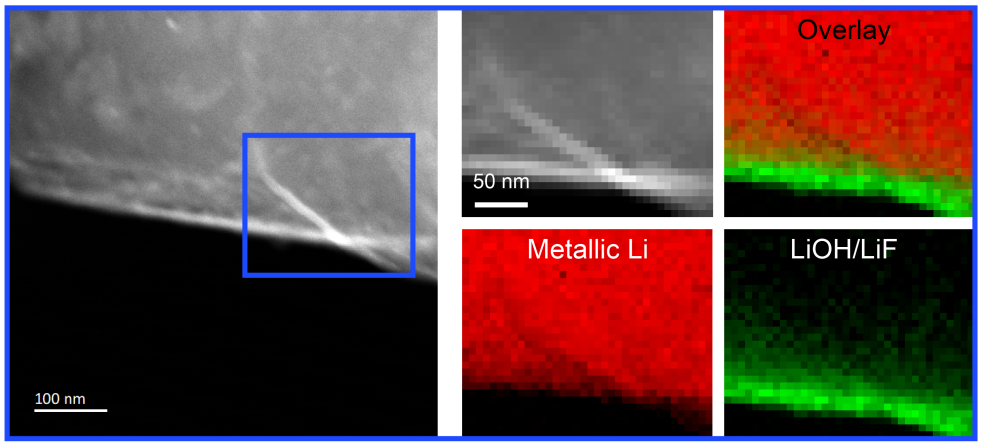
100 nm
50 nm
Overlay
Metallic Li
LiOH/LiF

c

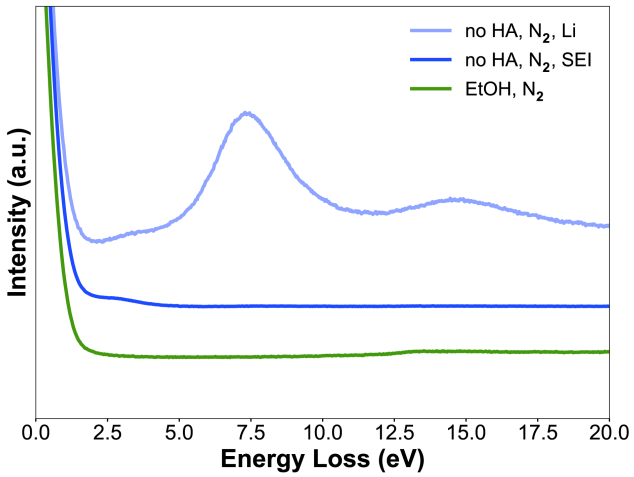
no HA, N2, Li
no HA, N2, SEI
EtOH, N2
Intensity (a.u.)
0.0
2.5
5.0
7.5
10.0
12.5
15.0
17.5
20.0
Energy Loss (eV)

Fig. S4.12 Cryo-STEM EELS results for "no HA, N_2" and "EtOH, N_2" samples. a, Li K-edge core-loss spectra, with images at right depicting where in sample spectra were collected. Light blue, "no HA, N_2" collected in the metallic Li region, darker blue, "no HA, N_2" collected in the SEI region, and green, "EtOH, N_2." Reference spectra represent data extracted from Wang et al., 2011.[34] **b**, EELS maps from "no HA, N_2" sample, showing where the composition changes from primarily metallic Li at the core of the filament to LiOH and LiF in the SEI. **c**, Low-loss spectra showing that only the "no HA, N_2 spectrum from the metallic Li region has the characteristic metallic Li plasma response at ~7.5 eV.

4.7 References

1. MacFarlane, D. R. et al. A Roadmap to the Ammonia Economy. *Joule* **4**, 1–20 (2020).
2. Erisman, J. W., Sutton, M. A., Galloway, J., Klimont, Z. & Winiwarter, W. How a century of ammonia synthesis changed the world. *Nat. Geosci.* **1**, 636–639 (2008).
3. *World fertilizer trends and outlook to 2022* (FAO, 2019).
4. Maxwell, G. R. *Synthetic Nitrogen Products* (Kluwer Academic Publishers, 2004).
5. Smith, C., Hill, A. K. & Torrente-Murciano, L. Current and future role of Haber-Bosch ammonia in a carbon-free energy landscape. *Energy Environ. Sci* **13**, 331–344 (2020).
6. Appl, M. in *Ullmann's Encyclopedia of Industrial Chemistry* 139–225 (2011)
7. Chen, J. G. et al. Beyond fossil fuel-driven nitrogen transformations. *Science* 360, (2018).
8. Soloveichik, G. Electrochemical synthesis of ammonia as a potential alternative to the Haber–Bosch process. *Nat. Catal.* **2**, 377–380 (2019).
9. Schiffer, Z. J. & Manthiram, K. Electrification and Decarbonization of the Chemical Industry. *Joule* **1**, 10–14 (2017).

10. Ludwig, T., Singh, A. R. & Nørskov, J. K. Subsurface Nitrogen Dissociation Kinetics in Lithium Metal from Metadynamics. *J. Phys. Chem. C* **124**, 26368–26378 (2020).
11. Lazouski, N., Chung, M., Williams, K., Gala, M. L. & Manthiram, K. Non-aqueous gas diffusion electrodes for rapid ammonia synthesis from nitrogen and water-splitting-derived hydrogen. *Nat. Catal.* **3**, 463–469 (2020).
12. Suryanto, B. H. R. et al. Nitrogen reduction to ammonia at high efficiency and rates based on a phosphonium proton shuttle. *Science* **372**, 1187–1191 (2021).
13. Li, K. et al. Enhancement of lithium-mediated ammonia synthesis by addition of oxygen. *Science* **374**, 1593–1597 (2021).
14. Tsuneto, A., Kudo, A. & Sakata, T. Efficient Electrochemical Reduction of N2 to NH3 Catalyzed by Lithium. *Chem. Lett.* **22**, 851–854 (1993).
15. Tsuneto, A., Kudo, A. & Sakata, T. Lithium-mediated electrochemical reduction of high pressure N2 to NH3. *J. Electroanal. Chem.* **367**, 183–188 (1994).
16. Lazouski, N., Schiffer, Z. J., Williams, K. & Manthiram, K. Understanding Continuous Lithium-Mediated Electrochemical Nitrogen Reduction. *Joule* **3**, 1–13 (2019).
17. Andersen, S. Z. et al. A rigorous electrochemical ammonia synthesis protocol with quantitative isotope measurements. *Nature* **570**, 504–508 (2019).
18. Cai, X. et al. Lithium-mediated electrochemical nitrogen reduction: mechanistic insights to enhance performance. *iScience* **24**, 1–17 (2021).
19. Andersen, S. Z. et al. Increasing stability, efficiency, and fundamental understanding of lithium-mediated electrochemical nitrogen reduction. *Energy Environ. Sci.* 13, 4291–4300 (2020).

20. Schwalbe, J. A. et al. A Combined Theory-Experiment Analysis of the Surface Species in Lithium-Mediated NH3 Electrosynthesis. *ChemElectroChem* **7**, 1542–1549 (2020).

21. Peled, E. The Electrochemical Behavior of Alkali and Alkaline Earth Metals in Nonaqueous Battery Systems—The Solid Electrolyte Interphase Model. *J. Electrochem. Soc.* **126**, 2047–2051 (1979).

22. Peled, E. & Menkin, S. Review—SEI: Past, Present and Future. *J. Electrochem. Soc.* **164**, A1703–A1719 (2017).

23. Lazouski, N. et al. Proton Donors Induce a Differential Transport Effect for Selectivity toward Ammonia in Lithium-Mediated Nitrogen Reduction. *ACS Catal.* **12**, 5197–5208 (2022).

24. Zachman, M. J., Tu, Z., Choudhury, S., Archer, L. A. & Kourkoutis, L. F. Cryo-STEM mapping of solid–liquid interfaces and dendrites in lithium-metal batteries. *Nature* 560, 345–349 (2018).

25. Li, Y. et al. Correlating Structure and Function of Battery Interphases at Atomic Resolution Using Cryoelectron Microscopy. *Joule* **2**, 2167–2177 (2018).

26. Li, Y. et al. Atomic structure of sensitive battery materials and interfaces revealed by cryo-electron microscopy. *Science* **358**, 506–510 (2017).

27. Zhang, Z. et al. Capturing the swelling of solid-electrolyte interphase in lithium metal batteries. *Science* **375**, 66–70 (2022).

28. Verdouw, H., Van Echteld, J. A. & Dekkers, E. M. L. Ammonia Determination Based on Indophenol Formation with Sodium Salicylate. *Water Res.* **12**, 399–402 (1977).

29. Cherepanov, P. V., Krebsz, M., Hodgetts, R. Y., Simonov, A. N. & MacFarlane, D. R. Understanding the Factors Determining the Faradaic Efficiency and Rate of the Lithium Redox-Mediated N2Reduction to Ammonia. *J. Phys. Chem. C* **125**, 11402–11410 (2021).

30. Adams, B. D. et al. Accurate Determination of Coulombic Efficiency for Lithium Metal Anodes and Lithium Metal Batteries. *Adv. Energy Mater.* **8**, 1702097 (2018).
31. Xiao, J. et al. Understanding and applying coulombic efficiency in lithium metal batteries. *Nat. Energy* **5**, 561–568 (2020).
32. Mehta, R. in *Scanning Electron Microscopy* (ed. Kazmiruk, V.) 17–30 (InTech, 2012).
33. Wang, F. et al. Chemical Distribution and Bonding of Lithium in Intercalated Graphite: Identification with Optimized Electron Energy Loss Spectroscopy. *ACS Nano* **5**, 1190–1197 (2011).
34. Wang, F. et al. Chemical Distribution and Bonding of Lithium in Intercalated Graphite: Identification with Optimized Electron Energy Loss Spectroscopy. *ACS Nano* **5**, 1190–1197 (2011).

Chapter 5: Outlooks and future work

5.1 Summary and outlook

This Ph.D. dissertation presents a mechanistic understanding of lithium (Li) metal deposition and the solid electrolyte interphase (SEI) formation by integrating electrochemical methods with cryogenic electron microscopy (cryo-EM), revealing multi-faceted roles of Li metal in batteries and beyond. Through the decoupling of Li deposition from SEI formation in **Chapter 2**, the intrinsic deposition morphology of Li was revealed to be a rhombic dodecahedron that is independent of electrolyte chemistry or substrate composition. The ability to promote more dense Li metal deposition using pulse-current strategies offers a new direction for engineering stable Li metal anodes. Moreover, this work establishes a fundamentally new growth mode of Li metal deposition, where deposition occurs faster than the formation of the SEI. Besides enhancing our understanding of Li deposition and morphology, this principle can also be extended to other reactive metals, e.g., sodium metal, potassium metal. By doing so, we can demonstrate the broader applicability of the methodology and opens new opportunities to explore how reactive metal deposition fundamentally proceeds without corrosion film. Understanding these intrinsic growth mechanisms is critical to regulating the reversibility of metal plating/stripping and optimizing the performance of alkali metal batteries.

Moreover, by decoupling SEI formation from Li metal deposition, this approach offers a powerful platform for systematic and controllable investigation of SEI chemistry. In **Chapter 2**, we demonstrated that the deposition current density of 1,000 mA cm^{-2} is sufficient to outpace SEI formation, thereby revealing the intrinsic growth behavior of Li metal. However, the precise

current density threshold required to overcome SEI influence, referred to here as the transitional current density, remains unknown within the 100 to 1,000 mA cm^{-2} range. Although the morphology of Li metal deposition become independent of electrolyte chemistry once SEI formation is outpaced, the transitional current density required to outpace SEI formation varies across different electrolytes. This value also further depends on factors such as operating temperature. Moreover, the transitional current density that just outpaces SEI formation can be used to quantify the SEI formation rate, exploring the intrinsic kinetics of SEI formation. Identifying and quantifying this transitional current density in different electrolyte systems at different temperature will be an important direction for future research. Such insights could enable the deliberate control of SEI formation rates, offering a new lever for tuning interfacial properties and guiding electrolyte design across a wide range of battery chemistries.

Additionally, by separating the SEI formation process from electrodeposition, we identified the critical role of electric field modulation in shaping interfacial chemistry in **Chapter 3**. The definitions of electrochemical SEI and chemical SEI provide a new conceptual framework for understanding and designing interphases with tunable composition and function. Lastly, by extending Li chemistry into non-traditional electrochemical systems, such as ammonia electrosynthesis, **Chapter 4** demonstrates the broader impact of Li metal and the versatility of cryo-EM for probing reactive electrochemical interfaces.

Despite these advances, several important questions remain and open up compelling directions for future research. First, while cryo-EM offers unprecedented spatial resolution and chemical sensitivity, it's limited to capture the real-time dynamics of Li growth and SEI evolution under

operating conditions. The development of novel "freeze-and-capture" strategies that target transient reactions states can be fruitful directions for future.[1-2] Second, electrochemical catalysis involves dynamic interfacial regions where electric fields, solvation structures, and ion distributions interact.[3-4] The methodology developed here, using electrochemical modulation and cryo-preservation, may be extended to interrogate these transient and reactive electrochemical environments, ultimately helping to reveal how interfacial nanostructures dictate selectivity, kinetics, and stability in complex reactions. Third, the insights gained in conventional liquid electrolytes now invite application to solid-state[5-6] and polymer-based[7-8] electrolyte systems, where ion transport and SEI formation are fundamentally different. How solid polymer or hybrid electrolytes modulate Li morphology and interphase chemistry under various electrochemical conditions remains largely unexplored. Applying the principles of pulse-seeding and electrical double layer (EDL)-mediated SEI control in these systems could enable a new generation of safe and long-term Li metal batteries. Finally, as demonstrated in **Chapter 4**, Li metal chemistry can serve as a platform for driving new chemical transformations, such as electrified ammonia synthesis.[9-11] This intersection between battery science and electrosynthesis offers a rich space for discovery. Future work may focus on how to leverage Li metal's unique redox properties to enable other challenging transformations and how cryo-EM can capture and visualize reaction intermediates at the solid–liquid interface in various energy systems.

In summary, this work not only advances our understanding of Li metal deposition and SEI chemistry but also opens new methodological and conceptual directions. The combination of electrochemistry, interfacial engineering, and cryo-EM imaging offers a powerful platform for addressing fundamental challenges in energy storage and beyond. Continued exploration along

these directions will be critical for the rational design of next-generation electrochemical systems with enhanced performance, safety, and sustainability.

5.2 References

1. Li, Y. et al. Electrified Operando-Freezing of Electrocatalytic CO2 Reduction Cells for Cryogenic Electron Microscopy. *Nano Lett.* **24**, 10409–10417 (2024).
2. Dutta, N. S., et al. Ion Depletion Microenvironments Mapped at Active Electrochemical Interfaces with Operando Freezing Cryo-Electron Microscopy. *ACS Energy Lett.* **9**, 2464–2471 (2024).
3. Kim, C., Weng, L.-C., Bell, A. T. Impact of Pulsed Electrochemical Reduction of CO2 on the Formation of C2+ Products over Cu. *ACS Catal.* **10**, 12403–12413 (2020)
4. Nitopo, S., et al. Progress and Perspectives of Electrochemical CO2 Reduction on Copper in Aqueous Electrolyte. *Chem. Rev.* **119**, 7610–7672 (2019)
5. Ye, L., Li, X. A dynamic stability design strategy for lithium metal solid state batteries. *Nature* **593**, 218–222 (2021)
6. Cheng, X.-B., et al. Recent Advances in Energy Chemistry between Solid-State Electrolyte and Safe Lithium-Metal Anodes. *Chem.* **5**, 74-96 (2019).
7. Ding, P., et al. Polymer electrolytes and interfaces in solid-state lithium metal batteries. *Mater. Today* **51**, 449-474 (2021).
8. Huang, Z., et al. A salt-philic, solvent-phobic interfacial coating design for lithium metal electrodes. *Nat. Energy* **8**, 577–585 (2023)
9. Fu, X., et al. Continuous-flow electrosynthesis of ammonia by nitrogen reduction and hydrogen oxidation. *Science* **379**, 707-712 (2023)

10. Chang, W., et al. Lithium-mediated nitrogen reduction to ammonia via the catalytic solid–electrolyte interphase. *Nat. Catal.* **7**, 231-241 (2024)
11. Mangini, A. et al. Multivariate Approaches Boosting Lithium-Mediated Ammonia Electrosynthesis in Different Electrolytes. *Angew. Chem.* **137**, e202416027 (2025)